EASY ON THE IONS: PHOTON SCATTERING ERRORS FROM FAR-DETUNED RAMAN BEAMS IN TRAPPED-ION QUBITS

by

ISAM DANIEL MOORE

A DISSERTATION

Presented to the Department of Physics
and the Division of Graduate Studies of the University of Oregon
in partial fulfillment of the requirements
for the degree of
Doctor of Philosophy

June 2023

DISSERTATION APPROVAL PAGE

Student: Isam Daniel Moore

Title: Easy on the Ions: Photon Scattering Errors from Far-Detuned Raman Beams in Trapped-Ion Qubits

This dissertation has been accepted and approved in partial fulfillment of the requirements for the Doctor of Philosophy degree in the Department of Physics by:

Dr. Steven Van Enk	Chair
Dr. David T. C. Allcock	Advisor
Dr. Stephanie Majewski	Core Member
Dr. Andrew Marcus	Institutional Representative

and

Krista Chronister	Vice Provost for Graduate Studies

Original approval signatures are on file with the University of Oregon Division of Graduate Studies.

Degree awarded June 2023

DISSERTATION ABSTRACT

Isam Daniel Moore

Doctor of Philosophy

Department of Physics

June 2023

Title: Easy on the Ions: Photon Scattering Errors from Far-Detuned Raman Beams in Trapped-Ion Qubits

The viability of quantum computers depends on the development of scalable platforms with low error rates. Our "Oregon Ions" group has studied one such scalable architecture proposal including the limitations placed on logic gate fidelity by photon scattering. We studied spontaneous Raman scattering-induced errors in stimulated Raman laser beam-driven logic gates in metastable- and ground-manifold-encoded qubits. For certain parameter regimes, we found that previous, simplified models of the process significantly overestimated the gate error rate due to spontaneous photon scattering. We developed an improved model, which shows that there is no fundamental lower limit on gate error due to spontaneous photon scattering for electronic ground state qubits in commonly-used trapped-ion species when the Raman laser beams are red detuned from the main optical transition. Additionally, spontaneous photon scattering errors are studied for qubits encoded in a metastable $D_{5/2}$ manifold, showing that gate errors below 10^{-4}

are achievable for all commonly used trapped ions. Furthermore, we extended this theory from hyperfine to Zeeman qubits and we measured scattering rates from far-detuned Raman beams in a metastable $D_{5/2}$ Zeeman qubits in $^{40}Ca^{+}$, obtaining results that matched theoretical expectations. Finally, we present progress towards implementing a two-qubit Mølmer-Sørensen gate with these Raman beams in trapped $^{40}Ca^{+}$ ions.

This dissertation contains previously published and unpublished material.

CURRICULUM VITAE

NAME OF AUTHOR: Isam Daniel Moore

GRADUATE AND UNDERGRADUATE SCHOOLS ATTENDED:
University of Oregon, Eugene, Oregon
Wright State University, Dayton, Ohio

DEGREES AWARDED:
Doctor of Physics, 2022, University of Oregon
Bachelor of Science, 2017, Wright State University

AREAS OF SPECIAL INTEREST:
Quantum Computing, Quantum Information, Atomic Physics

PROFESSIONAL EXPERIENCE:

Graduate Research Assistant, University of Oregon, 2019-2023

Graduate Teaching Assistant, University of Oregon, 2017-2019

GRANTS, AWARDS AND HONORS:

Weiser Doctoral Thesis Award, University of Oregon Department of Physics, 2023

PUBLICATIONS:

Moore, I. D., van Enk, S. J. (2021). Self-consistent tomography and measurement-device independent cryptography. *Int. J. Quantum Inf.* **19**, 2040003

Allcock, D. T. C., Campbell, W. C., Chiaverini, J., Chuang, I. L., Hudson, E. R., Moore, I. D., Ransford, A., Roman, C., Sage, J. M., Wineland, D. J., (2021). *omg* blueprint for trapped ion quantum computing with metastable states. *APL*, **119**, 214002.

Moore, I. D., Campbell, W. C., Hudson, E. R., Boguslawski, M. J., Wineland, D. J., Allcock, D. T. C. (2023). Photon scattering errors during stimulated Raman transitions in trapped-ion qubits. *PRA*, **107**, 032413.

Boguslawski, M. J., Wall, Z. J., Vizvary, S. R., Moore, I. D., Bareian, M., Allcock, D. T. C., Wineland, D. J., Hudson, E. R., Campbell, W. C. (2023). Errors in stimulated-Raman-induced logic gates in $^{133}Ba^{+}$. arXiv:2212.02608

Quinn, A., Metzner, J., Muldoon, J. E., Moore, I. D., Brudney, S., Das, S., Allcock, D. T. C., Joglekar, Y. N. (2023). Observing super-quantum correlations across the exceptional point in a single, two-level trapped ion. arXiv:2304.12413.

I thank Matt Boguslawski and Zach Wall for help in checking the accuracy of the calculations. I thank Wes Campbell and Eric Hudson for the extensive discussions of scattering processes and the Kramers-Heisenberg formula. I thank Steven van Enk for working with me scientifically and for his advice throughout graduate school. I also thank Sean Brudney, Gabe Gregory, and Vikram Sandhu for all their help during graduate school. I thank Dave Wineland, who read this thesis and provided much helpful guidance during graduate school, and I especially thank Alex Quinn and Jeremy Metzner who read this thesis and took data for it. I thank David Allcock for his patient guidance and mentorship to me over the years. Finally, I thank my friends, family, and Kaylin.

TABLE OF CONTENTS

Chapter Page

I. INTRODUCTION 1

1.1. Theory of ion trap quantum computing 1
1.2. Transitions Between Energy Levels in Trapped Ions 2
1.3. Laser Cooling in Ion Traps 4
1.4. Gates in an Ion Trap 7
1.5. Photon Scattering Errors in Trapped-Ion Quantum Computers . 14

II. OMG ARCHITECTURE 17

2.1. Metastable qubits 18
2.2. *omg* architecture 19
2.3. Two-Qubit Gates in m Qubits 23

III. EXPERIMENTAL METHODS 24

3.1. Ion Trap 24
3.2. Magnetic Field 27
3.3. Ion Detection 28
3.4. Trap rf Drive 29
3.5. Laser Systems 30

Chapter Page

3.6. AOM Boards 34

3.7. ARTIQ 39

3.8. Beam Delivery System 41

IV. SCATTERING THEORY 44

4.1. Choice of Qubit 44

4.2. Scattering Probability 46

4.3. Power Requirements 63

V. ZEEMAN QUBITS IN $^{40}CA^{+}$ 69

5.1. Zeeman Qubits in the $D_{5/2}$ Manifold 69

5.2. Scattering Theory for Zeeman Qubits 74

VI. SCATTERING RATE MEASUREMENTS 78

6.1. 976 nm laser setup 78

6.2. Scattering rate experiments 80

VII. TWO-QUBIT GATE 94

7.1. Mølmer-Sørensen Gate Setup 94

7.2. Preliminary Results 100

7.3. Future Directions 101

Chapter Page

VIII. CONCLUSION 105

APPENDICES

A. DERIVATION OF SCATTERING RATE 108

B. DECAY RATE FROM FERMI'S GOLDEN RULE 115

C. POWER REQUIREMENTS DERIVATION 117

D. RECOVERING CLASSICAL LIMITS 119

E. QUANTUM CRYPTOGRAPHY PROTOCOL 122

Bibliography 125

LIST OF FIGURES

Figure Page

1.1. Raman transitions schematic 3
1.2. The Bloch sphere 9
2.1. Alkaline earth ion's atomic structure 20
2.2. *omg* schemes 21
3.1. Render of our ion trap 25
3.2. Photograph of our trap 26
3.3. Magnetic coils 28
3.4. Ion camera schematic 29
3.5. Picture of ion camera 29
3.6. Photograph of laser rack 32
3.7. Laser rack drawer 33
3.8. Inside AOM 34
3.9. Blue AOM efficiency 36
3.10. Red AOM efficiency 37
3.11. AOM rack board 38
3.12. AOM board schematics 39
3.14. Schematic ARTIQ system 40
3.13. AOM board design schematic 42
3.15. Schematic of trap optics 43
4.1. g and m qubits 45

Figure Page

4.2. Scattering processes 50

4.3. Single-qubit gate Raman scattering error 55

4.4. Two-qubit gate Raman scattering error 58

4.5. Rayleigh scattering error ratio 64

4.6. Single qubit gate power requirements 67

4.7. Two-qubit gate power requirements 68

5.1. Zeeman m qubit 71

5.2. Laser and rf m qubit operations 72

5.3. Polarization impurity scattering 74

5.4. Power and detuning requirements for light shift 75

5.5. Rayleigh error ratio 77

6.1. 976 nm laser 79

6.2. 976 nm optical setup. 79

6.3. Scattering configurations 84

6.4. $m_J = +5/2$, σ^- raw measurement results 88

6.5. $m_J = +5/2$, σ^- scattering vs. power results 89

6.6. $m_J = +3/2$, σ^- raw measurement results 90

6.7. $m_J = +3/2$, σ^- scattering vs. power results 91

6.8. $m_J = +3/2$, π raw measurement results 92

6.9. $m_J = +3/2$, π scattering vs. power results 93

7.1. MS gate schematic geometry 95

7.2. Carrier Rabi flopping, m qubit 96

7.3. Sideband Rabi flopping, m qubit 98

7.4. Phase sensitive vs. phase insensitive geometry 99

Figure Page

7.5. MS gate schematic state transfer 100

7.6. Walsh modulation schematic 101

7.7. Walsh modulation preliminary results 102

7.8. Preliminary Mølmer-Sørensen gate results 103

A.1. Scattering derivation frequencies 109

LIST OF TABLES

Table Page

1.1. Minimum scattering error during a two-qubit gate in some commonly-used trapped-ion species. Sourced from Ozeri, 2007. 15

4.1. Hyperfine qubit characteristics 47

8.1. Scattering characteristics of m and g qubits 107

CHAPTER I

INTRODUCTION

1.1. Theory of ion trap quantum computing

1.1.1. Earnshaw's Theorem and the Ion Trap Potential

If asked how to trap a charged particle, you might initially think an appropriately chosen static electric field will suffice. However, it is not possible to trap charged particles using static electric fields only. This result is known as Earnshaw's Theorem. It is simple to demonstrate: the charged particle needs to be confined in free space in the presence of an electric field sink, *i.e.*, a point where the electric force field's divergence is negative (for a positively-charged particle). However, this contradicts Gauss' law. The divergence of an electric force field $\mathbf{F}$ arising from electric potential U in free space is, by Laplace's equation,

$$\nabla \cdot \mathbf{F} = \nabla \cdot (\nabla U) = \nabla^2 U = 0 \tag{1.1}$$

where the last step is due to Gauss' law. This means that we need an electrodynamic interaction to trap a charged particle. There are many ways to generate such an interaction, but in our group, we use a linear Paul trap.

1.1.2. Linear Paul Traps and the Mathieu Equations

A linear Paul trap Paul and Steinwedel, 1953 often consists of a pair of rf electrodes, a pair of ground electrodes, and a pair of dc endcap electrodes Figure 3.1. The rf electric field null line defines the "trap axis" (for our trap,

this is roughly the vector between the endcap electrodes). The rf electrodes ('rod' electrodes) run parallel to this axis. While the endcap electrodes have a static potential, two of the rod electrodes have rf signals applied to them with the other pair being connected to ground. This generates an oscillating quadrupole electric field and lets us get around Earnshaw's theorem. Along with the on-axis confinement provided by the dc endcaps, this creates a ponderomotive confining potential in 3D.

1.2. Transitions Between Energy Levels in Trapped Ions

A quantum computer requires quantum logic gates. When working with trapped ions, our gates physically amount to driving transitions between the qubit states, which are encoded in some energy levels. There are many such transitions, such as magnetic dipole (M1), electric dipole (E1), and electric quadrupole (E2) transitions. Although we use other transitions in the lab (such as M1), this work focuses primarily on E1 transitions. For that reason, in this section, I will discuss how we can change an ion's energy by coupling to such E1 transitions.

1.2.1. Stimulated Raman Transitions

Stimulated Raman transitions are a common method for inducing E1 transitions. Here I will explain the mechanism behind Raman transitions, as well as give a theoretical description of a single-qubit gate and a two-qubit gate that we have implemented in the lab.

Consider a three level "Λ" system as in Figure 1.1, with one excited state $|e\rangle$ and two lower lying states $|1\rangle$ and $|2\rangle$. We can couple the low-lying states to the excited state via the electric dipole coupling by applying laser beams to the ion.

The strength of this coupling can be characterized by the 'Rabi frequency' Ω_g. The Rabi frequency is defined as

$$\Omega_g = \frac{E \langle e | \vec{d} \cdot E\hat{\epsilon} | g \rangle}{\hbar}, \tag{1.2}$$

where E is the peak electric field amplitude, $\hat{\epsilon}$ is the polarization direction of the beam, and $g = 1, 2$ indexes the lower states.

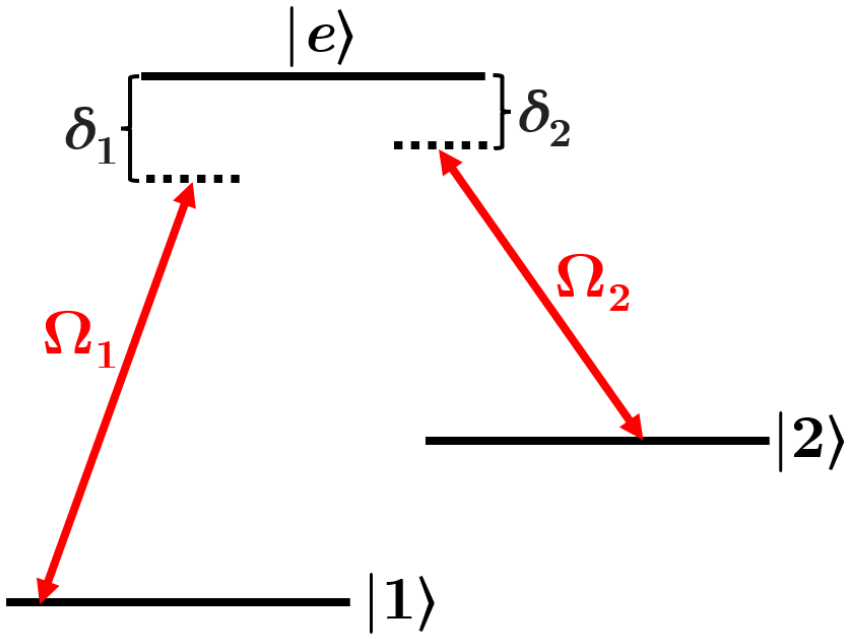

FIGURE 1.1. Schematic of a stimulated Raman transition between states $|1\rangle$ and $|2\rangle$ via the excited state $|e\rangle$.

To understand stimulated Raman transitions in this system, we need to study the Hamiltonian governing their dynamics:

$$\mathscr{H} = \frac{1}{2}\Omega_1 e^{i\phi_1} e^{i\mathbf{k_1}\cdot\mathbf{r} - i\delta_1 t} |e\rangle \langle 1| + \frac{1}{2}\Omega_2 e^{i\phi_2} e^{i\mathbf{k_2}\cdot\mathbf{r} - i\delta_2 t} |e\rangle \langle 2| + \text{h.c.} \tag{1.3}$$

Following the discussion in Ballance, 2014, we note that if $\Omega_1 \ll \delta_1$ and $\Omega_2 \ll \delta_2$, then there will be largely no population transfer out of states $|1\rangle$ and

$|2\rangle$. If, however, $\delta = |\delta_1 - \delta_2| \ll \delta_1, \delta_2$, then we can apply the James-Jerke approximation James and Jerke, 2007:

$$\mathscr{H} = \frac{\Omega_1}{4\delta_1}(|1\rangle\langle 1| - |e\rangle\langle e|) + \frac{\Omega_2}{4\delta_2}(|2\rangle\langle 2| - |e\rangle\langle e|) + \frac{\Omega_1\Omega_2}{4\Delta}\left(e^{i\phi}e^{i\Delta\mathbf{k}-i\delta t}|2\rangle\langle 1| + h.c.\right), \tag{1.4}$$

where $\phi = \phi_1 - \phi_2$ and $\frac{1}{\Delta} = \frac{1}{2}(\frac{1}{\delta_1} - \frac{1}{\delta_2})$. Final term of Eqn. 1.4 generates a coupling between states $|1\rangle$ and $|2\rangle$ through a two-photon emission process. This is a stimulated Raman transition.

1.3. Laser Cooling in Ion Traps

1.3.1. Doppler Cooling

Simply creating a potential well to confine the ion does not mean it will stay there. If the ion has sufficient kinetic energy, it can escape the trap. Therefore to keep the ion trapped, we need to keep it cool. We do this by Doppler cooling D. J. Wineland, Drullinger and Walls, 1978 and Neuhauser et al., 1978.

Consider a trapped ion which has an electronic transition of frequency ω_0. We can implement Doppler cooling by applying a laser beam tuned red of this transition, i.e., we apply a laser with frequency $\omega_L = \omega_0 - \Delta$, where Δ is the detuning of the laser beam. Since the ion will be oscillating about its equilibrium position, the frequency of the laser light experienced by the ion will be Doppler-shifted. This implies that the transition will be driven more strongly, and therefore that the ion will preferentially absorb a photon, when the ion is moving towards the laser beam. In such a case, the ion will lose momentum since it is traveling opposite the direction of the beam. On average, then, the atom will lose

momentum when it absorbs photons. When it later emits this absorbed photon, it will do so in some random direction. The average change in momentum from emission is therefore zero. So on net, the laser will cool the ion.

There are limits to this process, of course. You cannot bring the ion to a standstill. The average emission event does not reduce the ion's *momentum*, but it does change its kinetic energy by $\hbar^2 k^2/2m$, where k is the transition wavenumber and m is the ion mass. This may seem contradictory, but it is a simple consequence of the fact that the velocity averages to zero, but the square of the velocity does not. So Doppler cooling clearly cannot reduce the ion's kinetic energy below the single photon recoil kinetic energy. However, since the actual equilibrium will be achieved when the heating and cooling rates of the competing processes are equal, the true limit is somewhat different (and higher): it is $\hbar\gamma/2k_B$, where γ is the linewidth of the transition and k_B is the Boltzmann constant Letokhov, Minogin and Pavlik, 1977. For certain applications (such as two qubit gates), it is desirable to be closer to the motional ground state than the Doppler limit will allow. Fortunately, we are able to beat the Doppler limit by implementing resolved sideband cooling.

1.3.2. Resolved Sideband Cooling

Resolved sideband cooling is a standard technique in ion trapping Monroe et al., 1995, Eschner et al., 2003. To understand the mechanism behind this method, consider a trapped ion with motional frequency ω_m. Suppose a laser beam of frequency ω_L is driving an atomic transition of frequency ω_0 in this ion. As a function of ω_L, the atomic emission spectrum will have a transition at ω_0, as well as many transitions separated from the strong transition by integer

multiples of ω_m. The strong transition is referred to as the 'carrier' and the weaker transitions are referred to as the 'sidebands'. Physically, these transitions are allowed by emitting a photon and simultaneously absorbing/emitting some number of motional phonons.

These sideband transitions can be exploited to cool the ion. By setting the laser frequency to $\omega_L = \omega_0 - \omega_m$, the ion will become electronically excited most often when it simultaneously loses a phonon. When coupled with a mechanism for repumping back to the initial state, this cools the ion down. However, the photons emitted from this repumping will kick the ion, which causes heating. This issue can be avoided by operating in the Lamb-Dicke regime.

1.3.3. Lamb-Dicke Regime

The Lamb-Dicke regime is characterized by a weak coupling between the ion's atomic and motional states D. Wineland et al., 1998. Mathematically, the condition to be in the Lamb-Dicke regime is given by

$$\sqrt{\langle \Psi_m | \, k_z^2 z^2 \, | \Psi_m \rangle} \ll 1 \tag{1.5}$$

where $|\Psi_m\rangle$ is the motional wavefunction, z is the distance away from the ion's equilibrium position operator along the axis of interest, and k_z is the z-component of the laser's wavevector. To better understand the inequality 1.5, we begin by expressing the operator $\hat{z}$ as

$$\hat{z} = \sqrt{\frac{\hbar}{2m_i\omega_m}}(a + a^\dagger) \tag{1.6}$$

where m_i is the ion's mass, and a and $a^\dagger$ are the ladder operators which, respectively, lower or raise the photon number of photon number eigenstates $|n\rangle$ (Fock states). If we assume we are in a Fock state $|n\rangle$, then the inequality 1.5 may be written

$$\sqrt{\langle\Psi_m| k_z^2 z^2 |\Psi_m\rangle} = \sqrt{\frac{\hbar k_z^2}{2m_i\omega_m} \langle\Psi_m| (a+a^\dagger)^2 |\Psi_m\rangle} = \sqrt{\frac{\hbar k_z^2}{2m_i\omega_m}(2n+1)} \tag{1.7}$$

$$= \sqrt{\eta^2(2n+1)} \ll 1 \tag{1.8}$$

where we have defined the 'Lamb-Dicke parameter' η as $\sqrt{\hbar k_z^2/2m_i\omega_m}$. Fundamentally, this requirement just says that a small Lamb-Dicke parameter is needed to be in the Lamb-Dicke regime. The physical meaning of this is that the kinetic energy change due to a laser photon recoil energy $\hbar^2 k_z^2/2m_i$ must be much smaller than the harmonic oscillator energy level separation $\hbar\omega_m$, i.e., the atomic energy states must be largely decoupled from this motion. This is necessary in sideband cooling, since after driving a sideband transition, we want spontaneous emission events (which serve as the repumping process mentioned above) to take place primarily at the carrier frequency so as to not significantly alter the motional states and disrupt the cooling process. Satisfying the Lamb-Dicke criterion ensures this is the case.

1.4. Gates in an Ion Trap

Information processing in a classical computer takes place on bits, which can take the values 0 or 1. To make a classical computer most useful, it is desirable to ensure that it is capable of performing any logical operation, i.e., it is able to map

any string of bits to any other string of bits. Such a device is called a universal computer, and the set of logical operations is said to be functionally complete. The simplest functionally complete set of operators is comprised only of the operator NAND. The NAND operator is the negation of the logical conjunction of two bits, and it can be proven that this operator alone can map any string of bits to any other string of bits. Similarly, in a quantum computer, it is desirable to construct a set of universal quantum logic gates.

1.4.1. Universal Quantum Logic Gate Sets

Since quantum logic gates can be represented as vectors in an the space of unitary operators, we need a set of gates that can generate any desired unitary operation. For a single qubit, you can generate a universal gate set with the the Pauli matrices,

$$\sigma_X = \begin{bmatrix} 0 & 1 \\ 1 & 0 \end{bmatrix}, \ \sigma_Y = \begin{bmatrix} 0 & -i \\ i & 0 \end{bmatrix}, \ \sigma_Z = \begin{bmatrix} 1 & 0 \\ 0 & -1 \end{bmatrix}, \tag{1.9}$$

written in the $\{|0\rangle, |1\rangle\}$ basis. You can use these to create operators that rotate vectors along the "Bloch sphere". The Bloch sphere is a representation of all possible single qubit states, with $|0\rangle$ and $|1\rangle$ corresponding to opposite 'poles' of the sphere along the Z-axis, with X and Y corresponding to axes in the equatorial plane of the sphere. A visualization of the Bloch sphere is given in Fig. 1.2. It is trivial to see that operators which can map an arbitrary vector to any other vector on the Bloch sphere would constitute a universal set. The rotation operators do just that, and are written as

$$R_X(\theta) = e^{\frac{-i\theta}{2}\sigma_X}, R_Y(\theta) = e^{\frac{-i\theta}{2}\sigma_Y} \; R_Z(\theta) = e^{\frac{-i\theta}{2}\sigma_Z}. \tag{1.10}$$

Here, θ is the angle of the rotation, and X, Y, and Z correspond to the axis of rotation on the Bloch sphere.

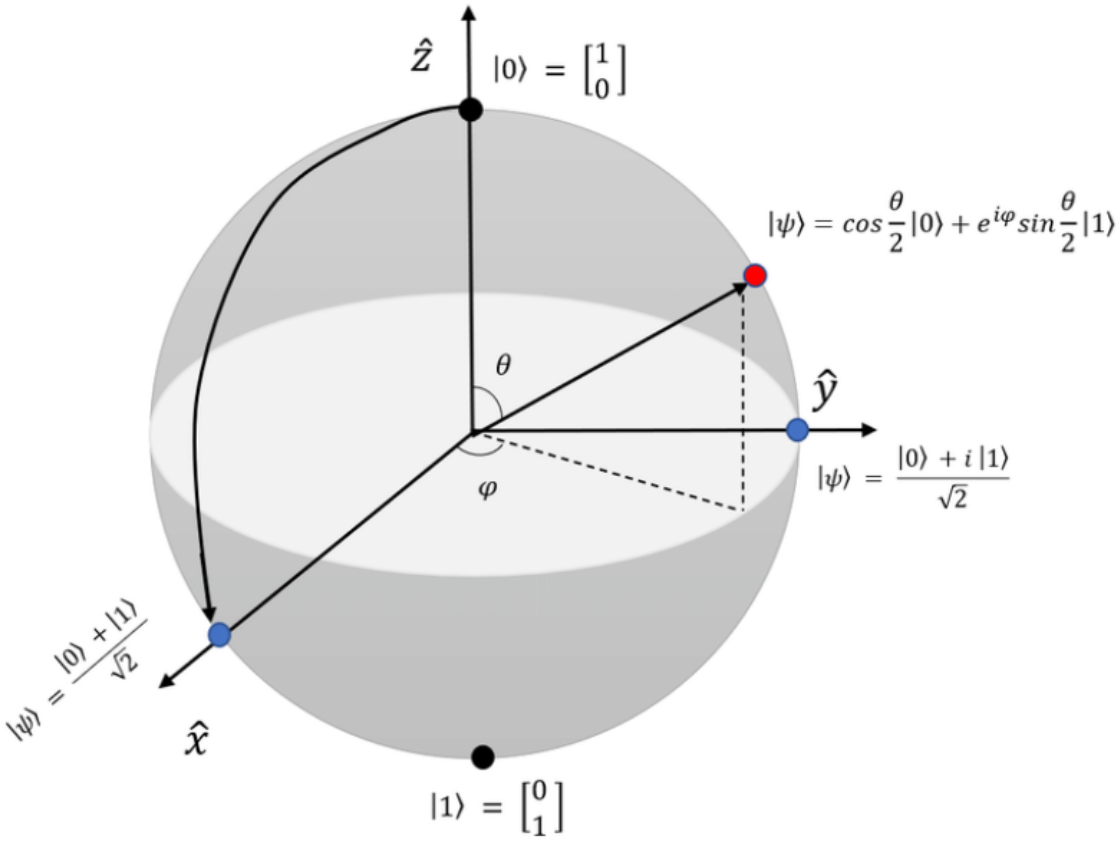

FIGURE 1.2. The Bloch sphere (figure taken from Saad et al., 2021). Poles of the Z-axis correspond to the states $|0\rangle$ and $|1\rangle$. The angle θ adjusts the population of $|0\rangle$ and $|1\rangle$ and the angle ϕ adjusts the relative phase.

For the n-qubit case, however, these operators would not constitute a universal set. The set must be augmented by an entangling, two-qubit gate, such as the controlled-not (CNOT) gate. The CNOT gate is a two-qubit gate that

simply flips the second qubit if the first qubit is $|1\rangle$ but does nothing if the first qubit is $|0\rangle$. In matrix form, the CNOT gate is

$$CNOT = \begin{bmatrix} 1 & 0 & 0 & 0 \\ 0 & 1 & 0 & 0 \\ 0 & 0 & 0 & 1 \\ 0 & 0 & 1 & 0 \end{bmatrix}, \tag{1.11}$$

written in the $\{|00\rangle, |01\rangle, |10\rangle, |11\rangle\}$ basis. The purpose of the CNOT gate is to generate entanglement between qubits. You can see that the CNOT gate generates entanglement by applying it to the state $\frac{1}{\sqrt{2}}(|0\rangle) \otimes (|0\rangle + |1\rangle)$, which results in the maximally-entangled Bell state $\frac{1}{\sqrt{2}}(|00\rangle + |11\rangle)$.

The rotation operators, plus a phase shift operator, plus CNOT constitute a universal gate set. This is provable Nielsen and Chuang, 2000, but the proof is complicated. Intuitively, you can discern that these operators are universal because they are capable of creating any unitary single-qubit operator and can also entangle any two qubits together.

In practice, phase shifts, rotation operators, and the CNOT gate are straightforward enough to implement in ion traps that they are commonly used to implement general quantum circuits. In our lab, we usually physically perform these gates using stimulated Raman transitions. We discuss the physics behind such transitions and their use in implementing our quantum logic gates in the sections below.

1.4.2. Single-Qubit Gate

Perhaps the most commonly-used single-qubit gate is σ_X gate, i.e., a π rotation about the X-axis of the Bloch sphere. This is the same as a σ_Y gate, but with a different phase. For qubits encoded in sublevels of some manifold in a trapped ion, such gates are usually physically implemented in one of two ways: stimulated Raman transitions or rf pulses. Stimulated Raman transitions were discussed in some detail above, but the physics underlying rf-pulse-induced σ_X gates is very similar; the only difference is that rf pulses utilize an M1 coupling as opposed to the E1 coupling used by Raman transitions.

1.4.3. Two-Qubit Gate

Investigation into two-qubit gates in trapped ions began with the Cirac-Zoller (CZ) gate Cirac and Zoller, 1995). The CZ gate is a means of generating entanglement between two ions, but it is challenging to implement. Two difficulties with implementing the CZ gate are the need for individually addressing each qubit with the laser beams and the first-order dependence of the gate fidelity on temperature.

In the intervening years since the CZ paper, work has been done to construct more practical two-qubit gates in trapped ions. Today, the two most common implementations of a two-qubit gate in trapped-ion quantum computers are the Mølmer-Sørensen gate (a controlled σ_x gate) and the light shift gate (a controlled σ_z gate). I will discuss each of these gates in turn.

1.4.4. The Mølmer-Sørensen Gate

The original discussion of this gate may be found in Mølmer and Sørensen, 1999. The first experimental demonstration was in Sackett et al., 2000. This gate flips each qubit and applies a phase conditional on their parity.

Physically, an MS gate generates entanglement by coupling the ions internal, electronic state to the collective motion of the ion crystal. The gate may be driven by microwaves, quadrupole lasers, or by pairs of Raman beams. Since the latter case is what we have implemented in the lab, I will discuss it further. We can implement the MS gate using Raman beams with each detuned by some amount δ from the resonance of the sideband transitions. This detuning ensures that the only transitions which flip both ions' qubit states are driven resonantly. The action of the gate can be visualized in phase space, where the position and momentum of the ions form the x and y axes. The joint state of the ion may be represented as a point in this space. The MS gate acts by steering the ion state around this space, forming a closed loop at the end of the gate. The area enclosed by this loop corresponds to the phase that state accumulates, and, for appropriately chosen parameters, the MS gate will impart phase only to certain joint states of the ion. We discuss our lab's progress towards physically implementing this gate in a novel qubit encoding in Chapter VII

1.4.5. The Light Shift Gate

The light shift (LS) gate Leibfried et al., 2003 Home et al., 2009, like the MS gate, is a common entanglement-generation mechanism for trapped ions. Both gates are closely related; they are simply geometric phase gates in different bases. To physically implement an LS gate, we need to choose a Raman beam

polarization such that $|0\rangle$ and $|1\rangle$ couple to it differently. We can then apply a pair of such beams to generate a standing interference pattern. In this case, the light shift varies spatially which generates a force. If we adjust the relative phase of the Raman beams, we can generate a beat note. By tuning this beat frequency to the motional mode frequency, we can induce a spin-dependent force. Finally, we can detune the Raman beams from the motional sideband of interest by a small amount δ, which may be used to control the phase accumulated depending on the ion pair's joint state. If we neglect off-resonant terms, the phase accumulated by each state is approximately Ballance, 2014

$$\begin{aligned} |11\rangle &: (1 + e^{i\phi_m})\Omega_1 \\ |10\rangle &: \Omega_1 - e^{i\phi_m}\Omega_0 \\ |01\rangle &: e^{i\phi_m}\Omega_1 - \Omega_0 \\ |00\rangle &: -(1 + e^{i\phi_m})\Omega_0, \end{aligned} \tag{1.12}$$

where ϕ_m is a the Raman phase difference between the two ions and Ω_j is the single-beam Rabi frequency for the qubit state $|j\rangle$.

For well-chosen experimental parameters, we can set $\phi_m = \pi$ to maximize the efficiency of this scheme. In this case, ion pairs with the same parity will experience no force, but opposite-parity ion pairs will experience a force of $\pm(\Omega_0 + \Omega_1)$. This can be used to implement the logical gate

$$\hat{U} = \begin{bmatrix} 1 & 0 & 0 & 0 \\ 0 & i & 0 & 0 \\ 0 & 0 & i & 0 \\ 0 & 0 & 0 & 1 \end{bmatrix} \tag{1.13}$$

in the basis $\{|00\rangle, |01\rangle, |10\rangle, |11\rangle\}$. If given $|\psi\rangle = 1/\sqrt{2}(|0\rangle+|1\rangle)\otimes 1/\sqrt{2}(|0\rangle+|1\rangle)$ as the input state, this gate will yield the maximally entangled state $|\Psi\rangle = 1/2(|00\rangle + i|01\rangle + i|10\rangle + |11\rangle)$.

1.5. Photon Scattering Errors in Trapped-Ion Quantum Computers

As discussed above, stimulated Raman transitions are often used to implement trapped-ion quantum logic gates. In such setups, a pair of laser beams drives a two-photon stimulated transition between qubit states $|0\rangle$ and $|1\rangle$ through one or more intermediate states. Photon scattering during this process is unavoidable and reduces the gate fidelity, *i.e.*, how well the actual output state overlaps with the desired output state. Understanding the fundamental limit photon scattering places on achievable gate fidelity is potentially crucial for the viability of trapped-ion quantum computing.

Although photon scattering errors have been previously studied Ozeri, 2007; Uys et al., 2010; Sawyer and Brown, 2021, our group chose to revisit the topic for two reasons. First, past work produced a model of scattering that, while suitable for explaining moderate-detuning gate errors, is inaccurate at larger detunings. Second, we are interested in characterizing qubits in metastable manifolds ('m' qubits), and the previous studies did not examine such qubits. They instead

focused solely on qubits with either one or both states encoded in the $S_{1/2}$ ground manifold of trapped ions ('o' qubits and 'g' qubits, respectively).

1.5.1. Past models of Raman Scattering Error

Since 2007, the seminal study of photon scattering errors in trapped-ion qubits has been Ozeri, 2007. In that work, Raman and Rayleigh scattering errors were calculated for g qubits in most commonly-used trapped-ion species. While there was much other useful information in this study, perhaps the most important message was that there is a fundamental limit on photon scattering suppression in Raman-beam-driven logic gates in trapped ion species that have low-lying D manifolds. Put another way, it was said that photon scattering ensures that you can never reduce the gate error below a certain value. For some species, such as $^{43}Ca^{+}$ and $^{137}Ba^{+}$, this limit is large enough that it would make error correction difficult due to the high overhead demands. The limits for two-qubit gates each species are given in the Table 1.1.

$^{43}Ca^{+}$	$1.06 \cdot 10^{-4}$
$^{87}Sr^{+}$	$5.0 \cdot 10^{-5}$
$^{137}Ba^{+}$	$1.46 \cdot 10^{-4}$
$^{171}Yb^{+}$	$7 \cdot 10^{-7}$
$^{199}Hg^{+}$	$1 \cdot 10^{-7}$

TABLE 1.1. Minimum scattering error during a two-qubit gate in some commonly-used trapped-ion species. Sourced from Ozeri, 2007.

However, we discovered that these limits do not exist. Ozeri et al. found such limits because their model assumes that certain effects are negligible, but these assumptions are valid only at small detunings. The neglected effects include the detuning dependence of the scattered photon frequency and Lamb-Dicke parameter, contributions of a second scattering term, interference effects

in scattering to the metastable manifolds, and the contribution of the counter-rotating component of the laser electric field to the Raman transition rate. As shown below, including such effects changes the limiting behavior of the model, resulting in no lower bound on gate error, in contrast to the predictions of Ozeri, *et al.*.

1.5.2. Photon Scattering Errors in Metastable Qubits

The past studies of Raman scattering errors have primarily considered o and g qubits. However, in a recent proposal Allcock et al., 2021 I co-authored (this thesis presents a lot of this work, particularly in Chapter II), we showed that encoding qubits in metastable states of trapped ions ('m' qubits) has several important advantages over g and o type encodings. Since we are interested in implementing m qubits, it is important for us to characterize the photon scattering errors for such qubits. Below, we will show that the m qubit scattering error has largely the same form as in g qubits, though m qubits require longer wavelength lasers and higher power to reach the same error as g qubits at the same detuning.

CHAPTER II

OMG ARCHITECTURE

Typically, ion trap qubits have at least one of their states encoded in the ground manifold. When both states are so encoded, we call it a g qubit ('g' for 'ground'); when one state is in the ground manifold, and the other is in some higher manifold, we call is an o qubit ('o' for 'optical'). In these schemes, you generally need to load the trap with two ion species: one for your qubit operations, the other for sympathetic cooling. This is because if you loaded the trap with just one species and attempted to drive cooling transitions in one of the ions in the chain, you will also cause scattering in the qubit ions and destroy their coherence. Loading two species solves this since you can cool on a transition of one species with a wavelength at which the other species is unlikely to scatter light.

While the multi-species approach has many benefits, it also has several drawbacks. For example, it requires more lasers, complicated interspecies operations, and more atomic sources Tan et al., 2015; Bruzewicz et al., 2019; A. C. Hughes et al., 2020. Additionally, it has multiple downsides due the mass inequality of the different ion species. First, you have to concern yourself with the order of the ions in the chain. This is because different ion species ordering can alter the mode structure. Also, practically speaking, mixed species approaches require a specific ordering of the ion species in the chain. This is to ensure that the ion is at the position of maximum intensity for its respective driving lasers. This is a drawback because enforcing the desired ion order requires relaxing the ion chain until it assumes the sought-after form. This procedure works well in a small-scale experiment, but may be be difficult to automate at scale in a

proper quantum computer. Second, cooling is less efficient in multi-species chains, due to their different masses. Third, different ion species will generally have different sensitivities to stray static fields, which will shift the ions away from their equilibrium position by different amounts, resulting in a relative position vector that is no longer aligned with the trap axis. Fourth, gradients in the time-averaged rf potential and trap anharmonicities can change the inter-ion spacing since different species will experience a different strength from the ponderomotive potential. Finally, it is somewhat challenging to transport multi-species ion chains without substantial motional excitation, though this is not completely infeasible (see, *e.g.*, Burton et al., 2023).

It would therefore be desirable to implement a scheme that allows ion trap quantum computing in a single ion species. In collaboration with MIT, MIT Lincoln Labs, and UCLA, we proposed and implemented such a qubit scheme: the *omg* qubit scheme Allcock et al., 2021 (some experimental work towards implementing these qubits has been conducted by a group at Tsinghua University Yang et al., 2022).

2.1. Metastable qubits

To begin to understand the usefulness of the *omg* scheme, we must first study the m qubit. The m qubit is simply a qubit with both states encoded in the Zeeman or hyperfine sublevels of a metastable manifold in the trapped ion. A diagram of the m qubit position in energy space, along with parallel depictions of o and g qubits, is given in 2.1. For singly-ionized alkaline earth metals, such as Ca^+, we are interested in the metastable $D_{5/2}$ manifold. In other ion species, other metastable manifolds are also viable, such as the $F_{7/2}$ manifold of Yb^+ Ransford

et al., 2021. In this work, I will be focusing on $D_{5/2}$ metastable qubits since they are what we have studied in our lab.

While they are necessary to implement single-species ion trap quantum computing, there are a few drawbacks to using metastable qubits. First, they have a finite lifetime. For example, the $D_{5/2}$ manifold of Ca^+ lives for about 1.2 seconds. This does not seriously limit that manifold's potential for encoding qubits however. Since most quantum logic gates take on the order of microseconds, potentially millions of operations can be performed within the lifetime of the $D_{5/2}$ manifold.

Secondly, preparation and readout are slightly more complicated than in g qubits. Optical pumping schemes can be used for preparation and readout m qubits, but more lasers are required to shelve and deshelve population in the $D_{5/2}$ manifold. However, I performed Python simulations of preparation and readout for m in the $D_{5/2}$ manifold on $^{43}Ca^+$ before we began trapping ions in our lab, and confirmed that they did not limit the viability of such qubits. I concluded that greater than 99% preparation and readout fidelity could be achieved, with optical pumping taking around only $100\,\mu$s.

2.2. *omg* architecture

The utility of the *omg* qubit scheme comes mainly from the separation of g and m qubits in Hilbert space. This separation lets us divide the various tasks of quantum computing among the different qubit encodings. Here we will discuss three modes for *omg* qubits. We will characterize each mode by an ordered triple, $\{q_1, q_2, q_3\}$ with $q_i = o, m$ or g) and where q_1 corresponds to which encoding is used for state preparation, q_2 which encoding is used for gates, and q_3 which encoding is used for storage. The three modes we will discuss are the $\{m, m, m\}$ mode, the

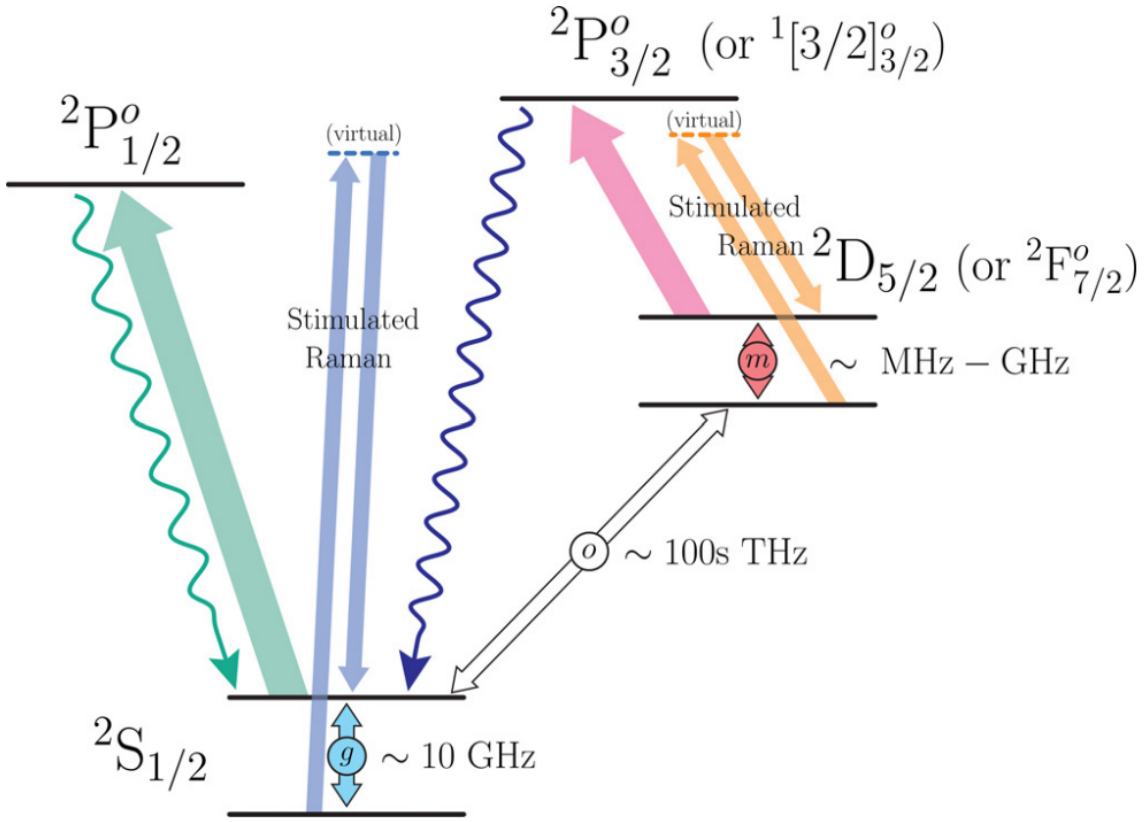

FIGURE 2.1. The typical structure of alkaline earth ions, including relevant transitions. The $S_{1/2} \longleftrightarrow P_{1/2}$ transition is used for dissipative operations (laser cooling, state preparation, and readout). The o qubit transition is electric dipole (E1) forbidden and typically requires a narrow linewidth laser. Figure taken from Allcock et al., 2021.

$\{g, m, g\}$ mode, and the $\{m, g, m\}$ mode. A diagrammatic explanation of these modes is given in Figure 2.2.

2.2.1. The $\{m, m, m\}$ Mode

The main motivation for the $\{m, m, m\}$ mode is that g qubits are a natural choice for dissipative operations like laser cooling, state preparation, and readout. It is therefore natural to consider using m qubits for most of the unitary

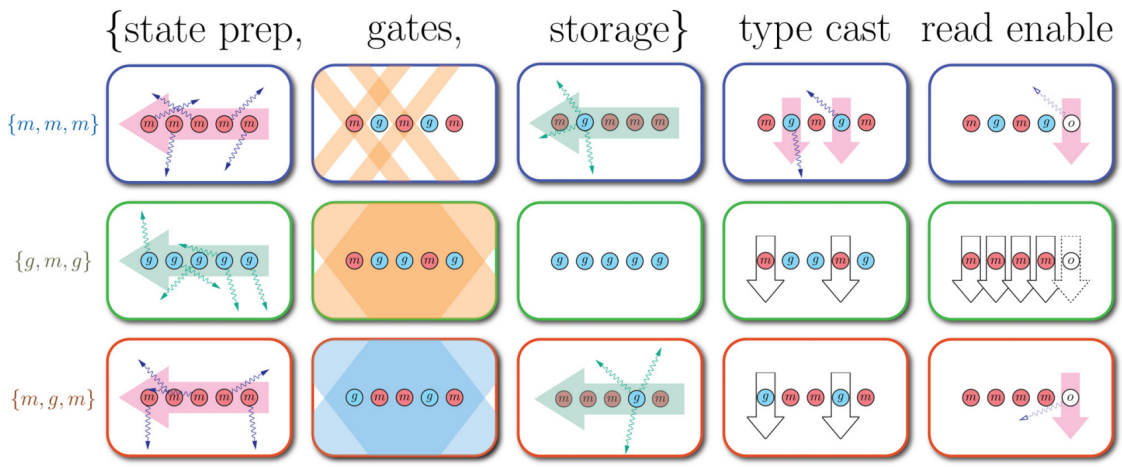

FIGURE 2.2. Various *omg* schemes. Figure taken from Allcock et al., 2021.

operations. As shown in Figure 2.2, gates in this mode would be performed by individually addressing the m qubit ions with Raman laser beams.

Conveniently, because all coherent operations take place in m qubits in this mode, no coherent transfer between m and o or g qubits is necessary. This, in turn, means that all requisite operations may be accomplished using only electric-dipole transitions, and, therefore, the technologically challenging implementation of narrow linewidth lasers for, *e.g.*, electric-quadrupole transitions is not strictly necessary. It is also worth noting that this mode has the advantage of allowing for dissipitative operations such as laser cooling to be performed on g qubits during single-qubit gates on m qubits in the same ion crystal.

The primary drawback of using this mode is the limited lifetime the metastable states. However, for many species, including Ca^+, the lifetime is long enough that it will not be a limiting error for gate performance. Since the $D_{5/2}$ manifold of $^{40}Ca^+$ has a lifetime of $\sim$1.2 s, for a gate time of 1-10 μs, this would give an error between 1.2×10^{-6} and 1.2×10^{-5}.

2.2.2. The $\{g, m, g\}$ Mode

The second mode we will consider is characterized in the middle row of Figure 2.2. Here, coherent transfer between o, m, and g encodings can be achieved with individually addressable, narrow linewidth laser beams that drive electric-quadrupole or electric-octopole transitions in the ions. Global beams may then be used to implement logic gates.

The main upside of this mode is that it exploits the stability of g qubits to protect stored information during logic gates. One disadvantage, of course, is that this scheme requires high-fidelity coherent population transfer on quadrupole or octopole transitions.

2.2.3. The $\{m, g, m\}$ Mode

The last mode we will consider is described in the final row of Figure 2.2. This is the first of the three modes we have considered in which gates are performed on g qubits. Just as in the $\{g, m, g\}$ mode, this mode requires that we be able to coherently transfer individual ions from a g to an m qubit, and vice versa. This capability would be required for gates and helpful for cooling and readout, although the latter may be accomplished with incoherent methods.

This mode shares a common advantage with the $\{g, m, g\}$ mode: the storage qubits are protected from the laser light, so we may apply the laser beams globally for gates. The difference is that only the qubits need to be converted between m and g, which is a less stringent requirement than in the $\{g, m, g\}$ mode. However, keeping the ions in the metastable manifold by default means that this mode is more susceptible to the finite lifetime of the m qubit.

2.3. Two-Qubit Gates in m Qubits

Two-qubit gates have recently been performed in m qubits for the first time. One such gate was performed by University of Oxford in m qubits encoded in the metastable $D_{5/2}$ manifold of $^{88}Sr^{+}$ Bazavan et al., 2023. They implemented it with the $S_{1/2} \longleftrightarrow D_{5/2}$ quadrupole transition and achieved a gate fidelity of 0.859(5).

Another gate was performed at Innsbruck Roos et al., 2004. Technically, the gate was not performed in m qubits, but it did generate entangled m qubit states. The group performed an entangling gate on $S_{1/2}$, $D_{5/2}$ o qubits. These qubits were then converted to m qubits with single qubit operations.

Our group has also made progress towards implementing m qubit two-qubit gates. Unlike previous implementations, we are applying a two-qubit gate directly in m qubits using stimulated-Raman transitions. In Chapter VII, I report on our progress towards implementing such a gate.

CHAPTER III

EXPERIMENTAL METHODS

Below, I describe the various components of our experimental apparatus.

3.1. Ion Trap

We use a linear Paul trap in our lab. The schematic of our trap is shown in Figure 3.1. A view of the physical trap is given in Figure 3.2. The ion-electrode separation 'r_0' is 0.75 mm, the needle-to-needle spacing 'a' is $\sim$3 mm, and the rods have a diameter '$2r_e$' of 0.5 mm. In order to minimize the rate of background gas collisions, we keep the trap under ultra-high vacuums, reaching pressures of order 10^{-11} Torr.

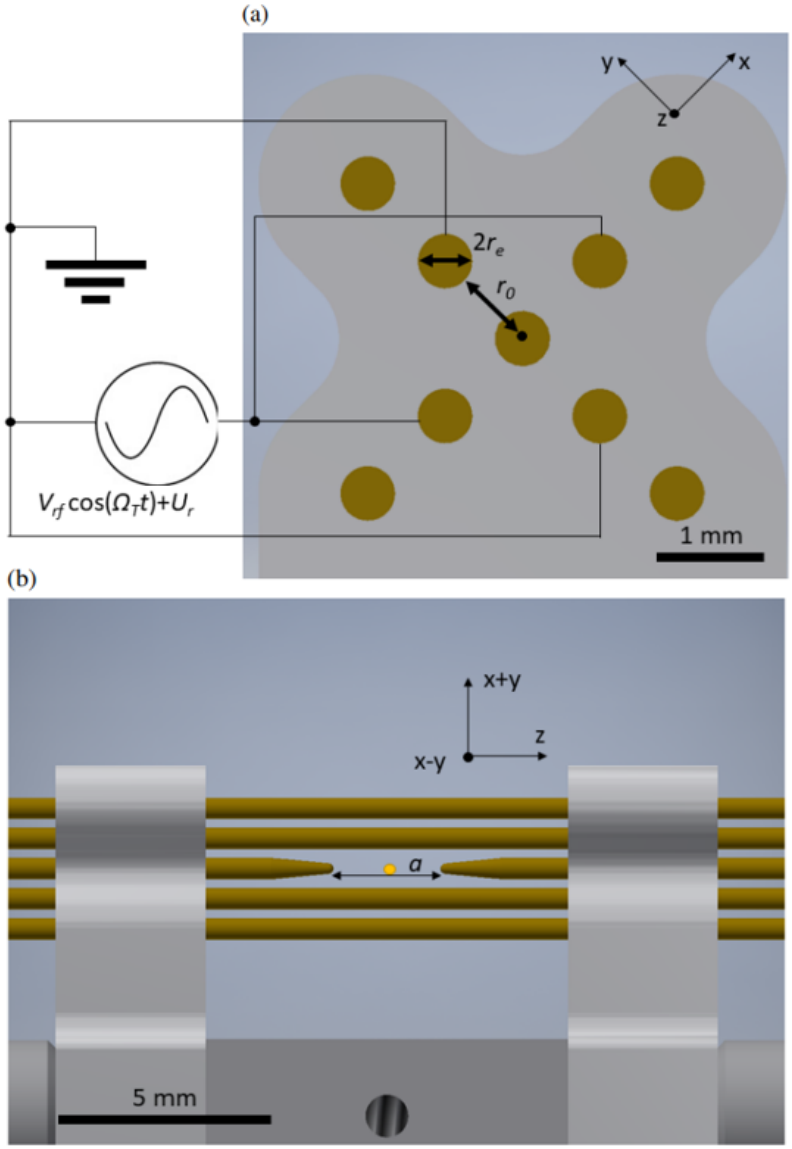

FIGURE 3.1. (a) Schematic view of our linear rod trap along the trap axis. The gold circles are cross-sections of the different rods in the trap. In the figure, r_e is the electrode radius and r_0 is the trap axis to electrode surface distance or trap radius. Two opposing inner rods are connected to the oscillating voltage V_{rf} at frequency Ω_T with offset U_r and the other two inner rods are held at ground. (b) Schematic side view of the linear rod trap where a is the tip-to-tip distance between the needles and the yellow dot is an oversized ion giving its approximate location in the trap. Following the axes in figure (a), the upward direction in (b) is the $(x + y)$ axis and the out-of-the-page direction is the $(x - y)$ axis.

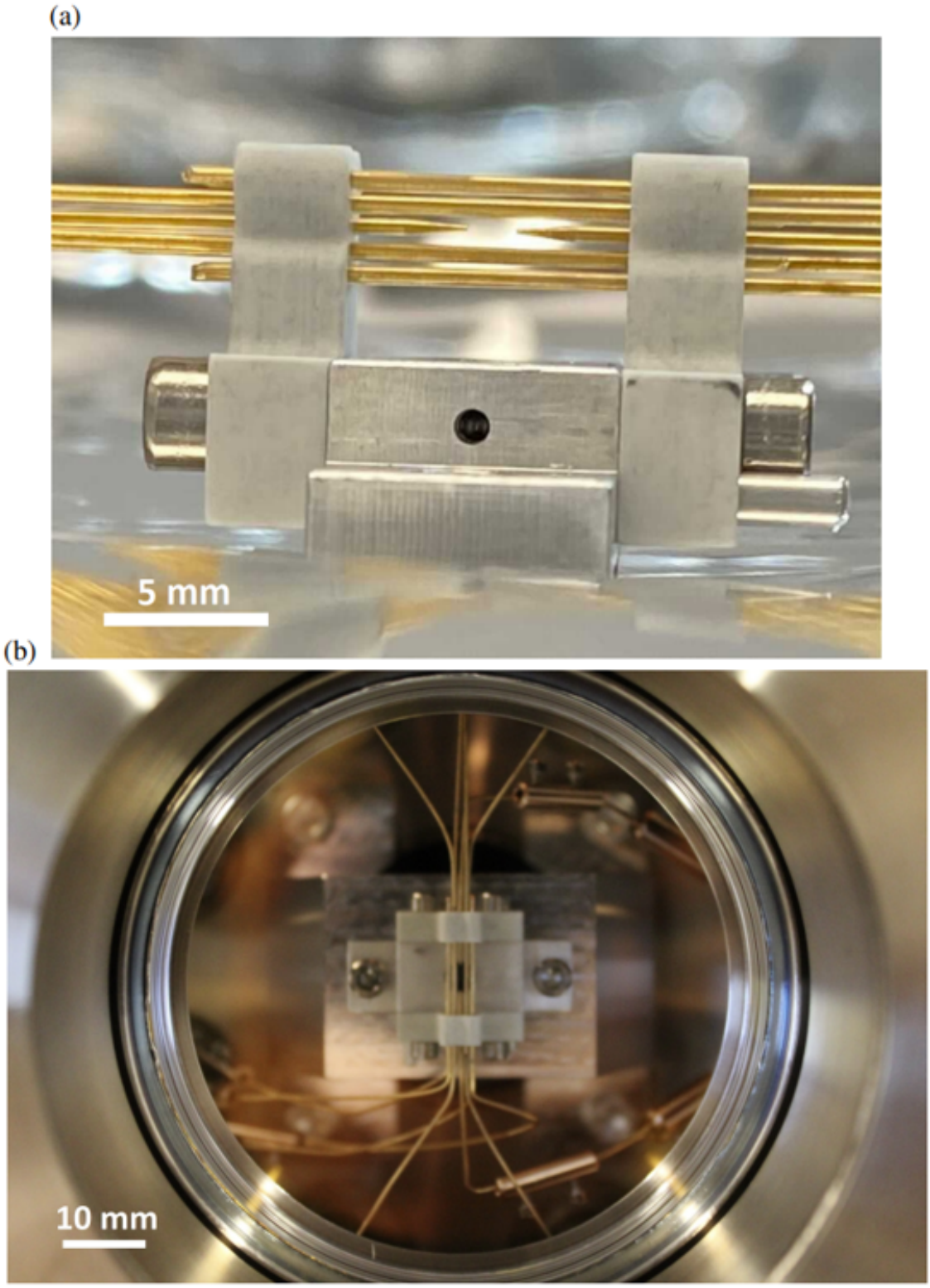

FIGURE 3.2. (a) The assembled rod trap. (b) The rod trap mounted in the vacuum chamber, as seen through a viewport.

3.2. Magnetic Field

When working with trapped ions, it is necessary to apply an external magnetic field to lift the degeneracy of the atomic sublevels. We accomplish this by supplying a current to four rectangularly coiled wires, each of different sides of the spherical octagon chamber in which the trap sits. Additionally, there is one circularly coiled wire oriented perpendicular to the rectangular coils. One of the rectangular coil pairs, acting in concert with the Earth's magnetic field, primarily determines the magnetic field magnitude and direction, and, therefore, the ion's quantization axis. The remaining coils allow us to finely adjust ("shim") the magnetic field to align it relative to the incoming laser beams. We supply a 0.5 A current with a low-noise source. This setup allows us to generate a 0.498 G magnetic field, which creates a Zeeman splitting in the $D_{5/2}$ manifold of 2.63 MHz.

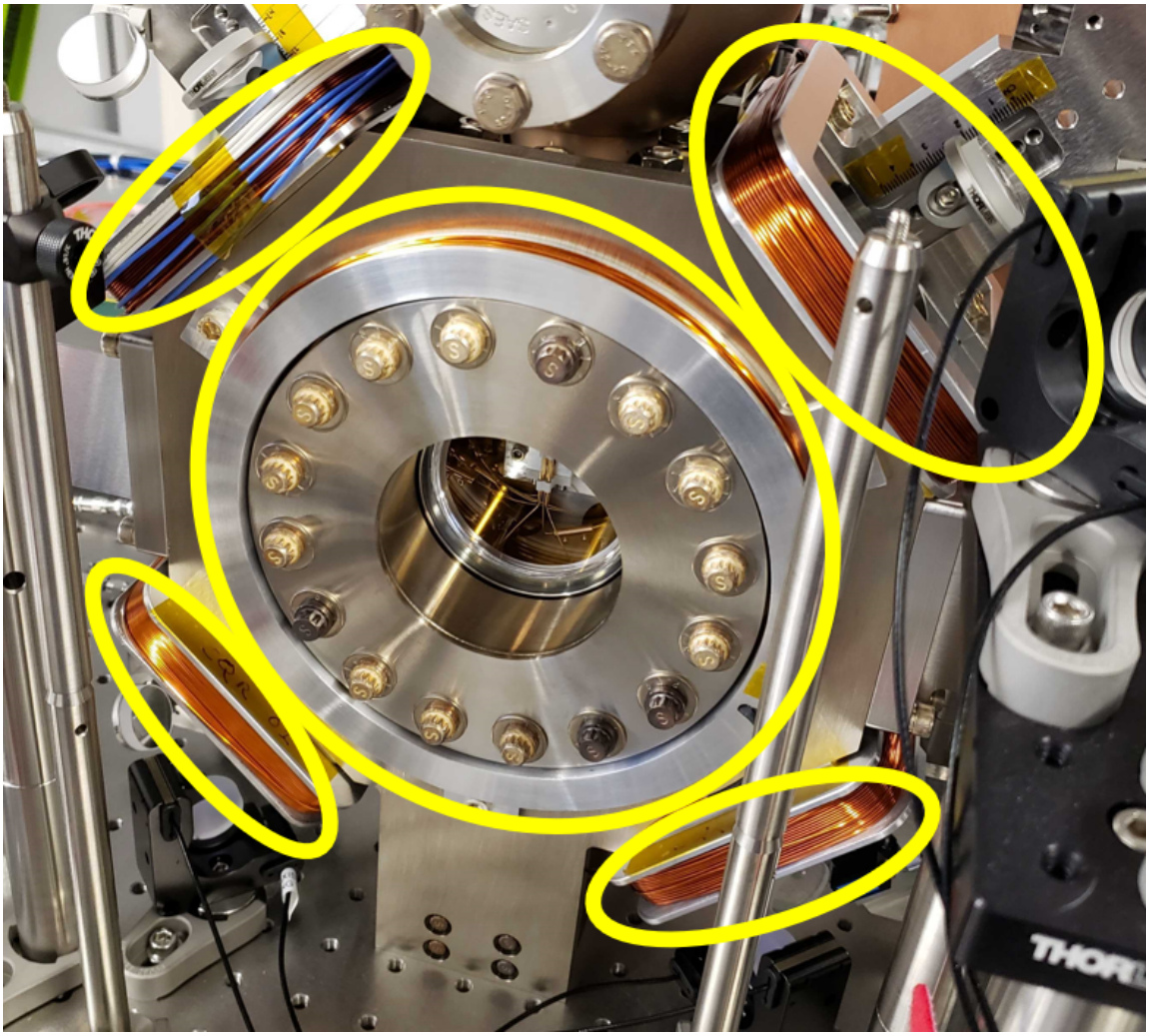

FIGURE 3.3. Coils of copper wire used to generate our trap's magnetic field

3.3. Ion Detection

We use an imaging system to detect ions and the state of the qubit. The imaging system is optimized to collect 397 nm photons, which we generate when we drive the $S_{1/2} \longleftrightarrow P_{1/2}$ transition. The imaging system has a numerical aperture (NA) of 0.4 and a photomultiplier tube (PMT) efficiency of ∼0.3. The total measured click efficiency of the system is 1.2%.

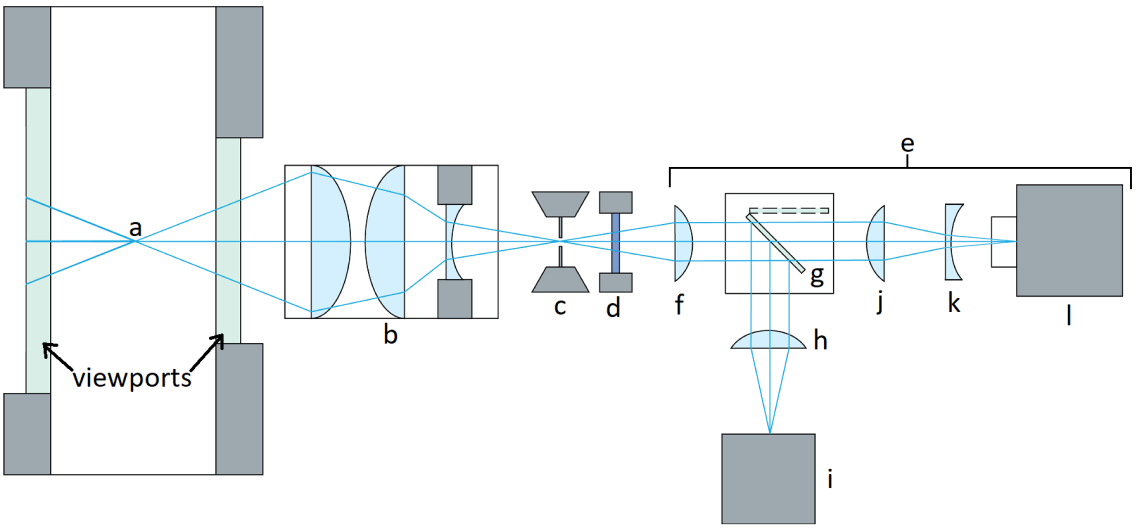

FIGURE 3.4. Schematic of the ion detection system. Component indicated by 'a' is the ion in vacuum, 'b' is the aspheric objective, 'c' is the adjustable aperture, 'd' is the filter holder, 'e' is the second stage (re-imaging Lenses and items f-l), 'f' is the slit imaging lens, 'g' is the flipper mirror, 'h' is the photomultiplier tube (PMT) imaging lens, 'i' is the photomultiplier tube, 'j' is the convex camera imaging lens, 'k' is the concave camera imaging lens, and 'l' is a CMOS camera with 3.45 micron resolution.

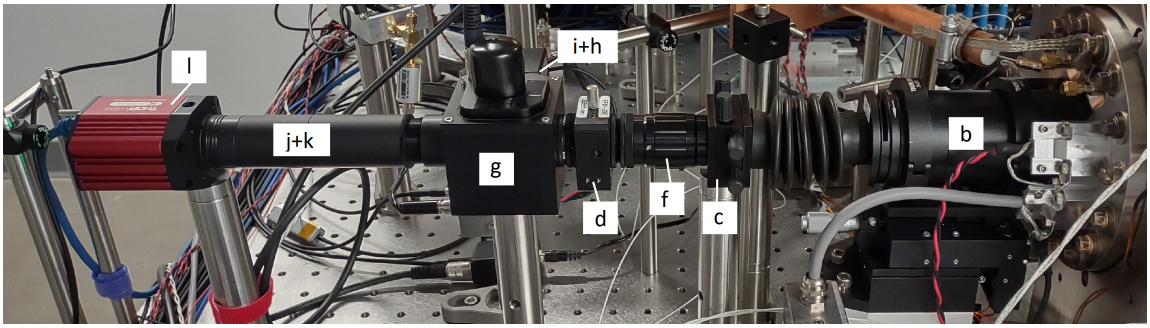

FIGURE 3.5. The actual ion camera system.

3.4. Trap rf Drive

The rf chain provides the signal needed to provide stable confinement for the ions as well as reducing noise that contributes to motional decoherence. The rf chain is comprised of multiple components. One key component is the

Squareatron, developed by Jeremy Metzner in collaboration with University of Oxford Metzner, Allcock and Ballance, 2020. The Squareatron behaves like a saturated amplifier, taking its input clock signal (which it receives from an arbitrary wave generator, or AWG) and stripping the harmonics off with a bandpass filter (BPF) to return stable rf signals. It has an output power of about 10 dBm and can be tuned roughly 1 dBm with a digital to analog converter (DAC) board. The purpose of the Squareatron is to reduce amplitude modulation noise to keep the ion's secular frequency stable. Additionally, the rf chain has a helical resonator (coupled to a 1 W amplifier to get necessary power) with a step-up of $\sim$100$\times$ and a Q of $\sim$150. This resonator impedance-matches the amplifier to the ion trap and provides modest filtering. The Squareatron and amplifier are kept in an insulating box with a thermostat *Thermostat* 2022 which helps to stabilize the ion's motional frequency.

3.5. Laser Systems

Our lab's laser systems are stored in one room with three racks: a rack containing drawers which house our Toptica Littrow ECDL lasers (Model 'DL Pro'), a rack containing Toptica laser controllers (Model 'DLC Pro'), and a rack housing the wavemeter. The setup of the room can be seen in Figure 3.6. The setup of a laser rack drawer is shown in Figure 3.7. In each drawer, a Toptica laser in mounted to an optical breadboard. The Toptica laser parameters are set by the controllers mounted in the adjacent rack. Upon emission from the laser, the beam is redirected by a periscope to be level with half-inch optics mounts. In order to prevent amplified stimulated emission a few nanometers away from the lasing mode from reaching the optical fiber, the beam is then reflected off of a diffraction

grating before being sent down a path of polarizing beam splitters, where half-waveplates allow us to adjust how much power goes down each arm. These separated beams are then coupled into fibers to be delivered to the AOM boards in the trap rooms. One of the beams on each board is sent to the wavemeter, which serves to stabilize the laser frequencies.

FIGURE 3.6. The laser racks. Contains our breadboard laser systems used for ionization, cooling, preparation, and readout.

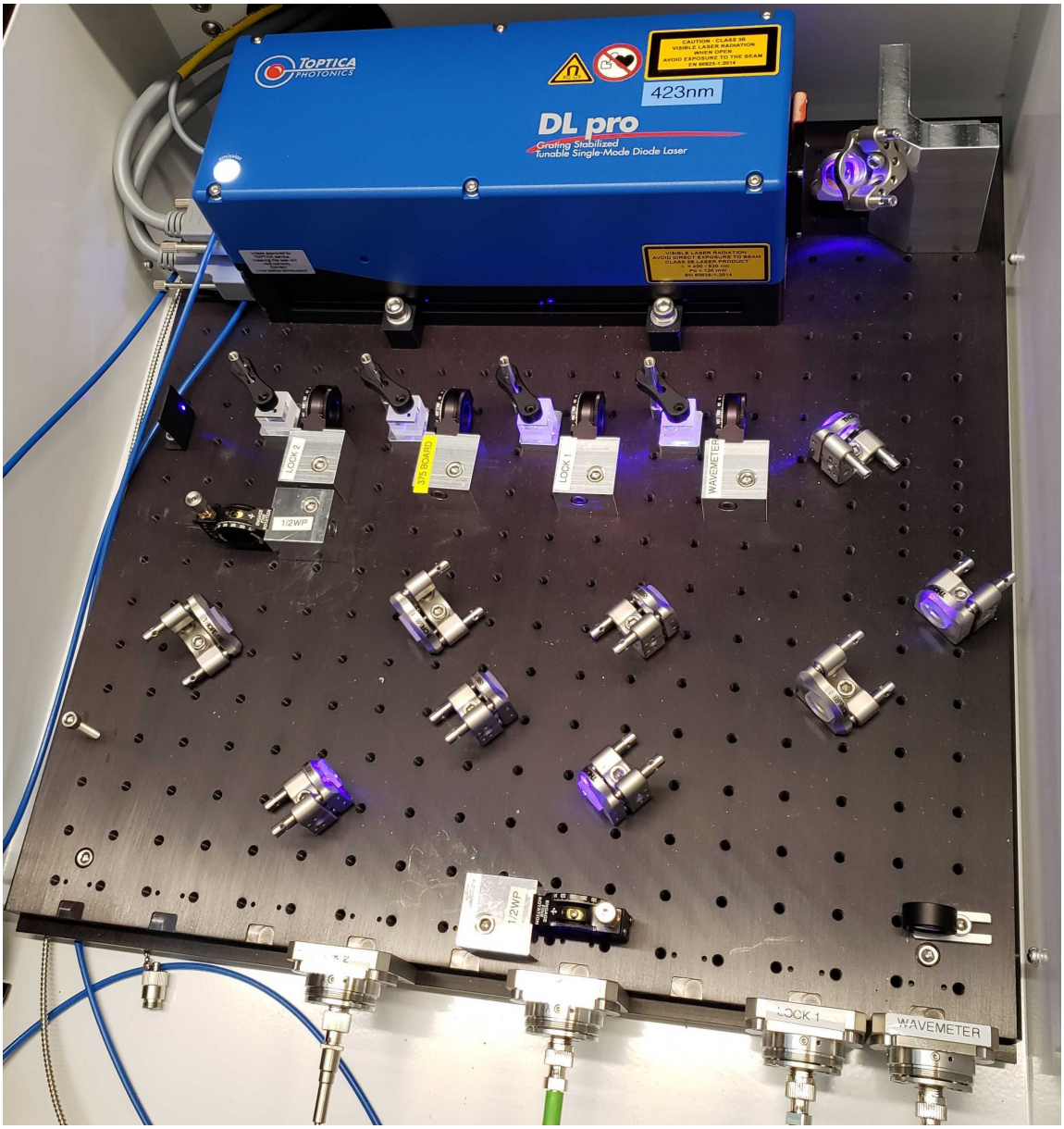

FIGURE 3.7. The inside of a laser rack drawer. The beam from a Toptica laser is picked off by multiple polarizing beam-splitters and is coupled into multiple fibers to be sent to different AOM racks in a separate room.

3.6. AOM Boards

Because our experiments take place on the scale of microseconds, we need a way to rapidly turn our lasers on and off. Our solution is to use acousto-optical modulators (AOMs).

AOMs are composed of a piezoelectric material attached to a crystal. When an rf signal is applied to the piezoelectric material, it causes it to vibrate and generate a sound wave in the crystal. When laser light passes through the AOM, the interaction of the light with the vibrating crystal creates discrete, diffracted beams with frequencies shifted by some integer multiple of the rf frequency. A picture of the inside of one of our lab's AOMs is given in Figure 3.8.

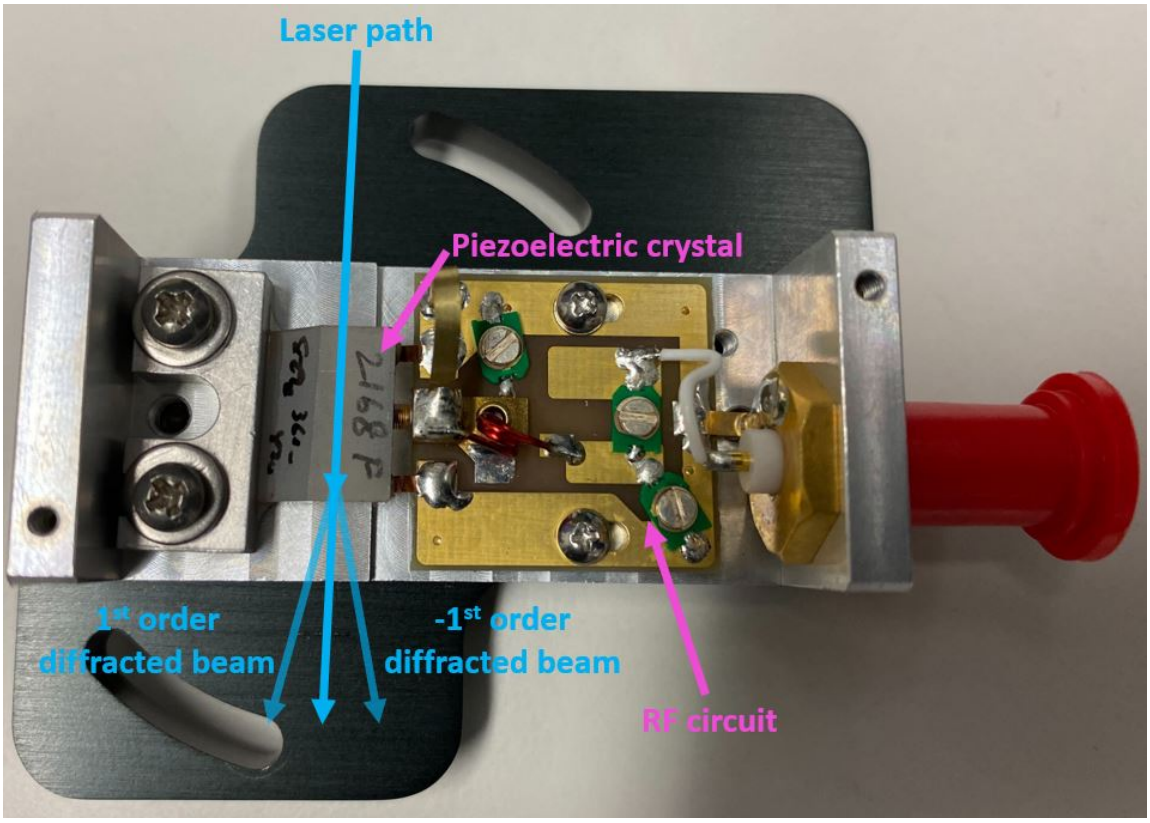

FIGURE 3.8. The inside of an AOM. The circuit produces an ac current that creates a sound wave using a sheet of piezoelectric material attached to the crystal. The circuit is controlled via the SMA connector on the right side.

The optical switch functionality of the AOM comes from the separation between the diffracted beams. To create our switch, we simply position a slit in the beam path that allows through the 1^{st} or -1^{st} diffracted beam, but blocks the 0^{th} order. This means that the laser light reaches the ion only when the AOM is on. Since the rise time of our AOMs is tens of nanoseconds, they provide optical switches which are more than fast enough for our experiment's requirements. Some of our AOM paths are double-pass. This means that the laser beam is sent through the AOM, the 1^{st} or -1^{st} order beam is picked off, reflected, and sent back through the AOM once more. This setup has three benefits: in it, the angle of the beam is constant with changes in AOM frequency, it effectively doubles the electrical bandwidth, and there is a higher extinction ratio for the beam. This latter effect is important for some beams, as we want to ensure that we do not have leakage when the AOMs are off. For example, 854 nm light leakage could lead to $D_{5/2}$ deshelving during an m qubit experiment.

Another benefit of using AOMs is that, in conjunction with the SU servo (see Section 3.7), they allow us to control the optical power of the laser beams at the ion. This is done by feeding the SU servo the signal from the photodiodes (see Section 3.8) and having the servo adjust the attenuation of the rf signal to the AOM to maintain the desired power.

Using AOMs comes at the cost of optical power, however. We choose to use the first-order diffracted beam out of the AOM, but there is always some power in the other orders. The first-order diffraction efficiency is controllable by adjusting the rf power into the AOM. The optimal operating power is different for Isomet model 1250C-829A "blue" AOMs is shown in Figures 3.9. The blue AOM contains a TeO_2 crystal and has a center frequency of 260 MHz with a 50 MHz

bandwidth. The optimal operating power for the Isomet model 1205C-1 "red" AOMs is shown in Figure 3.10. The red AOM contains a $PbMoO_4$ crystal and has a center frequency of 200 MHz with a 50 MHz bandwidth.

It is worth noting that people commonly place AOMs directly on their optical tables and work with them there. We, however, choose to build our AOM paths on modular boards housed in rack drawers. This design idea came from the University of Oxford ion-trapping group. This design has the advantages that the AOM racks take up less space in the lab (as the drawers may be vertically stacked in a 19" rack) and are more stable (due to the low beam height), but has the drawback that the optics' positions are less reconfigurable. One AOM rack board (the 393 nm/397 nm board) is shown in Figure 3.11.

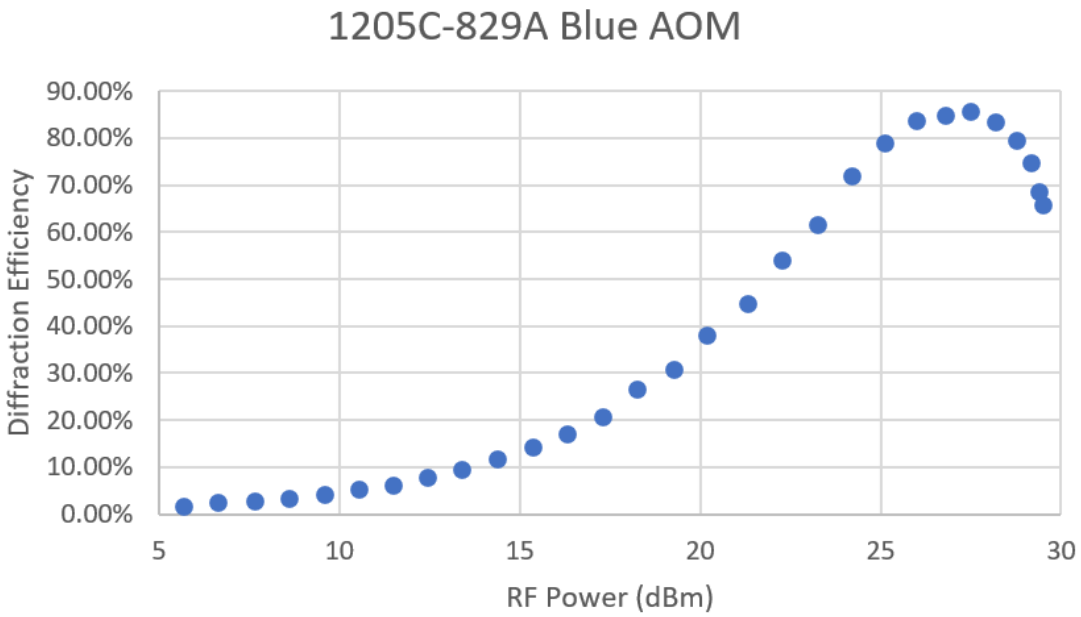

FIGURE 3.9. Model 1205C-829A "blue" AOM first-order diffraction efficiency as a function of Urukul attenuation.

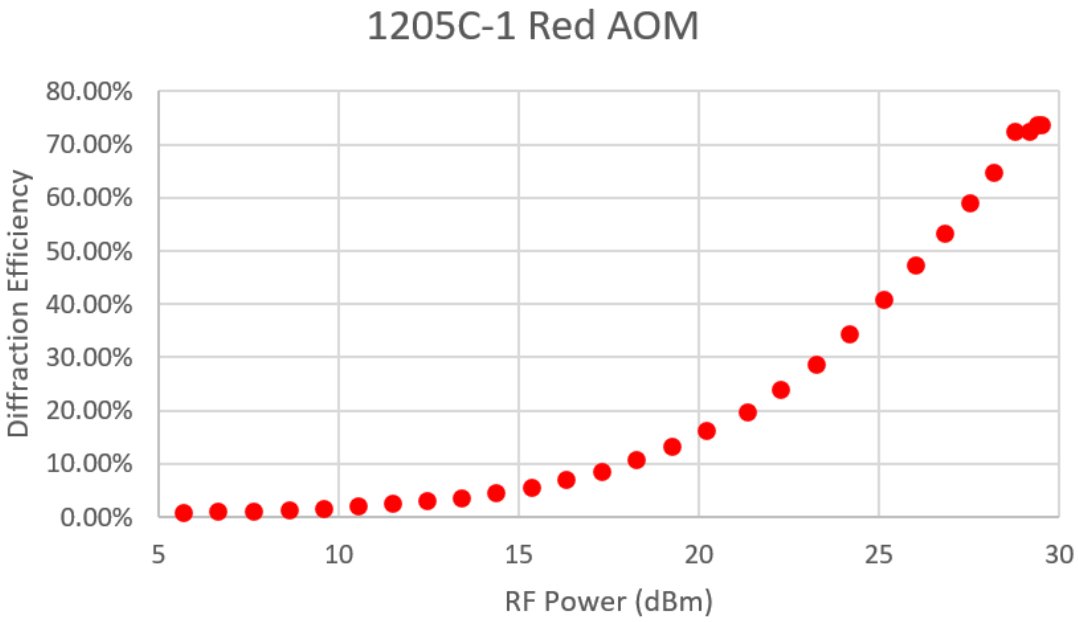

FIGURE 3.10. Model 1205C-1 "red" AOM first-order diffraction efficiency as a function of Urukul attenuation.

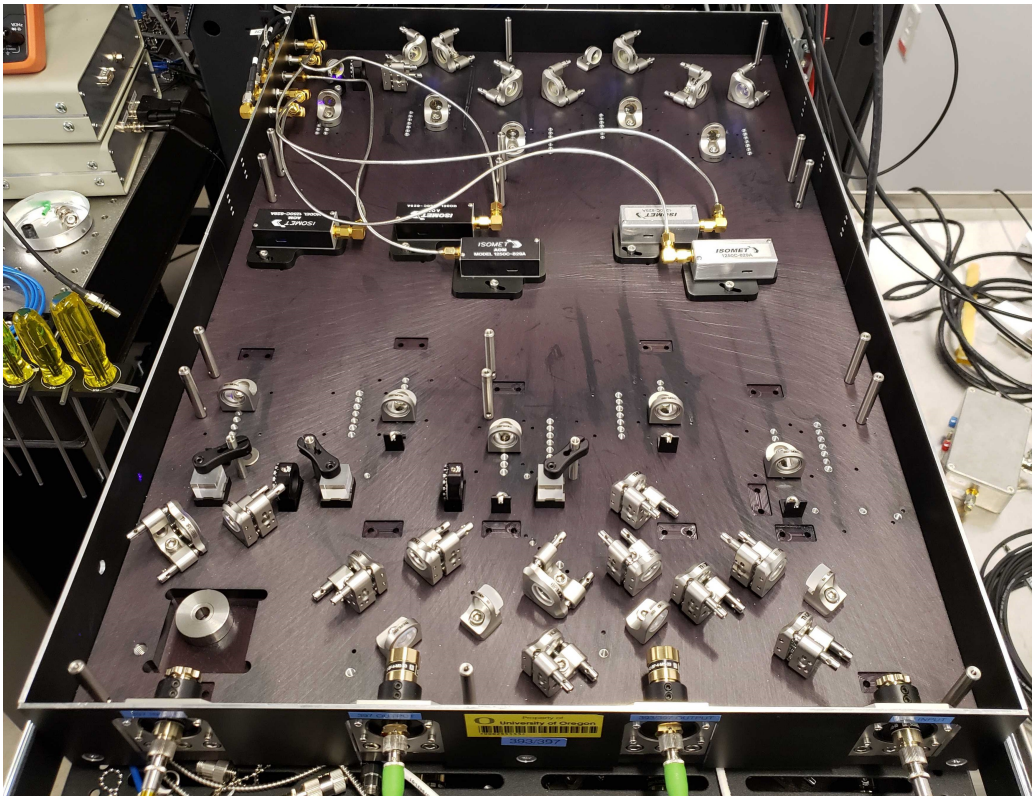

FIGURE 3.11. Example of an AOM rack board in our lab.

We have three AOM boards, and their design is shown in Fig 3.12. More detailed beam path diagrams are given in Figures 3.13. The top-most board generates our 850 nm and 854 nm pump beams. We use these beams to pump population out of the $D_{3/2}$ and $D_{5/2}$ manifolds. The board just below that is designed to control the 854 nm input to the top board as well as the 866 nm beam. The latter beam is used in Doppler cooling (by driving $D_{3/2} \longleftrightarrow P_{1/2}$ transitions) and for depumping the $D_{3/2}$ population. The bottom board of the diagram controls our 397 nm and 393 nm laser beams. The 397 nm beams are for optical pumping, cooling, and detection on the $S_{1/2} \longleftrightarrow P_{1/2}$ transition, and the 393 nm beam is for optical pumping on the $S_{1/2} \longleftrightarrow P_{3/2}$ transition.

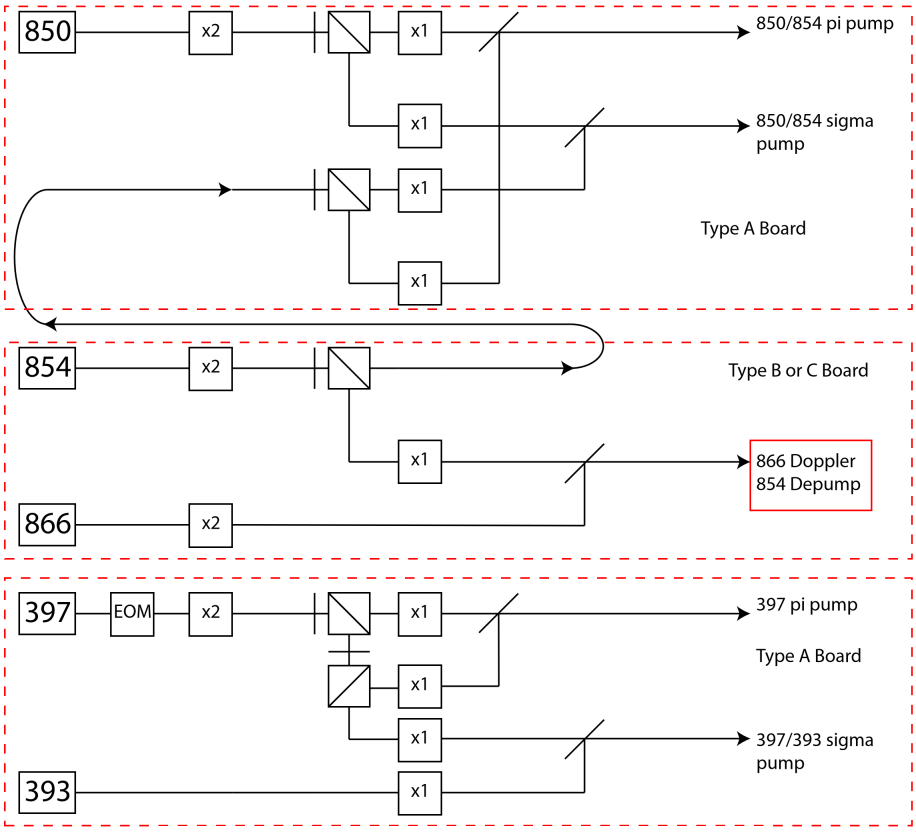

FIGURE 3.12. The three AOM boards. The boards are for dissipative operations, such as cooling, preparation, and readout. The boxes labeled "1×" and "2×" correspond to single- and double-pass AOM filters, respectively.

3.7. ARTIQ

For real-time implementation and remote control of our experiments, both hardware control and data collection, we utilize the software system ARTIQ Bourdeauducq et al., 2016 (Advanced Real-Time Infrastructure for Quantum physics) and the associated hardware from Sinara Kasprowicz, Kulik et al., 2020; Bourdeauducq et al., 2016. A schematic of the ARTIQ setup is show in Figure 3.14.

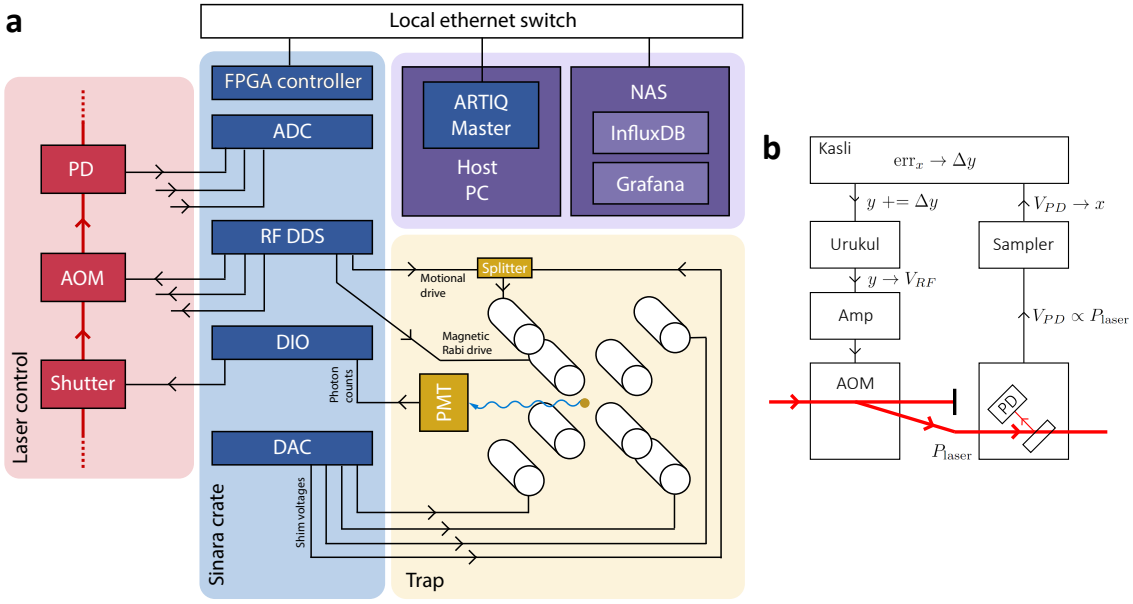

FIGURE 3.14. Schematic of the ARTIQ setup. (a) Schematic of the connections between the physical components between the subcomponents of the ARTIQ system in our lab. (b) Schematic of the SU servo system, and depiction of its feedback on the optical power measured by the photodiode. Figures made by Alex Quinn.

In terms of hardware, firstly, the host PC interfaces with an FPGA board called the "Kasli," which, along with the host, also runs the ARTIQ code. The trap electrodes are controlled by the "Zotino" board, a digital to analog converter (DAC). We use the Zotino to apply dc voltages to shim the trap electrodes and finely adjust the ion's position. We use "Urukul" direct digital synthesizer (DDS) boards Kasprowicz, Harty et al., 2022 as sources of timed rf signals, with applications to controlling AOMs, driving M1 transitions between Zeeman levels, and driving ion motion (achieved by applying an rf tone to one of the trap rods). For reading and generating digital signals, we use DIO boards. This has utility for reading photon clicks from the photomultiplier tubes and for controlling our mechanical shutters. Finally, we have the "Sampler", which is an analog to digital

converter (ADC) board. This is a component of the "Sampler-Urukul" (SU) servo system for precise control of laser beam powers on short timescales. The SU servo uses a pickoff from the laser beams (discussed in the section below) to monitor the laser power. The SU servo acts as a feedback system, adjusting the rf amplitude on the Urukul to control adjust the laser power in response to the Sampler reading.

3.8. Beam Delivery System

After the beams are sent from the laser rack room to the trap room, and there through the AOM boards, they finally reach the beam delivery system. The primary function of the beam delivery system is to get the laser beams from the output fibers (usually from the AOM boards) to the ions while ensuring we maintain the correct beam power, polarizations, and alignment on the ion. After being passing through the AOM board, the laser beam leaves the fiber via a collimator and then passes through a PBS to fix the polarization. After this, it is sent through the photodiode assembly, which picks a fraction of the beam off to monitor the beam power with the SU servo. After this, the beam is sent to the optics mounted to the "tombstone", a custom-machined component made to attach to the vacuum hardware. On the tombstone are a pair of 1" fixed mirrors and a 1" $f = 150\,\mathrm{mm}$ achromatic lens. The beam pointing is controlled by a piezoelectric-motor-controlled mirror mount, which is controllable by ARTIQ. After passing through the tombstone optics, the beam is sent to the ion. A schematic of the relevant beams passing through the trap is shown in Figure 3.15. The polarization of the beams is controlled by half- and quarter-waveplates (labeled $\lambda/2$ and $\lambda/4$ in 3.15).

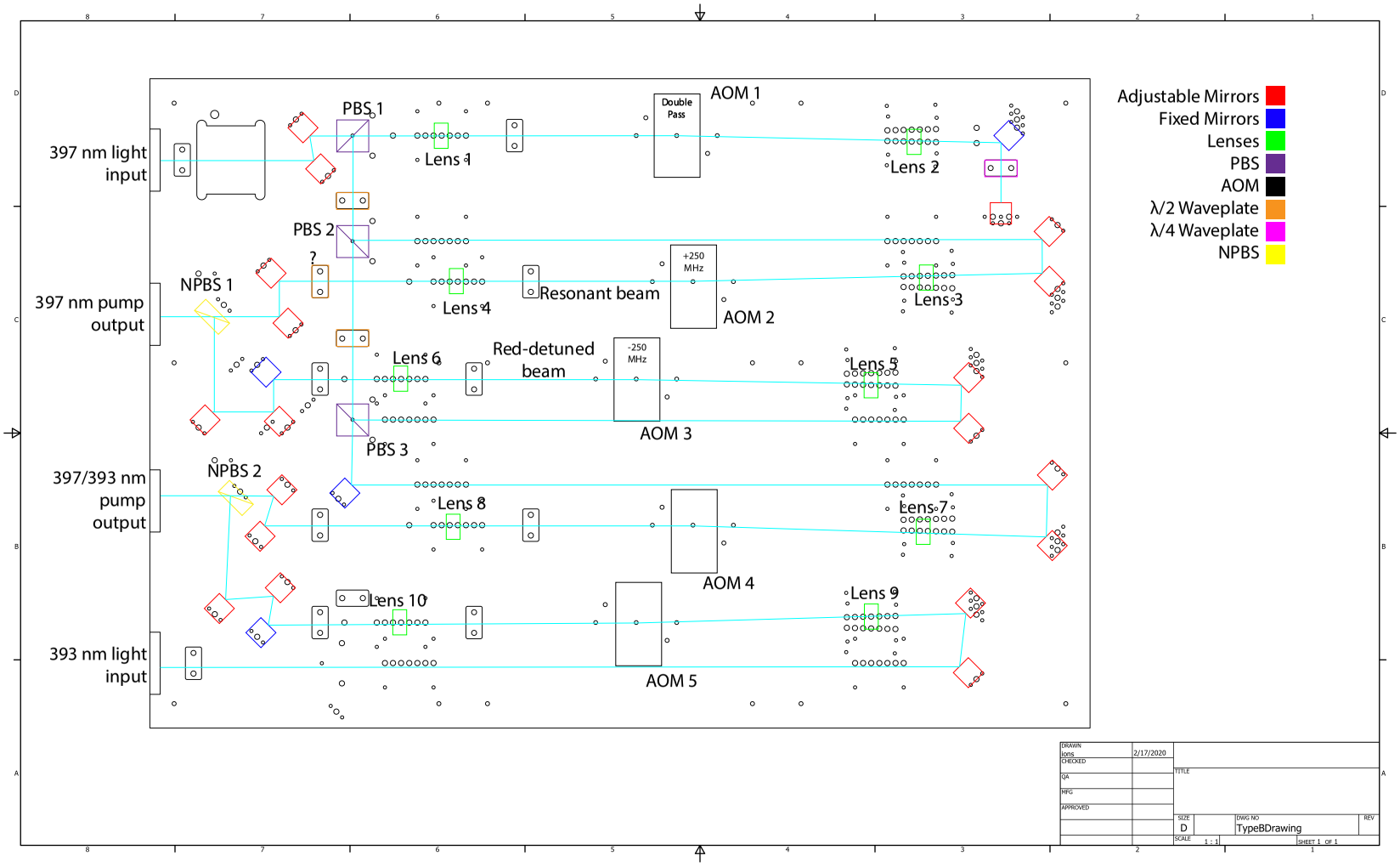

FIGURE 3.13. Optical paths on the 397/393 nm AOM control board.

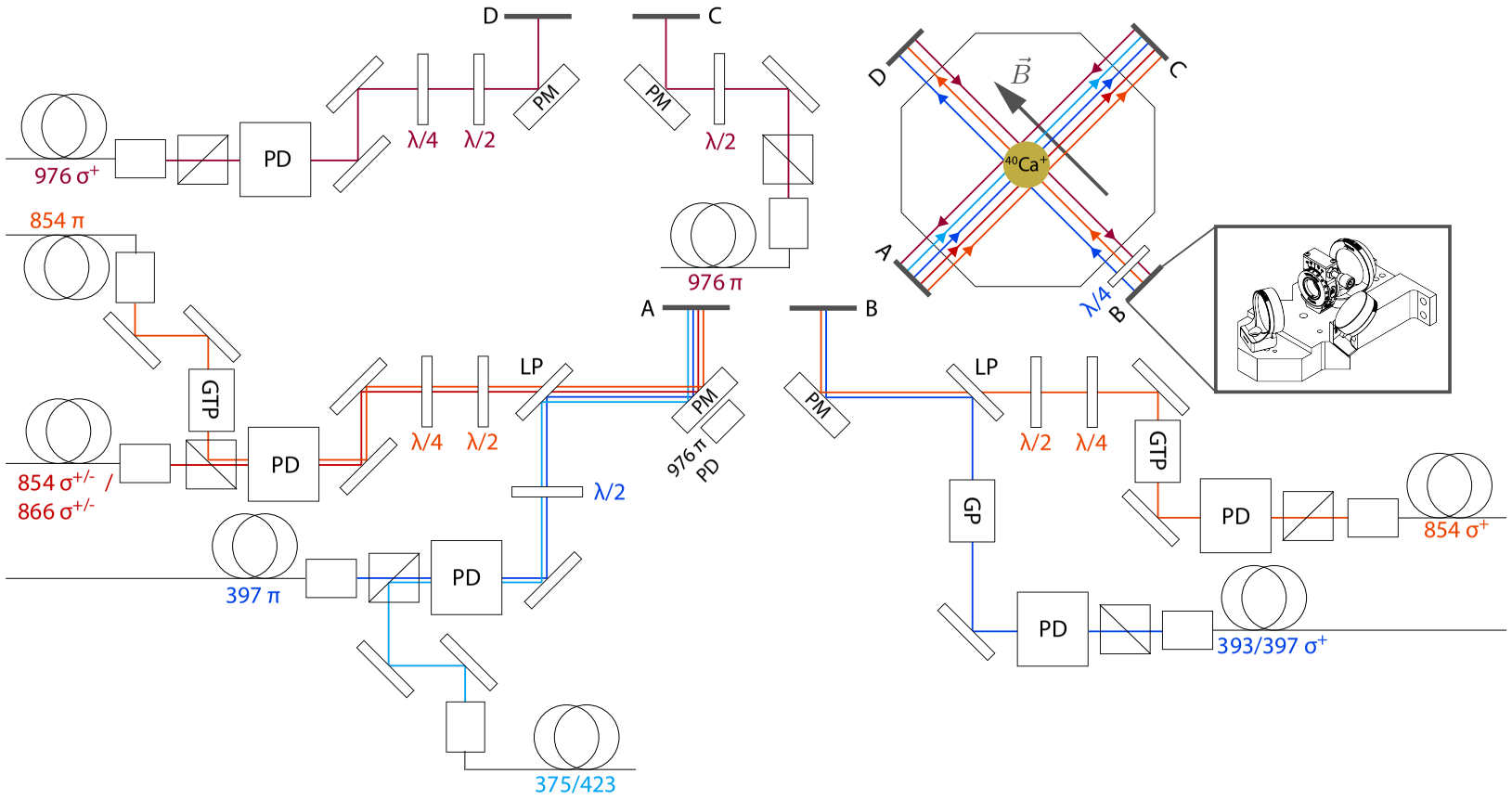

FIGURE 3.15. Schematic of beam delivery system. Path shown for each laser beam, as well as the direction they travel in the trap. Ion shown as yellow circle. Tombstone drawing shown on the right side.

CHAPTER IV

SCATTERING THEORY

Below, after describing our qubit choices and defining our model, we calculate the photon-scattering-induced errors in single-qubit and two-qubit gates in m qubits and compare them to g qubits. There are many physical differences between m and g qubits, such as the dipole coupling between the qubit states and $P_{1/2}$ that exists for g qubits but is absent in m qubits, or certain scattering terms present in m qubits that are not present in g qubits. These physical differences exert influences of varying magnitudes on the quantitative scattering error, but on net, they tend to increase the detuning from resonance required for a certain error in m qubits relative to g qubits. As for the qualitative scattering behavior, we find that the main difference between the two schemes is the existence of a lower bound on two-qubit gate errors in m qubits which is absent in g qubits. However, for all trapped ions considered in this work, this lower bound is sufficiently small (less than 10^{-4}) that low-overhead error correction is possible for Raman gates in the m qubit scheme.

After describing the overall behavior of the two different qubit schemes in the large-detuning model, we discuss the contributions of higher-lying levels to the scattering rates of the m qubit model. Additionally, for both m and g qubits, we estimate the contribution to gate error from Rayleigh scattering.

4.1. Choice of Qubit

In what follows, we consider a number of common trapped-ion qubit species: $^{9}\mathrm{Be}^{+}$, $^{25}\mathrm{Mg}^{+}$, $^{43}\mathrm{Ca}^{+}$, $^{87}\mathrm{Sr}^{+}$, $^{133}\mathrm{Ba}^{+}$, $^{135}\mathrm{Ba}^{+}$, $^{137}\mathrm{Ba}^{+}$, $^{171}\mathrm{Yb}^{+}$, and $^{173}\mathrm{Yb}^{+}$. We

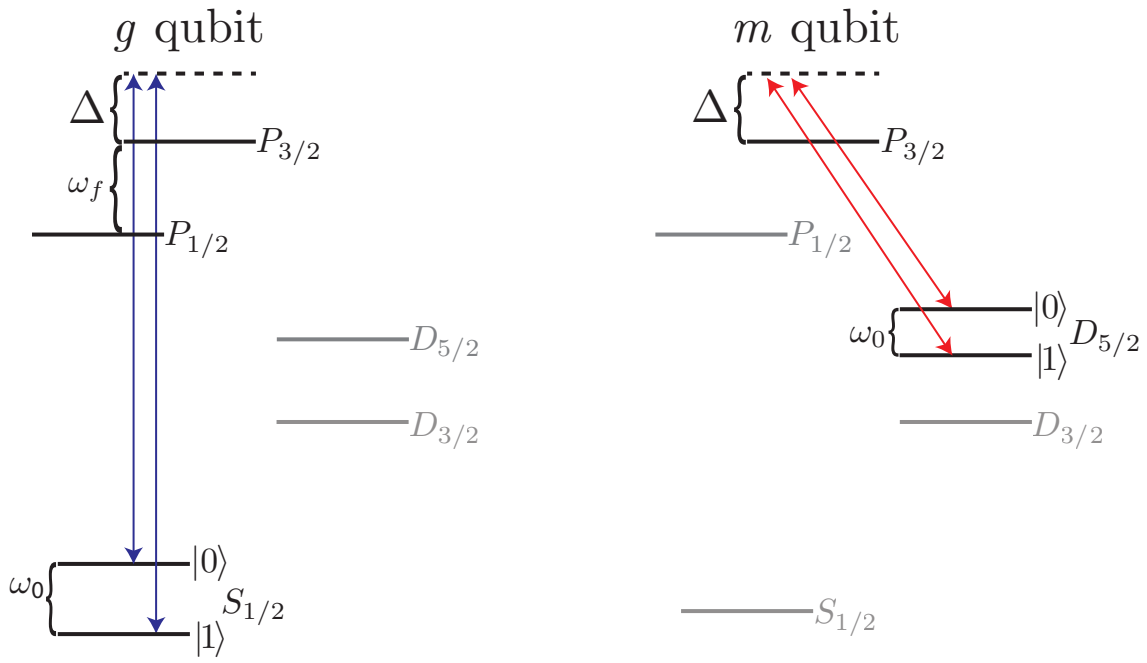

FIGURE 4.1. The g qubits are encoded in hyperfine sublevels of the $S_{1/2}$ manifold with gates often performed via Raman transitions; m qubits are encoded in the hyperfine sublevels of the $D_{5/2}$ level with gates performed in the same way. Manifolds that do not participate in qubit operations in the respective schemes are shown in gray. Figure from Moore, Campbell et al., 2023.

present results for g qubits in all species. For m qubits, we perform calculations only for the species with a sufficiently long-lived ($\gtrsim$ 1 second lifetime) $D_{5/2}$ manifold: $^{43}Ca^+$, $^{87}Sr^+$, $^{133}Ba^+$, $^{135}Ba^+$, and $^{137}Ba^+$ (see [1] for further discussion). The attributes of all these ion species are given in Table 4.1.

For our qubit choices, we use hyperfine 'clock' qubits for both m and g qubits, due to their insensitivity to magnetic field noise and corresponding suppression of Rayleigh dephasing Tan, 2016 (see [2] for the definition of 'clock

[1] Yb^+ has an $F_{7/2}$ manifold with a years-long lifetime Allcock et al., 2021, making it a suitable candidate for m qubits. However, this system is more complex and would require a separate analysis, so we only present g qubit results for Yb^+.

[2] A clock qubit is defined as having a qubit frequency that does not change with changes in the B-field (to first order); the B-field magnitude at which this occurs can be called the clock point, and the B-field direction defines the quantization axis.

qubit'.). We give our qubit choices (along with other qubit details) explicitly in Table 4.1 in terms of F (hyperfine angular momentum quantum number) and m_F (corresponding angular momentum projection quantum number). Since g qubits are already well-established, we simply follow Ozeri, 2007 in their encoding scheme. As for m qubits, we choose states that should be relatively easy to prepare and readout, as well as give consistent behavior across all m qubit species for studying the scattering errors the states

$$|0\rangle = |D_{5/2}, F = I + \frac{5}{2}, m_F = \pm|I + \frac{5}{2} - 1|\rangle$$

and

$$|1\rangle = |D_{5/2}, F = I + \frac{5}{2} - 1, m_F = \pm(I + \frac{5}{2} - 1)\rangle$$

(depending on the sign of relevant hyperfine splittings), where F is the hyperfine angular momentum quantum number, m_F is the corresponding angular momentum projection quantum number, and I is the nuclear spin (for further discussion of this choice, see [3]). Details about the qubits in the various species are given in Table 4.1.

4.2. Scattering Probability

We assume that gates are performed on m and g qubits using stimulated Raman transitions (Fig. 4.1). These are coherent two-photon processes where population is transferred between $|0\rangle$ and $|1\rangle$ virtually through higher energy intermediate states $|k\rangle$. During this process, there is a chance of spontaneous

[3]These are not necessarily "optimal" qubits. We choose them simply to have consistent behavior across m qubits for studying the scattering errors.

	$^{9}Be^{+}$	$^{25}Mg^{+}$	$^{43}Ca^{+}$	$^{87}Sr^{+}$	$^{133}Ba^{+}$	$^{135}Ba^{+}$	$^{137}Ba^{+}$	$^{171}Yb^{+}$	$^{173}Yb^{+}$
I	3/2	5/2	7/2	9/2	1/2	3/2	3/2	1/2	5/2
$\tau_{D_{5/2}}$(s)	-	-	1.110	0.357	29.856			0.0072	
$\|0\rangle$ (m)	-	-	$\|6,+5\rangle$	$\|6,-6\rangle$	$\|2,+2\rangle$	$\|4,-3\rangle$	$\|4,-3\rangle$	-	-
$\|1\rangle$ (m)	-	-	$\|5,+5\rangle$	$\|7,-6\rangle$	$\|3,+2\rangle$	$\|3,-3\rangle$	$\|3,-3\rangle$	-	-
$\|0\rangle$ (g)	$\|2,0\rangle$	$\|3,0\rangle$	$\|4,0\rangle$	$\|5,0\rangle$	$\|1,0\rangle$	$\|2,0\rangle$	$\|2,0\rangle$	$\|0,0\rangle$	$\|2,0\rangle$
$\|1\rangle$ (g)	$\|1,0\rangle$	$\|2,0\rangle$	$\|3,0\rangle$	$\|4,0\rangle$	$\|0,0\rangle$	$\|1,0\rangle$	$\|1,0\rangle$	$\|1,0\rangle$	$\|3,0\rangle$
Clock point (m, G)	-	-	2.54	6.49	33.0	1.79	0.0720	-	-
$\omega_0/2\pi$ (m, GHz)	-	-	0.025	0.036	0.062	0.012	0.00047	-	-
$\omega_0/2\pi$ (g, GHz)	1.3	1.8	3.2	5.0	9.9	7.2	8.0	12.6	10.5
$d^2(\omega_0/2\pi)/dB^2$ (m, kHz/G^2)	-	-	55.9	36.7	10.6	119	1.72	-	-
$d^2(\omega_0/2\pi)/dB^2$ (g, kHz/G^2)	3.13	2.19	1.21	0.783	0.395	0.545	0.487	0.309	0.373
$\gamma_{P_{3/2}}/2\pi$ (MHz)	19.4	41.8	23.2	24.0	25.2			25.9	
$\alpha_{S_{1/2}}$	1	1	0.9350	0.9406	0.7417			0.9875	
$\alpha_{D_{3/2}}$	-	-	0.0063	0.0063	0.02803			0.0017	
$\alpha_{D_{5/2}}$	-	-	0.0587	0.0531	0.2303			0.0108	
$\omega_f/2\pi$ (THz)	0.198	2.75	6.68	24.0	57.2			99.8	

TABLE 4.1. Characteristics of the qubits and ion species we consider. Throughout the table, m and g denote values for m or g qubits. I is the nuclear spin; $\tau_{D_{5/2}}$ is the $D_{5/2}$ lifetime; $|0\rangle$ and $|1\rangle$ are the qubit states in the notation $|F, m_F\rangle$; ω_0 is the qubit frequency; $d^2\omega_0/dB^2$ is the second-order B-field-dependence of the qubit frequency; $\gamma_{P_{3/2}}$ is the decay rate of the $P_{3/2}$ manifold; α_M is the branching ratio of $P_{3/2}$ to manifold M; and $\omega_f/2\pi$ is the fine-structure separation of the P manifolds. Lifetimes taken from Sahoo et al., 2006; Taylor et al., 1997; $\gamma_{P_{3/2}}$ values were taken/calculated from Poulsen, Andersen and Skouboe, 1975; Ansbacher, Li and Pinnington, 1989; Gosselin, Pinnington and Ansbacher, 1988; Safronova, 2010; Pinnington, Berends and Lumsden, 1995; Pinnington, Rieger and Kernahan, 1997; α_M values taken from Song et al., 2019; H. Zhang et al., 2016; Z. Zhang et al., 2020; Feldker et al., 2018; ω_f values taken from Ozeri, 2007; other values calculated from atomic parameters.

photon scattering, changing the ion's state or qubit phase and causing an error. The scattering probability is therefore important for characterizing the fidelity achievable by logic gates, as it sets an upper bound.

The rate of 'Λ and V scattering' (the processes with upward pointing laser beam arrows in Fig. 4.2) from qubit states $|i\rangle$ to final state $|f\rangle$ can be calculated from (see Appendix A for derivation)

$$\Gamma_{f,\Lambda\mathrm{V}} = \sum_{i,j,q} \frac{e^2 E_j^2 \mu_{Pi}^2}{4\hbar^2} \xi_i \gamma_{Pf} \left| \sum_k \left(\frac{\langle f| \vec{r} \cdot \hat{\mathbf{e}}_q |k\rangle \langle k| \vec{r} \cdot \hat{\epsilon}_j |i\rangle}{\mu_{Pf}\mu_{Pi}(\omega_{kP} - \Delta)} + \frac{\langle f| \vec{r} \cdot \hat{\epsilon}_j |k\rangle \langle k| \vec{r} \cdot \hat{\mathbf{e}}_q |i\rangle}{\mu_{Pf}\mu_{Pi}(\omega_{ki} + \omega_{kf} + \Delta)} \right) \right|^2 \left(1 + \frac{\Delta}{\omega_{Pf}}\right)^3, \tag{4.1}$$

where ξ_i is the occupation probability of qubit state $|i\rangle$ (on average $\frac{1}{2}$ for each qubit state in the gates we consider), $\vec{r}$ is the position operator of the electron relative to the atomic core (note that the matrix elements of the electric dipole operator can be tricky to calculate; see King, 2008 for a simple introduction to computing them while avoiding pitfalls), γ_{Pf} is the decay rate from $P_{3/2}$ to the manifold containing f, the various ω_{nm} are transition frequencies with n and m corresponding to states or levels (see [4] for more thorough definition of ω_{nm}), Δ is the detuning measured from the $P_{3/2}$ manifold (positive for detuning above this manifold, and neglecting the energy spread of the manifold's sublevels), E_j and $\hat{\epsilon}_j$ are the electric field and polarization direction of beam j respectively, and $\hat{\mathbf{e}}_q$ is the scattered photon polarization. The parameters μ_{Pi} (corresponding to transitions between the $P_{3/2}$ manifold and the manifold containing state i) and μ_{Pf} (corresponding to transitions between the manifolds containing k and f) are the transition dipole matrix elements of the spin-orbital coupling. Their general form can be derived by invoking the Wigner-Eckart theorem Brink and Satchler, 1968, giving

[4] To be explicit: ω_{kP} is $(E_k - E_P)/\hbar$, where E_k is the mean energy of the manifold containing $|k\rangle$ and E_P is the mean energy of the $P_{3/2}$ manifold (note this is zero if k corresponds to $P_{3/2}$); ω_{ki} corresponds to transitions between the manifold containing k and the qubit manifold; ω_{kf} corresponds to transitions between the manifold containing k and the manifold containing f; ω_{Pf} corresponds to transitions between the $P_{3/2}$ manifold and the manifold containing f.

$$\mu_{ul} = \left| \langle L_l | \, |\vec{r}| \, | L_u \rangle \sqrt{(2J_l+1)(2L_l+1)} L_l L_u 1 J_u J_l S \right|, \tag{4.2}$$

where $\langle L_u | \, |\vec{r}| \, | L_l \rangle$ is the reduced dipole matrix element for transitions between upper level u and lower level l, S is the spin, L is the orbital angular momentum, J is the total angular momentum $(L + S)$, and the bracketed term is the Wigner 6j-symbol. The matrix element μ_{ul} can also be related to the decay rate γ_{ul} from the J_u, L_u level to the J_l, L_l level by Steck, 2001

$$\gamma_{ul} = \frac{e^2 \omega_{ul}^3}{3\pi\epsilon_0 \hbar c^3} \mu_{ul}^2, \tag{4.3}$$

where ω_{ul} is the transition frequency, and e is the charge of the electron. In m qubits (but not g qubits), 'ladder scattering' (the processes with downward pointing laser beam arrows in Fig. 4.2) can also contribute to the error. The ladder scattering rate is given by

$$\Gamma_{f,\mathrm{lad}} = \frac{e^2 E_j^2 \mu_{Pi}^2}{4\hbar^2} \sum_{i,j,q} \xi_i \gamma_{Pf} \left| \sum_k \left(\frac{\langle f | \, \vec{r} \cdot \hat{\mathbf{e}}_q \, | k \rangle \langle k | \, \vec{r} \cdot \hat{\epsilon}_j^* \, | i \rangle}{\mu_{Pf} \mu_{Pi} \left(\omega_{kP} + \Delta + 2\omega_{PD} \right)} \right. \right.$$
$$\left. \left. + \frac{\langle f | \, \vec{r} \cdot \hat{\epsilon}_j^* \, | k \rangle \langle k | \, \vec{r} \cdot \hat{\mathbf{e}}_q \, | i \rangle}{\mu_{Pf} \mu_{Pi} \left(\omega_{kP} - \Delta + \omega_{Df} \right)} \right) \right|^2 \left(1 - \frac{2\omega_{PD} + \Delta}{\omega_{Pf}} \right)^3. \tag{4.4}$$

Note that in Eqn. 4.1, the Λ scattering term (first term in the sum within the modulus) dominates over V scattering; similarly, in Eqn. 4.4, the first term in the modulus dominates. In both equations, these terms correspond to a two-photon scattering process where the laser photon is first absorbed or emitted, while the other weaker terms (what we call the counter-rotating contributions to the

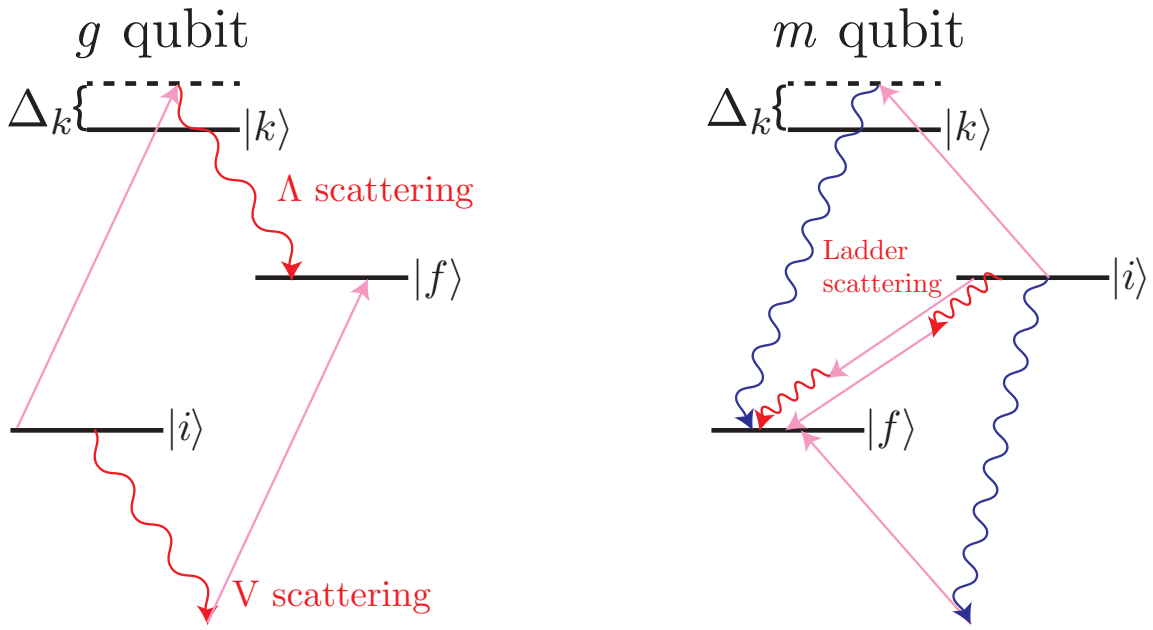

FIGURE 4.2. All two-photon scattering pathways from state $|i\rangle$ to $|f\rangle$ via excited state $|k\rangle$ in g qubits and m qubits. Raman laser beam shown in pink, scattered light shown in red and blue. Processes in which the Raman beam points up in the diagram are Λ or V scattering events. Processes in which the Raman beam points down are ladder scattering events (note that ladder scattering events are allowed only in m qubits). Figure from Moore, Campbell et al., 2023.

scattering rate) correspond to processes where the scattered photon is emitted first (Fig. 4.2).

We can rewrite Eqns. 4.1 and 4.4 in terms of g_{ul} given in Ozeri, 2007 as

$$g_{ul} = \frac{eE\mu_{ul}}{2\hbar}. \tag{4.5}$$

Note that in the following calculations, for m qubits, g_{Pi} and μ_{Pi} will correspond to transitions between the $D_{5/2}$ and $P_{3/2}$ manifolds, *i.e.*, u and l in Eqns. 5.2 and 4.5 will correspond to $P_{3/2}$ and $D_{5/2}$, respectively. For g qubits, g_{Pi} and μ_{Pi} will correspond to transitions between $S_{1/2}$ and $P_{3/2}$. Assuming that g_{Pi} is the same for both Raman beams, we can now write Eqns. 4.1 and 4.4 as

$$\Gamma_{f,\Lambda\mathrm{V}} = g_{Pi}^2 \sum_{i,j,q} \xi_i \gamma_{Pf} \left| \sum_k \left(\frac{\langle f| \vec{r} \cdot \hat{\mathbf{e}}_q |k\rangle \langle k| \vec{r} \cdot \hat{\epsilon}_j |i\rangle}{\mu_{Pf}\mu_{Pi}(\omega_{kP} - \Delta)} + \frac{\langle f| \vec{r} \cdot \hat{\epsilon}_j |k\rangle \langle k| \vec{r} \cdot \hat{\mathbf{e}}_q |i\rangle}{\mu_{Pf}\mu_{Pi}(\omega_{ki} + \omega_{kf} + \Delta)} \right)^2 \left(1 + \frac{\Delta}{\omega_{Pf}}\right)^3 \right. \tag{4.6}$$

and

$$\Gamma_{f,\mathrm{lad}} = g_{Pi}^2 \sum_{i,j,q} \xi_i \gamma_{Pf} \left| \sum_k \left(\frac{\langle f| \vec{r} \cdot \hat{\mathbf{e}}_q |k\rangle \langle k| \vec{r} \cdot \hat{\epsilon}_j^* |i\rangle}{\mu_{Pf}\mu_{Pi}(\omega_{kP} + \Delta + 2\omega_{PD})} + \frac{\langle f| \vec{r} \cdot \hat{\epsilon}_j^* |k\rangle \langle k| \vec{r} \cdot \hat{\mathbf{e}}_q |i\rangle}{\mu_{Pf}\mu_{Pi}(\omega_{kP} - \Delta + \omega_{Df})} \right) \right|^2 \left(1 - \frac{2\omega_{PD} + \Delta}{\omega_{Pf}}\right)^3, \tag{4.7}$$

where ω_{Df} is the frequency of the transition between $D_{5/2}$ and the manifold containing the state f. Eqn. 4.6 gives what we will call the "full model" for g qubits, and the sum of Eqns. 4.6 and 4.7 gives the corresponding full model for m qubits. In m qubits, we include contributions to the gate error from some of the closest higher energy intermediate states, but we neglect such contributions in g qubits for reasons given in section 4.2.3 below.

We will also define what we call our "simplified model", in which we neglect the detuning dependence of the scattered photon frequency (*i.e.*, we assume $(1 + \Delta/\omega_{Pf})^3 \approx 1$), neglect the contributions of the higher energy intermediate manifolds, and assume that only the first term in the squared modulus of Eqn. 4.6 appreciably contributes to the scattering rate in both m qubits and g qubits. This model results in a simpler version of Eqn. 4.6 D. J. Wineland, 2003,

$$\Gamma_f \approx g_{Pi}^2 \sum_{i,j,q} \xi_i \gamma_{Pf} \left| \sum_k \frac{\langle f| \vec{r} \cdot \hat{\mathbf{e}}_q |k\rangle \langle k| \vec{r} \cdot \hat{\epsilon}_j |i\rangle}{\mu_{Pf}\mu_{Pi}(\omega_{kP} - \Delta)} \right|^2. \tag{4.8}$$

These assumptions have also been made in studies of g qubits (*e.g.*, Ozeri, 2007) where the 10^{-4} gate error threshold required detunings on the order of 10 THz. However, as we will show, even at these modest detunings, our model can give large corrections to this simplified model. Despite this, the simplified model in m qubits provides an intuitive illustration of the scattering behavior for a large range of detunings, so we therefore elect to present both models of m qubits throughout this paper.

4.2.1. Single-qubit gates

We follow Ozeri, 2007 in their choice of a representative single-qubit gate: a π-rotation around the x-axis of the equivalent Bloch sphere, a $\hat{\sigma}_x$ gate. We will assume the gates are driven by two laser beams that induce two-photon stimulated Raman transitions. In the case of m qubits, we assume both beams are purely π-polarized because we found that they minimize the scattering probability and power requirements. In g qubits, we assume each beam has equal parts σ^+ and σ^- polarization. For this gate, the required time is given by Ozeri, 2007

$$\tau_{1q} = \frac{\pi}{2|\Omega_R|}, \tag{4.9}$$

where the Rabi frequency Ω_R is calculated according to

$$\Omega_R = g_{Pi}^2 \sum_k \left(\frac{\langle 1|\vec{r}\cdot\hat{\epsilon}_r^*|k\rangle\langle k|\vec{r}\cdot\hat{\epsilon}_b|0\rangle}{\mu_{ki}^2(\omega_{kP}-\Delta)} + \frac{\langle 1|\vec{r}\cdot\hat{\epsilon}_r|k\rangle\langle k|\vec{r}\cdot\hat{\epsilon}_b^*|0\rangle}{\mu_{ki}^2(\omega_{ki}+\omega_{Pi}+\Delta)} \right), \tag{4.10}$$

where r and b (for red and blue) label the two Raman beams, $|0\rangle$ and $|1\rangle$ are the two qubit states and k indexes the available intermediate states. Since

Raman scattering (scattering events for which $|i\rangle \neq |f\rangle$) is the dominant source of errors for most species, we will, for the moment, neglect errors caused by Rayleigh scattering (scattering events for which $|i\rangle = |f\rangle$); Section 4.2.4 below gives a discussion of these errors. We can now calculate the general Raman scattering error as

$$P_{\text{Ram}} = \tau_{1q}\Gamma_{\text{Ram}} = \frac{\pi\Gamma_{\text{Ram}}}{2|\Omega_R|}, \tag{4.11}$$

where Γ_{Ram} is given by the sum of the scattering rates to all possible final states $|f\rangle$ for which $|f\rangle \neq |i\rangle$. For g qubits, this will be the sum of Eqn. 4.6 over all relevant final states; for m qubits, it will be the sum of both Eqns. 4.6 and 4.7 over all relevant final states. This scattering error is plotted for g and m qubits in Fig. 4.3.

In the simplified model of m qubits, we neglect intermediate manifolds aside from the lowest energy $P_{3/2}$ manifold, the detuning dependence of the scattered photon frequency, ladder decay, and the counter-rotating field contribution to the scattering rate and Rabi frequency (the second terms in the sum of Eqn. 4.6 and Eqn. 4.10). In this case, the sum over k has the same form for all ion species considered, giving an expression for the m qubit simplified model's Rabi frequency for each ion species the form

$$\Omega_R = -\frac{2}{15}\frac{g_{Pi}^2}{\Delta}. \tag{4.12}$$

and a Raman scattering rate of the form

$$\Gamma_{\text{Ram}} = \rho\frac{4}{15}\frac{g_{Pi}^2\gamma}{\Delta^2} = 2\rho\left|\Omega_R\frac{\gamma}{\Delta}\right|, \tag{4.13}$$

where ρ is the Raman-only fraction of the total scattering rate (the value of ρ can be inferred from the nearly constant ratio in the low-detuning regime of Fig. 4.5) and γ is the decay rate of the $P_{3/2}$ manifold. For the m qubit's simplified model, this results in a gate error of

$$P_{\text{Ram}} = \rho \frac{\pi\gamma}{|\Delta|}. \tag{4.14}$$

This simplified model of m qubit scattering gives an especially simple form for P_{Ram}, since only one manifold ($P_{3/2}$) appreciably contributes to the scattering. The m qubit's simplified model behavior is also shown in Fig. 4.3 as the dashed lines.

From Fig. 4.3, we can see that the m qubits and g qubits each, as groups, have markedly similar behavior because their $P_{3/2}$ decay rates are all within $\sim$5 MHz (Table 4.1) of each other. As expected, the full model results deviate from the initial linear regime as the detuning becomes large. In m qubits, the full model yields a lower scattering probability than the simplified model for red-detuning, and a higher scattering probability for blue-detuning. The deviations from the m simplified model can be observed in the lower plot of Fig. 4.3

4.2.2. Two-qubit gates

Consider now a two-qubit Mølmer-Sørensen gate, driven by three Raman beams Mølmer and Sørensen, 1999; Tan, 2016. We will suppose that the three beams are comprised of one pair of co-propagating beams of power $\mathscr{P}$ and one beam counter-propagating with this pair with intensity $2\mathscr{P}$, since this distribution of power minimizes the scattering error for this beam geometry. For this gate, the duration is

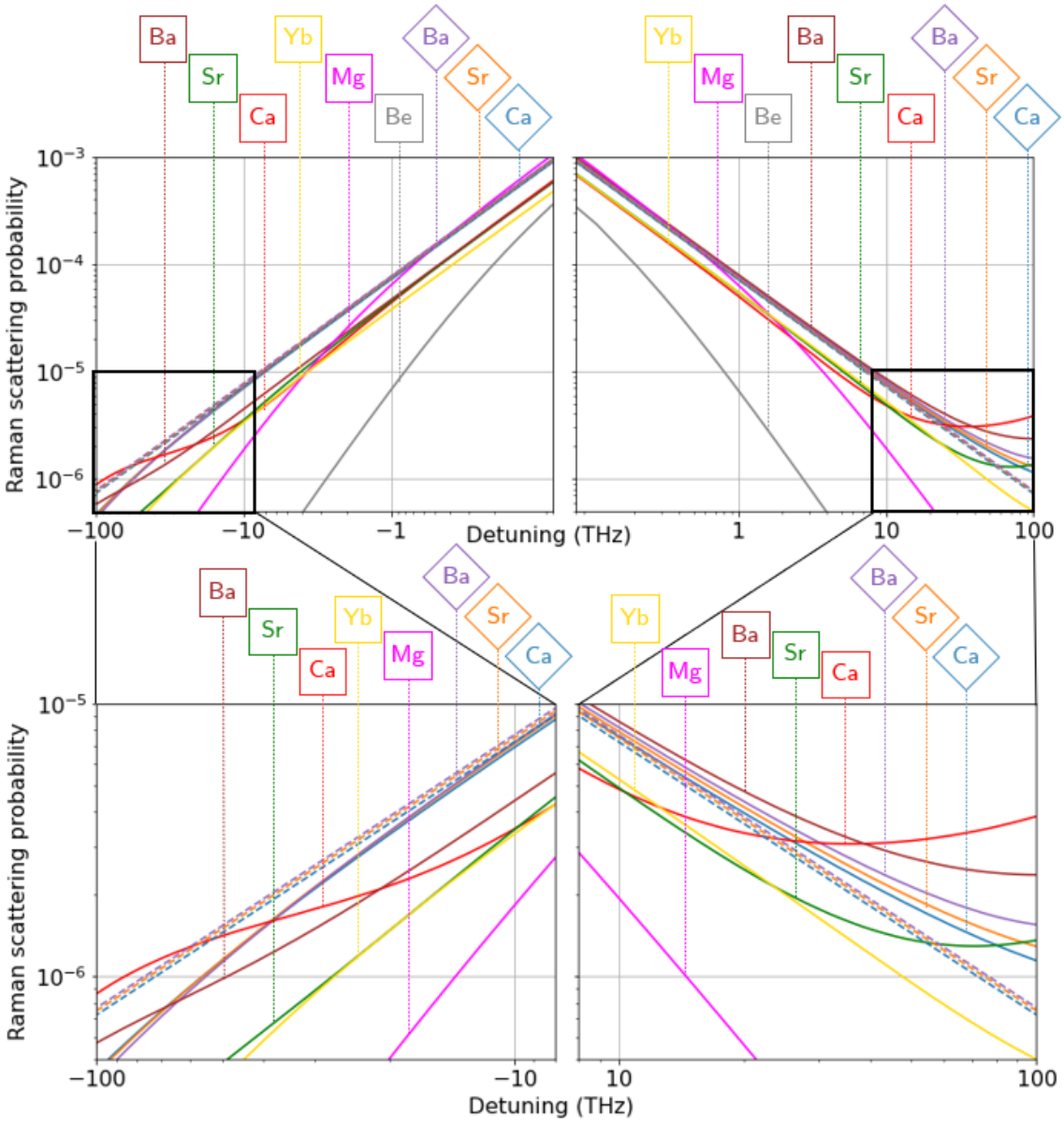

FIGURE 4.3. Raman scattering probability for m qubits and g qubits during single-qubit $\hat{\sigma}_x$ gate for large detuning. The m qubit ions are labeled by diamonds and the g qubit ions are labeled by squares. Detuning is measured relative to $P_{3/2}$ in m qubits; for g qubits, red detuning is measured relative to $P_{1/2}$, and blue detuning is measured relative to $P_{3/2}$. The lower plot shows zoomed-in regions of the upper plot with the simplified model behavior shown for m qubits as dashed lines. Figure from Moore, Campbell et al., 2023.

$$\tau_{2q} = \frac{\pi}{2\sqrt{2}|\Omega_R|}\frac{\sqrt{K}}{\eta}. \tag{4.15}$$

This is the gate time for the two-qubit gate in Ozeri, 2007 but reduced by a factor of $1/\sqrt{2}$ because of the unequal distribution of intensities in this setup. In this equation, K is the number of loops the $|01\rangle$ and $|10\rangle$ states trace out in phase space (we set $K = 1$ for our calculations) and η is the Lamb-Dicke parameter, which for counter-propagating Raman beams is given Ozeri, 2007 by

$$\eta = \Delta k z_0 b_p^{(i)} = 2k_L z_0 \frac{1}{\sqrt{2}} = \sqrt{2}\frac{\omega_L}{c} z_0, \tag{4.16}$$

where Δk is the magnitude of the difference between the two Raman beams' wavevectors (this difference wavevector being aligned to the mode of interest), k_L and ω_L are respectively the wavenumber and frequency of the Raman beams, and $b_p^{(i)}$ is the mode participation factor (equal to $1/\sqrt{2}$ here). Note that the simplified model of Ozeri, 2007 considers perpendicular beams which would increase the Lamb-Dicke parameter by a factor of $\sqrt{2}$. The root-mean-square spatial spread of the ground state wavefunction z_0 is given by

$$z_0 = \sqrt{\hbar/2M\omega_{\text{trap}}}, \tag{4.17}$$

where M is the mass of each ion and ω_{trap} is the frequency of the driven motional mode.

The scattering probability for this gate is the single-qubit gate scattering probability scaled by a factor of 4, as well as the extra gate time factor Ozeri, 2007. The factor of 4 comes from two considerations: first, that the two-qubit gate uses three beams with a total power twice as great as in the total beam power

used in the single-qubit gate, and second that there are two ions. Both of these differences scales the gate error by a factor of 2 to generate an overall increase of 4. This gives a general form for the two-qubit gate Raman scattering error,

$$P_{R2q} = \frac{\pi\Gamma_{\mathrm{Ram}}}{2\sqrt{2}|\Omega_R|}\frac{4\sqrt{K}}{\eta}. \tag{4.18}$$

For the simplified model in m qubits, this results in

$$P_{R2q,simp} = \rho\frac{\pi\gamma}{|\Delta|}\frac{4\sqrt{K}}{\sqrt{2}\eta}. \tag{4.19}$$

Because η is proportional to the laser frequency, it will in general depend on detuning. For the simplified model, we neglect this detuning dependence, so the error probability again exhibits linear behavior. We do, however, include this dependence in the full model, as the size of the effect is too large to reasonably ignore. In the full model for both g and m qubits, we can see that the Lamb-Dicke parameter leads to a further detuning dependence of the form

$$P_{R2q} \propto \frac{\omega_{Pi}}{|\Delta(\omega_{Pi}+\Delta)|}, \tag{4.20}$$

where ω_{Pi} denotes the frequency of the transition between the $P_{3/2}$ manifold and the manifold containing the qubit states. The Raman scattering error of a 1-loop two-qubit Mølmer-Sørensen gate is plotted in Fig. 4.4; the full models of g and m qubits are shown by the solid curves, and the simplified m qubit model is shown by the dashed curves.

The qualitative behavior of the sharply-increasing red-detuned m qubit scattering probability in Fig. 4.4 can be understood by observing that as the laser frequency approaches zero, the gate time goes to infinity (because the

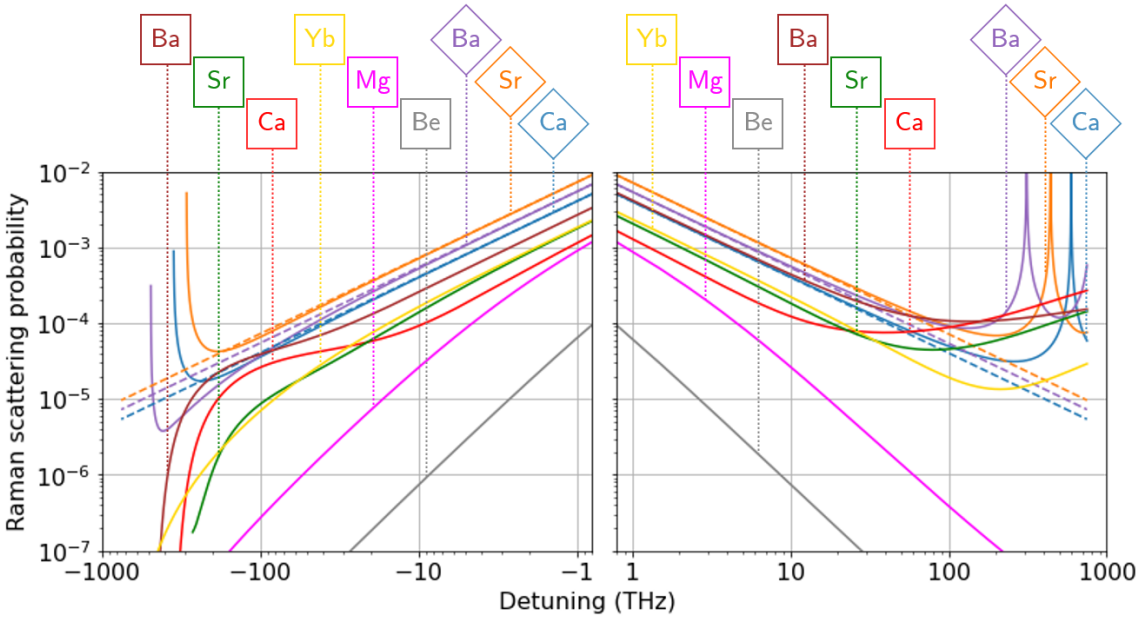

FIGURE 4.4. Raman scattering probability from a 1-loop two-qubit Mølmer-Sørensen gate on m and g qubits. The m qubit ions are labeled by diamonds and the g qubit ions are labeled by squares. The simple model for m qubits is shown in the plot as dashed lines. Detuning is measured relative to $P_{3/2}$ in m qubits; for g qubits, red detuning is measured relative to $P_{1/2}$, and blue detuning is measured relative to $P_{3/2}$. Figure from Moore, Campbell et al., 2023.

Lamb-Dicke parameter is approaching zero); however, the frequency of photons scattered to, *e.g.*, $S_{1/2}$ approaches a non-zero value (the $S_{1/2} \leftrightarrow D_{5/2}$ transition frequency). The gate error, being the product of the scattering rate and gate time, therefore approaches infinity as the laser frequency goes to zero. This does not occur in g qubits, because the scattered photon frequency also goes to zero as the laser frequency approaches zero. Additionally, the scattering rate in g qubits is generally lower than in m qubits across the detuning range considered. However, scattering errors in m qubits are largely due to scattering to $S_{1/2}$, *i.e.*, outside the qubit manifold. Such errors are easier to detect and correct; indeed, one of our collaborators recently applied some of the results presented here in an investigation

of erasure conversion in quantum error correction with metastable states Kang, Campbell and Brown, 2022.

The form of the g scattering probability plotted in Figs. 4.3 and 4.4 differs in several ways from that given in Ozeri, 2007. First, we compute D-manifold scattering rates directly, whereas Ozeri, 2007 calculates them by multiplying the total scattering rate by the branching ratio to the D-manifolds. This overestimates the D-scattering rate, as it neglects interference between the $P_{1/2}$ and $P_{3/2}$ manifolds. Second, we include the V scattering process and the counter-rotating electric field component contribution to the Rabi frequency (*i.e.*, the contribution to Rabi flopping that is neglected in the rotating-wave approximation). Third, we include the detuning dependence of the Lamb-Dicke parameter and scattered photon frequency (while Ozeri, 2007 used a single value of η and ω_{sc} for the entire detuning range). This latter effect makes the scattering rate proportional to ω_{sc}^3, the cube of the scattered photon frequency (Appendix A). Note that if a detuning is chosen such that $\Delta < -\omega_{Pf}$ the contribution to the scattering probability due to scattering to level f becomes precisely zero. This is because the proportionality to ω_{sc}^3 in such a condition renders the f scattering rate negative, which is non-physical. Another way to see that such scattering is not permitted is to note that it violates energy conservation.

Finally, it is notable that by neglecting the above effects, the simplified model of Ozeri, 2007 implied a lower bound on Raman scattering-induced gate error in g qubits (1.06×10^{-4}, 0.50×10^{-4}, 1.46×10^{-4}, and 0.007×10^{-4} for Ca^+, Sr^+, Ba^+, and Yb^+ respectively). This bound appears because the D-manifold scattering error in that model approaches a non-zero value at large red detunings. However, in our model, this lower bound does not exist. The Raman

scattering error approaches zero at large red detunings. This is as it should be, due to considerations of energy conservation.

4.2.3. Higher levels

The above models have incorporated scattering probability contributions from higher levels in m qubits, but not g qubits (a disparity we will justify in this section). Higher levels contribute to the scattering probability in two ways: through increasing the overall scattering rate, and increasing or decreasing the Rabi frequency. Because the Rabi frequency and scattering rate have different scaling in detuning, the inclusion of higher levels can actually result in a net decrease in scattering probability for some parameter regimes.

There are two factors which clearly attenuate the magnitude of contributions from the higher levels to the Raman scattering error: the larger frequency denominators of the scattering rates and the smaller radial overlap with higher levels' wavefunctions. To numerically estimate the contribution of the higher levels, we calculated it for the $P_{3/2}$, $F_{5/2}$, and $F_{7/2}$ manifolds available in the University of Delaware database Barakhshan et al., n.d. in Ca^+, Sr^+, and Ba^+.

The contributions from higher levels differ substantially in m qubits and g qubits. Destructive interference in the Rabi frequency due to higher levels causes m qubit behavior to change noticeably at large red- and blue-detunings. Interference effects are largely absent in g qubits, however, since the contributions of higher $P_{1/2}$ and $P_{3/2}$ essentially cancel. The reason for this cancellation is that Raman scattering flips the electron spin via the spin-orbit coupling $\mathbf{L} \cdot \mathbf{S}$ in the excited state. However, the dipole matrix element for this process is equal in magnitude but opposite in sign for the two fine-structure manifolds $P_{1/2}$ and

$P_{3/2}$ Cline et al., 1994; Ozeri, 2007. Since we are considering tunings far from the resonant excitation of the higher levels, these matrix elements largely cancel out their contributions; deviations from the g qubit model neglecting higher levels do not exceed more than a few percent until about 1 PHz detuning, where the laser frequency reaches a resonance with a higher P manifold.

Including the higher levels in the m qubit model lowers scattering probability at the 10^{-4} error level by a small amount for red detunings. The corrections for blue detuning, however, can be much larger at the 10^{-4} error level; inclusion of the higher levels *increases* the gate error for blue detuning. These corrections are large enough that when higher levels are included, Sr^+ and Ba^+ can no longer get below the 10^{-4} error level for blue detuning.

4.2.4. Rayleigh scattering errors

So far, we have neglected Rayleigh scattering-induced errors. Previous discussions of scattering in the literature (*e.g.* Ozeri, 2007) have characterized the infidelity contribution of Rayleigh scattering-induced dephasing as being proportional to the difference in elastic scattering rates; however, as is shown in Uys et al., 2010, the dephasing rate due to Rayleigh scattering must be computed by including interference between the Rayleigh scattering amplitudes. This can lead to Rayleigh scattering becoming the dominant source of error for certain parameter regimes. However, since we are considering clock qubits in both m qubits and g qubits, the Rayleigh-scattering-induced decoherence will be negligible. Tan, 2016

Rayleigh scattering can however cause errors during two-qubit gates in two other ways: recoil from the momentum kick during Rayleigh scattering and

nonlinearities in the two-qubit gate. Both effects were studied in Ozeri, 2007 and recoil was found to yield a gate error of the form

$$\epsilon_{Ray} = P_{E2q}\frac{\langle|\beta|^2\rangle}{2K}, \tag{4.21}$$

where P_{E2q} is the probability of a elastic Rayleigh scattering event during the two-qubit gate, β the recoil displacement in phase space due to the scattering event, and K is the number of loops traced out in phase space (again, $K = 1$ for our gate). The expected value of $|\beta|^2$ depends on the polarization choice, but we can determine an upper bound on the reduction in fidelity by taking the recoil displacement to equal its maximum value. For our choice of laser beam geometry, the squared magnitude of the recoil displacement is given by Ozeri, 2007

$$|\beta|^2 = \frac{\eta^2}{2}\left(\frac{1}{\sqrt{2}} + \cos\theta\right)^2, \tag{4.22}$$

where η is the Lamb-Dicke parameter and θ is the angle of the recoil direction from the axis along the motional mode to which we are coupling. The maximum value is at $\theta = 0$, so

$$\langle|\beta|^2\rangle \leq \eta^2\left(\frac{3}{4} + \frac{1}{\sqrt{2}}\right) \tag{4.23}$$

implying

$$\epsilon_{Ray} \leq P_{E2q}\eta^2\left(\frac{3}{8} + \frac{1}{2\sqrt{2}}\right). \tag{4.24}$$

The ratio of this upper bound on Rayleigh recoil error to the Raman scattering error during a two-qubit gate is plotted in Fig. 4.5 for m qubits and g qubits. The two lightest species, Be^+ and Mg^+, have the largest Rayleigh scattering errors

precisely because they are so light; their low masses increase their sensitivity to photon recoil. Additionally, they have higher frequency Raman transitions which makes their Lamb-Dicke parameters larger and therefore further increases their sensitivity to Rayleigh scattering events. In the other species, for most of the detuning range, the Rayleigh recoil errors are small. For m qubits, the magnitude of this contribution to the error is 5 or 6 orders of magnitude lower at the 10^{-4} error level compared to Raman scattering contribution in the various species of ions we consider. The g Rayleigh recoil error is roughly 1 to 3 orders of magnitude smaller than the Raman scattering error for most of the detuning range shown (again, except for Be^+ and Mg^+). The m qubits fare better than g qubits with respect to the Rayleigh recoil error in large part because m qubits have lower branching ratios to the qubit manifold, which leads to a lower probability of elastic scattering events. Furthermore, due to their lower frequency transitions, they have lower Lamb-Dicke parameters, which further suppresses the Rayleigh recoil error.

The infidelity contribution of gate nonlinearities due to recoil momentum displacement is even smaller. As noted in Ozeri, 2007, the error due to such nonlinearities is proportional to η^4. This is negligible for most g qubits and even less important in m qubits, due to their smaller Lamb-Dicke parameters. In Be^+ and Mg^+, this error can still be larger than the Raman scattering error, but it is small compared to the Rayleigh recoil error.

4.3. Power Requirements

Now we will calculate the power required to achieve a given gate error rate (recall that we are considering a two beam single-qubit gate and a three-beam two-qubit gate). We first rewrite Eqn. 4.3,

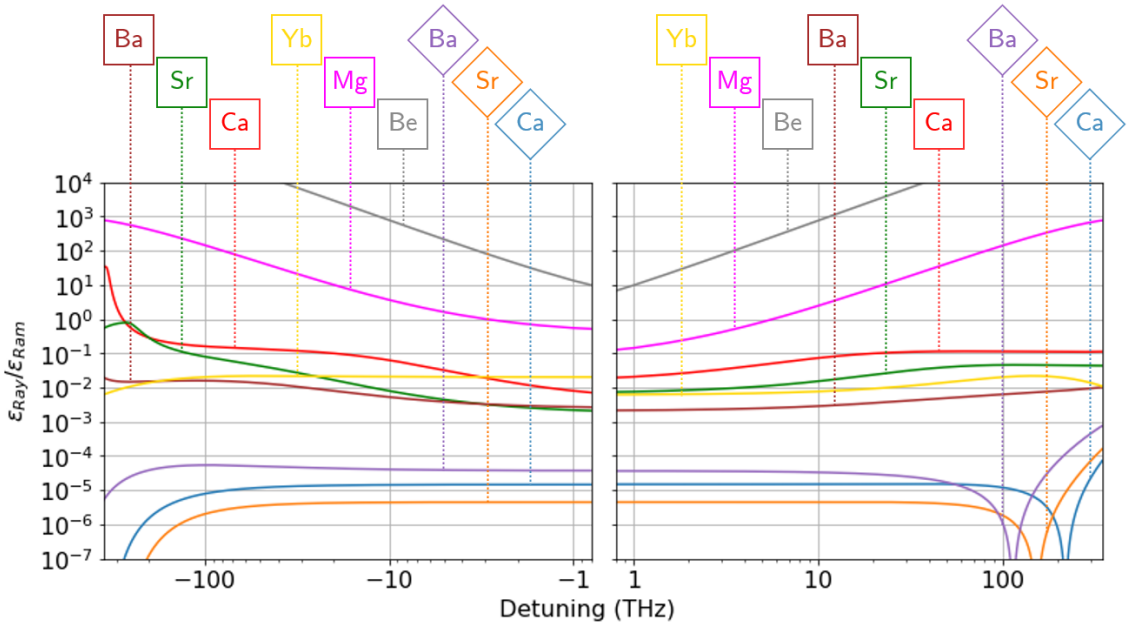

FIGURE 4.5. Ratio of the upper bound on Rayleigh recoil error to Raman scattering error during a two-qubit gate for m qubits and g qubits. The m qubit ions are labeled by diamonds and the g qubit ions are labeled by squares. Note that, for the detunings plotted, the Rayleigh recoil error upper bound exceeds the Raman scattering error only for g qubits in Be^+, Mg^+, and Ca^+. The steep declines in the ratio in m qubits at large blue detunings is due to destructive interference with the $F_{7/2}$ manifolds in the Rayleigh scattering rate. Figure from Moore, Campbell et al., 2023.

$$\rho_q \frac{\gamma}{g_{Pi}^2} = \frac{4\hbar\omega_{3/2}^3}{3\pi\epsilon_0 c^3 E^2}, \tag{4.25}$$

where ρ_q is the inelastic fraction of the scattering from $P_{3/2}$ to the qubit manifold, ω_{Pi} is the frequency of the transition from the qubit manifold to $P_{3/2}$, and E is the peak electric field strength. Note that this equation differs from Eqn. 15 of Ozeri, 2007 only by the factor ρ_q. This is because g_{Pi} in Ozeri, 2007 is defined for $S_{1/2} \leftrightarrow P_{3/2}$ transitions, and the branching ratio from $P_{3/2}$ to the lower D levels was considered small enough that the authors treated the decay rate to $S_{1/2}$ as the total decay rate. In m qubits, g_{Pi} is defined for transitions from $D_{5/2} \leftrightarrow P_{3/2}$,

but ρ_q is too small to treat this decay rate as the total. The decay rate to an individual level must then be the total decay rate weighted by the branching ratio to that level.

By rewriting g_{Pi}^2 in Eqn. 4.25 in terms of Ω_R and its detuning dependence $r(\Delta)$, defined as

$$r(\Delta) = |\Omega_R(\Delta)|/g_{Pi}^2 = \left| \sum_k \left(\frac{\langle 1|\vec{r}\cdot\hat{\epsilon}_r^*|k\rangle\langle k|\vec{r}\cdot\hat{\epsilon}_b|0\rangle}{\mu_{ki}^2(\omega_{kP}-\Delta)} + \frac{\langle 1|\vec{r}\cdot\hat{\epsilon}_r|k\rangle\langle k|\vec{r}\cdot\hat{\epsilon}_b^*|0\rangle}{\mu_{ki}^2(\omega_{ki}+\omega_{Pi}+\Delta)} \right) \right|, \tag{4.26}$$

we can write the power requirement as a function of detuning for single and two-qubit gates as (see Appendix C for derivation)

$$\mathscr{P}_{1q}(\Delta) = \frac{\hbar\omega_{Pi}^3 \mathrm{w}_0^2}{3c^2\rho_q\gamma} \frac{\pi}{\tau_{1q} r(\Delta)} \tag{4.27}$$

and

$$\mathscr{P}_{2q}(\Delta) = \frac{2\hbar\omega_{Pi}^3 \mathrm{w}_0^2}{3\sqrt{2}c^2\rho_q\gamma} \frac{\pi\sqrt{K}}{\tau_{2q}\eta(\Delta) r(\Delta)}, \tag{4.28}$$

where w_0 is the beam waist and $\eta(\Delta)$ is the Lamb-Dicke parameter (including detuning dependence). Because the gate error is also some function of Δ, $\epsilon(\Delta)$ (Sections 4.2.1 and 4.2.2), we can visualize the power and error requirements by plotting the set of points $(\epsilon(\Delta), \mathscr{P}(\Delta))$, shown in Figs. 4.6 and 4.7.

For the simplified model, $r(\Delta)$ can be directly related to the gate error ϵ, allowing us to write the power as a function of error as (Appendix C)

$$\mathscr{P}_{1q}(\epsilon_{1q}) = \rho \frac{5\pi\hbar\omega_{Pi}^3 \mathrm{w}_0^2}{2c^2\epsilon_{1q}} \frac{\pi}{\tau_{1q}} \tag{4.29}$$

and

$$\mathscr{P}_{2q}(\epsilon_{2q}) = \rho \frac{10\pi\hbar\omega_{Pi}^3 \mathrm{w}_0^2}{c^2\epsilon_{2q}} \frac{\pi}{\tau_{2q}} \frac{K}{\eta^2}, \tag{4.30}$$

for single and two-qubit gates, respectively.

As can be seen in Figs. 4.6 and 4.7, the power requirements for g qubits are, for a large range of detunings, about one order of magnitude smaller than the required power for m qubits at the same error probability; this is mostly because of the small branching ratio to $D_{5/2}$ qubit manifold. However, we note that high power lasers are readily available at the large red detunings anticipated for m qubits, so these higher power requirements may not be a limiting factor.

From Fig. 4.7, we can also see the the discrepancies between the simplified model and the full model reappearing. The full model power curves bend backwards past the minima of $\epsilon(\Delta)$, entering a regime of diminishing returns where the gates both take longer and have higher errors. For a fixed gate time, this farther tuning from resonance means more power is required to drive the gate.

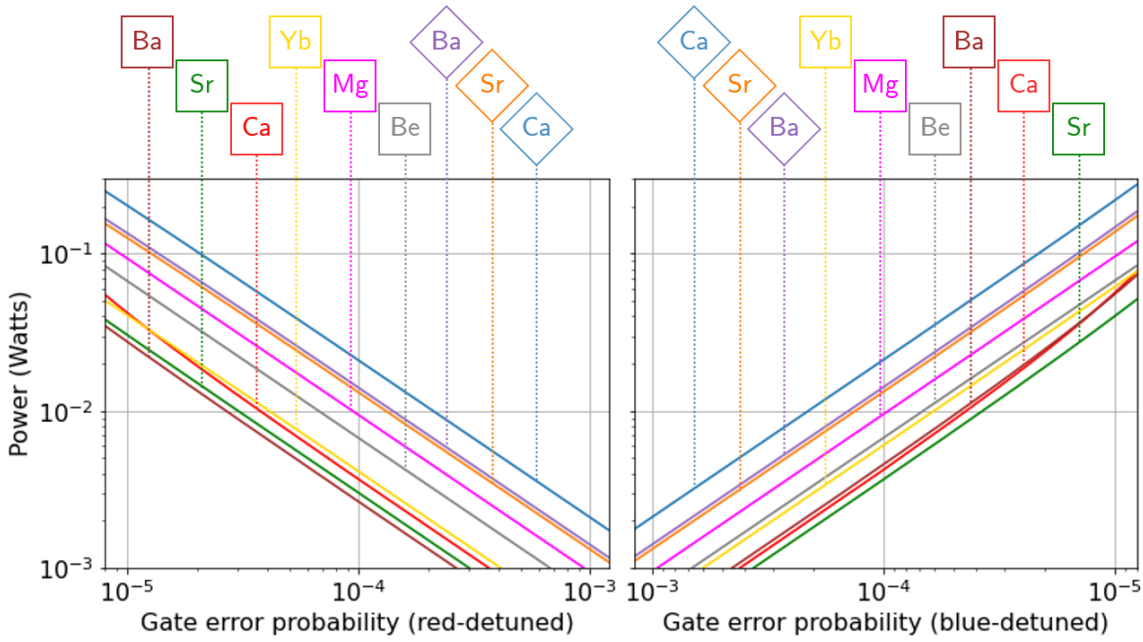

FIGURE 4.6. Total power required to achieve a given error rate during a single-qubit π-rotation gate in the full model (assumes 20 μm beam waist and 1 μs gate time). The m qubit ions are labeled by diamonds and the g qubit ions are labeled by squares. Errors for red-detuned g qubits here are calculated from detunings below $P_{1/2}$ only. Figure from Moore, Campbell et al., 2023.

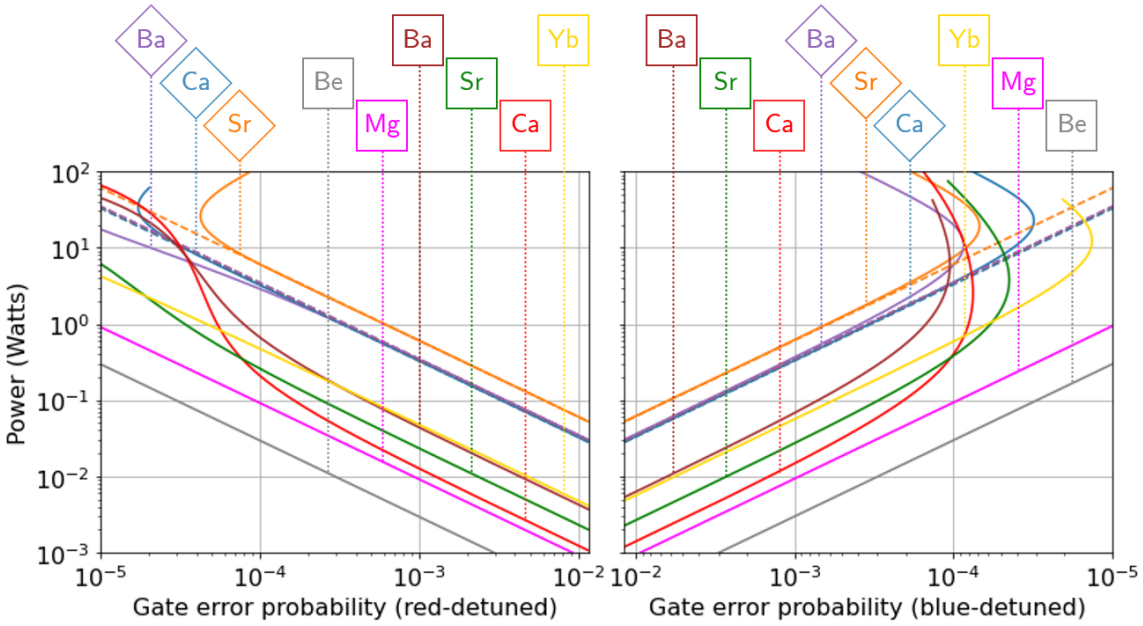

FIGURE 4.7. Total power required to achieve a given error rate during a two-qubit Mølmer-Sørensen gate (assumes 20 μm beam waist, 10 μs gate time, and a 5 MHz axial trap frequency). The m qubit ions are labeled by diamonds and the g qubit ions are labeled by squares. Solid lines correspond to full model, dashed lines correspond to the simplified model. Errors for red-detuned g qubits here are calculated from detunings below $P_{1/2}$ only. Figure from Moore, Campbell et al., 2023.

CHAPTER V

ZEEMAN QUBITS IN $^{40}CA^{+}$

The analysis of Chapter IV centers around hyperfine qubits in trapped alkaline earth ions. However, while our lab ultimately plans to trap $^{43}Ca^{+}$, we have so far trapped only $^{40}Ca^{+}$, which, having no nuclear spin, has no hyperfine structure. We chose to trap $^{40}Ca^{+}$ first because it has a simpler atomic structure (downsides will be discussed in the section below). This chapter will give the details of the Zeeman qubits on which we have performed our experiments and extends the theory of Chapter IV to them.

5.1. Zeeman Qubits in the $D_{5/2}$ Manifold

Since $^{40}Ca^{+}$ has no nuclear spin, its energy manifolds only possess fine structure, i.e., they only have Zeeman sublevels. For our experiments, we choose to encode our qubit as follows: $|1\rangle = |D_{5/2}, m = +5/2\rangle$ and $|0\rangle = |D_{5/2}, m = +3/2\rangle$. One disadvantage of using this Zeeman qubit is that it is not possible to make a "clock" qubit with Zeeman levels. The transition frequency of a clock qubit is at an extremum, such that the derivative of the frequency with respect to magnetic field is zero. This implies that the frequency is relatively insensitive to magnetic field noise and Rayleigh scattering. This is possible with hyperfine qubits, but not in Zeeman qubits, since the qubit frequency is linear in the B-field. However, these qubits are easy for us to prepare and control, and are sufficient for our experiments in this work, and so we elect to use them.

It is easy to prepare the qubit in the $|0\rangle$ state via the optical pumping scheme shown in 5.2. We begin with 397 nm (σ^{+}-polarized) and 866 nm laser beam

pulses. This prepares the $m_J = +1/2$ state in the $S_{1/2}$ manifold. From there, we apply 393 nm (σ^+-polarized) and 866 nm laser beam pulses to pump out the population of $m_J = +1/2$ sublevel of $S_{1/2}$ via the $m_J = +3/2$ sublevel of $P_{3/2}$. Finally, we apply an 854 nm π-polarized laser beam to depopulate the sublevels of $D_{5/2}$, except for the $m_J = +5/2$, the level we are trying to prepare. We then repeat this pulse sequence until the desired fidelity is achieved (usually around 7 times). We are able to obtain about 99% preparation fidelity this way.

With the qubit initialized to $|0\rangle$, we are nearly ready to perform our gate. One problem remains, though: all $\Delta m = \pm 1$ transitions are degenerate since their separation frequencies are set by the Zeeman splitting. We therefore need a way to separate our qubit transition from the other transitions in the $D_{5/2}$ manifold. We achieve this by applying a σ^+-polarized 854 nm beam. This induces a light shift on all sublevels aside from the qubit states (this technique was first used in Curtis, 2010; see also Sherman et al., 2013). Importantly, absent polarization impurities, it also causes no scattering from the qubit states.

After the gate, we perform readout by first shelving the $m = +3/2$ population in the $m = +1/2$ state. We do this so that when we deshelve with the 854 nm π-polarized laser beam we avoid back-scattering to the $m = +5/2$ sublevel. We can then pump this population out of the $D_{5/2}$ manifold, and then turn on the 397 nm and 866 nm lasers to check for population in the $S_{1/2}$ and $D_{3/2}$ manifolds. Finally, after this, we can completely depump the $D_{5/2}$ manifold with the 854 nm σ^-/σ^+-polarized laser beams. This is important for resetting the ion into the $S_{1/2}$ manifold after readout is complete. The complete suite of operations on this qubit is portrayed in Figure 5.2.

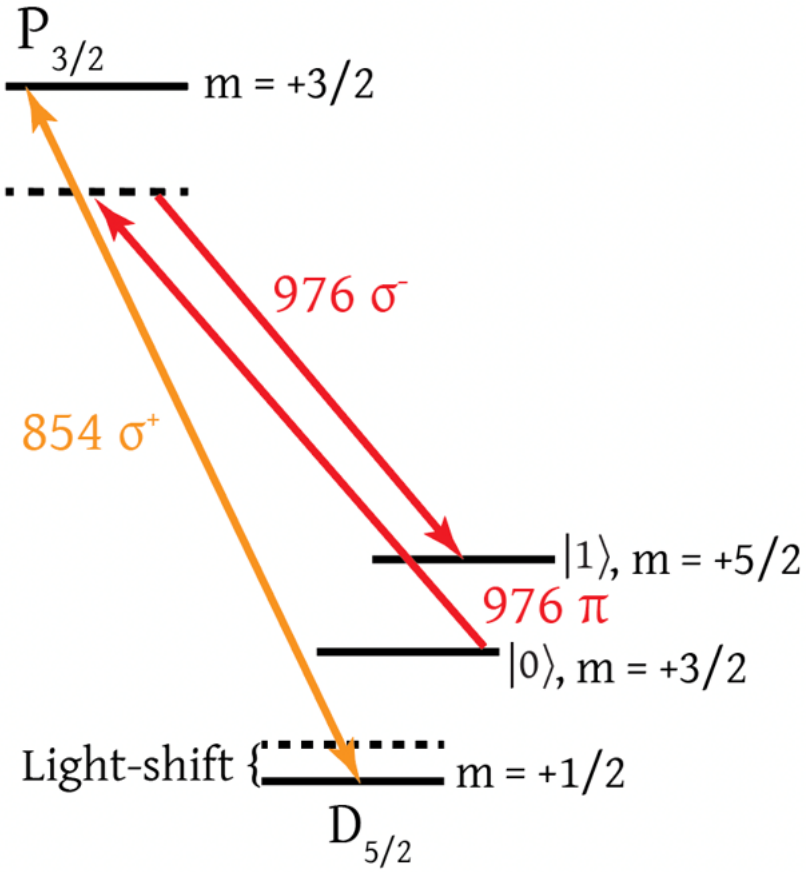

FIGURE 5.1. The $D_{5/2}$ Zeeman qubit. The qubit is isolated with 854 nm light shift beam and the gates are driven with the 976 nm Raman laser beams, or an rf magnetic field.

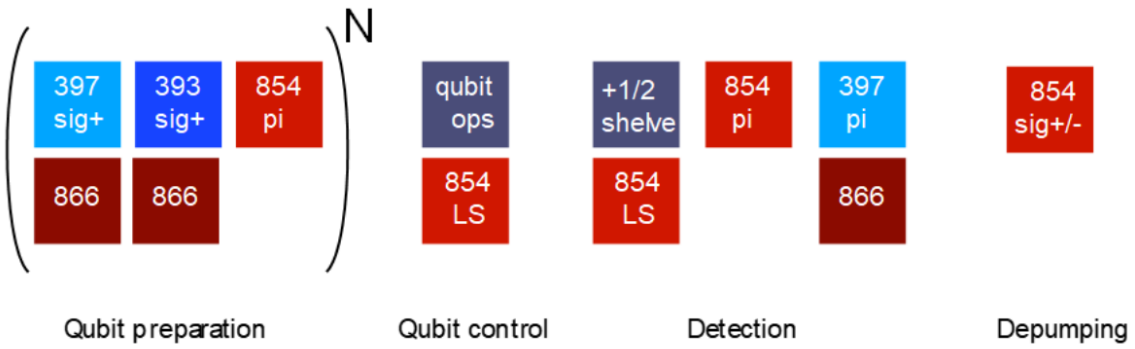

FIGURE 5.2. Laser and rf operations on the $^{40}Ca^{+}$ Zeeman qubit in the $D_{5/2}$ manifold. The preparation pulse sequence is performed N times, until a satisfactory preparation fidelity is achieved. The qubit operations (using the 976 nm Raman beams) may then be performed while the 854 nm light shift beam is on. To read out the qubit, we first shelve the $m = +3/2$ population in the $m = +1/2$ state and then deshelve this population with an 854 nm π-polarized laser beam. We then check for population in the $S_{1/2}$ and $D_{3/2}$ manifolds with the 397 nm and 866 nm laser beams. Finally, we can depump into the $S_{1/2}$ manifold with the 854 nm σ^{-}-polarized laser beam.

5.1.1. Light Shifts

As discussed in Section 5.1, we need to energetically separate our qubit sublevels from the other Zeeman sublevels. We manage this by using an 854 nm σ^+-polarized laser beam. This couples the $m = +1/2$ sublevel of the $D_{5/2}$ manifold to the $m = -1/2$ sublevel of $P_{3/2}$ manifold. This generates a light shift on the $m = +1/2$ sublevel, lifting the degeneracy as desired. The light shift can be calculated from

$$\Delta_{LS} = g^2 \sum_k \frac{|\langle k| \vec{d} \cdot \hat{\epsilon} |D_{5/2}, m = +1/2\rangle|^2}{\Delta}, \tag{5.1}$$

where k indexes all sublevels of the $P_{3/2}$ manifold.

It is worth noting that the 976 nm Raman beams are also capable of generating light shifts. However, the magnitude of the differential light shift from the 976 nm beams scales with the Rabi frequency, so the different transitions would never be well-resolved if this were the sole light shift. Therefore, we generally need the 854 nm light shift beam to make our qubit usable.

While the light shift beam is necessary to isolate the qubit states, it does introduce one other problem. Any σ^- polarization impurity in the 854 nm beam will cause scattering from the qubit states. However, the σ^- polarization impurity is small, typically around 0.1%. The scattering error from σ^- impurities in a 10 mW 854 nm beam during a 10 μs single-qubit gate is shown in Figure 5.3. From the figure, it is clear that keeping impurities low is paramount, since we also want to maintain a large light shift. The relationship between light shift magnitude and beam power can be seen in Figure 5.4

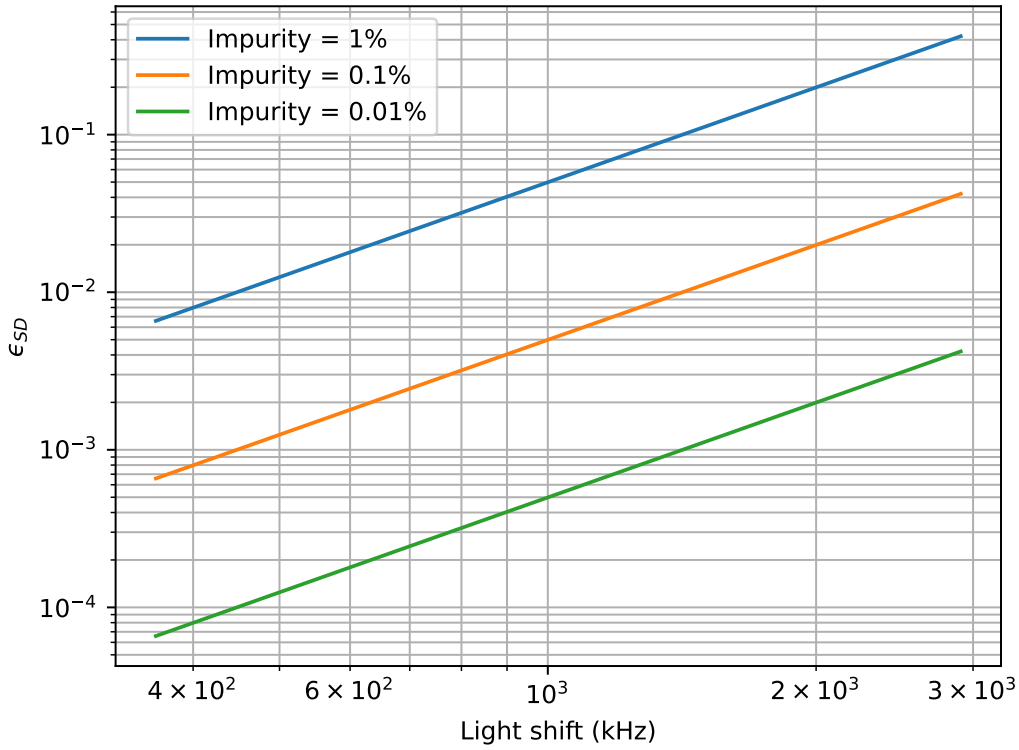

FIGURE 5.3. Trade-off between scattering error ϵ_{SD} from σ^- impurities in a 10 mW 854 nm beam during a 10 μs single-qubit gate and light shift magnitude for various σ^- fractional impurities.

5.2. Scattering Theory for Zeeman Qubits

There is no essential difference in the derivation of the scattering rate for Zeeman qubits as compared to hyperfine qubits. The scattering rate will have the same form as Eqn. 4.6 and Eqn. 4.7, but the matrix elements must be calculated differently. The transition dipole matrix element between upper and lower states $|u\rangle$ and $|l\rangle$ is given by

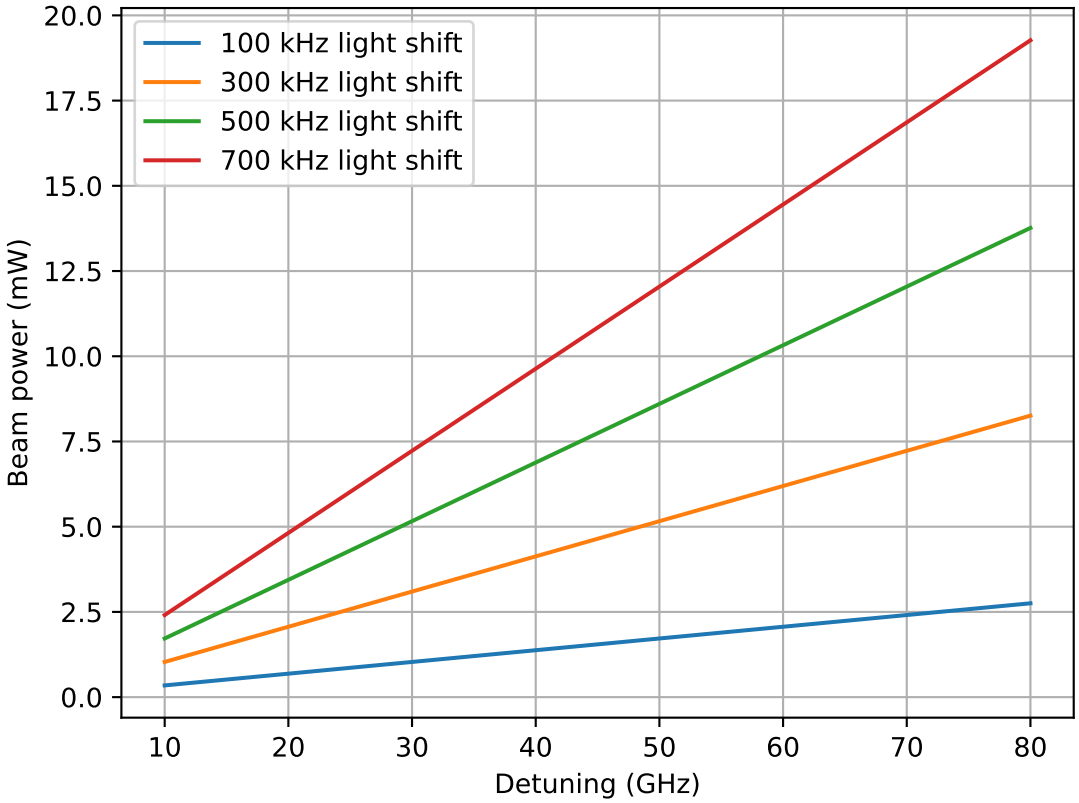

FIGURE 5.4. Power and detuning requirements for various light shifts from the 854 nm σ^+-polarized beam.

$$\begin{aligned}\langle u|\, d_{m_u-m_l}\, |l\rangle =& (-1)^{2J_u+L_l-m_l}\sqrt{(2J_l+1)(2L_l+1)} \\ & \times J_u 1 J_l m_u m_l - m_u - m_l L_l L_u 1 J_u J_l S.\end{aligned} \tag{5.2}$$

Additionally, when working with Zeeman qubits, one convenient feature of hyperfine qubits is unavailable to us: the possibility of producing clock qubits. Because the qubit frequency is determined solely by the Zeeman splitting in Zeeman qubits, it varies linearly with the B-field, which ensures that there will be no local minimum at which to generate a clock qubit. Besides increasing

dephasing, this also means we cannot use the same argument to neglect Rayleigh-scattering-induced decoherence as was given in Section 4.2.4. While this will worsen gate performance, it serves as no obstacle to our goal of measuring the Raman scattering error and comparing it to the predictions of the theory.

5.2.1. Rayleigh-Scattering-Induced Decoherence

The Rayleigh-scattering-induced decoherence can be calculated as in Uys et al., 2010,

$$\Gamma_{el} = g_{Pi}^2 \sum_j \gamma_{Pf} \left| \sum_k \left(\frac{|\langle k| \vec{r} \cdot \hat{\epsilon}_j |0\rangle|^2}{\mu_{Pi}^2 (\omega_{kP} - \Delta)} + \frac{|\langle k| \vec{r} \cdot \hat{\epsilon}_j |0\rangle|^2}{\mu_{Pi}^2 (\omega_{ki} + \omega_{kf} + \Delta)} \right) - \sum_k \left(\frac{|\langle k| \vec{r} \cdot \hat{\epsilon}_j |1\rangle|^2}{\mu_{Pi}^2 (\omega_{kP} - \Delta)} + \frac{|\langle k| \vec{r} \cdot \hat{\epsilon}_j |1\rangle|^2}{\mu_{Pi}^2 (\omega_{ki} + \omega_{kf} + \Delta)} \right) \right|^2 \left(1 + \frac{\Delta}{\omega_{Pf}} \right)^3 . \tag{5.3}$$

As noted in Section 4.2.4, this decoherence is negligible for clock qubits. Since we cannot generate a clock qubit in $^{40}Ca^+$, we cannot neglect the Rayleigh-scattering-induced decoherence. We can quantify the importance of this decoherence by plotting its ratio to the Raman scattering decoherence, as in 5.5.

As the figure shows, red-detuning lowers the fractional Rayleigh scattering error and for our laser system (at -44 THz detuning) will have about 6% more scattering error on top of ϵ_{SD} due to Rayleigh scattering. The error is therefore not substantially larger.

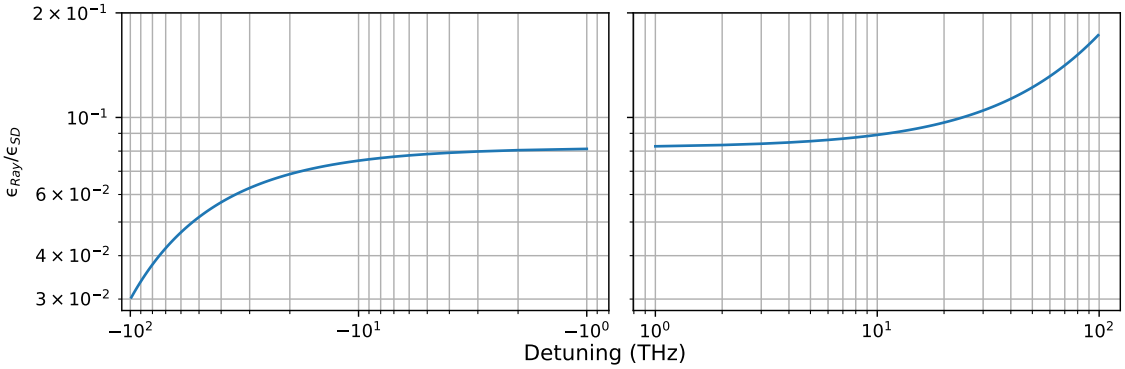

FIGURE 5.5. Ratio of Rayleigh scattering error, ϵ_{Ray}, to Raman scattering errors associated with scattering to $S_{1/2}$ and $D_{3/2}$, ϵ_{SD}.

CHAPTER VI

SCATTERING RATE MEASUREMENTS

With the scattering rate calculations in hand, we now turn to the experimental verification of them.

6.1. 976 nm laser setup

As discussed above, although m qubits require larger detunings to achieve the same gate error as g qubits, the required Raman laser wavelengths for m qubits in $^{40}Ca^{+}$ is in a wavelength range where there are powerful (watts to kilowatts) lasers available. This enables us to complete the gates in the low error regime in a reasonable amount of time.

We chose to use a free-space 700 mW 976 nm hybrid external cavity laser (a HECL; from Innovative Photonics Solutions, model I0976SB0700B) with a CTL300E-1-1200 Koheron driver. This laser is compact, powerful, and inexpensive, being about an order of magnitude more powerful than our Toptica lasers and having two orders of magnitude smaller volume. At 976 nm, this laser is -44 THz detuned from the $D_{5/2} \leftrightarrow S_{1/2}$ transition. We chose to use this wavelength because any wavelength longer than 963 nm (see Table 8.1) allows the two-qubit gate to reach a spontaneous scattering error below 10^{-4}. We choose 976 nm in particular because it is used to pump erbium-doped fiber amplifiers in telecommunications and therefore is widely available. Per Figure 4.4, at the -44 THz detuning this laser achieves, we expect a minimum achievable Raman-scattering-induced gate error of 9×10^{-5}. The laser is protected by a optical isolator (Newport, part number ISO-04-980-MP). The laser can be seen in Figure 6.1.

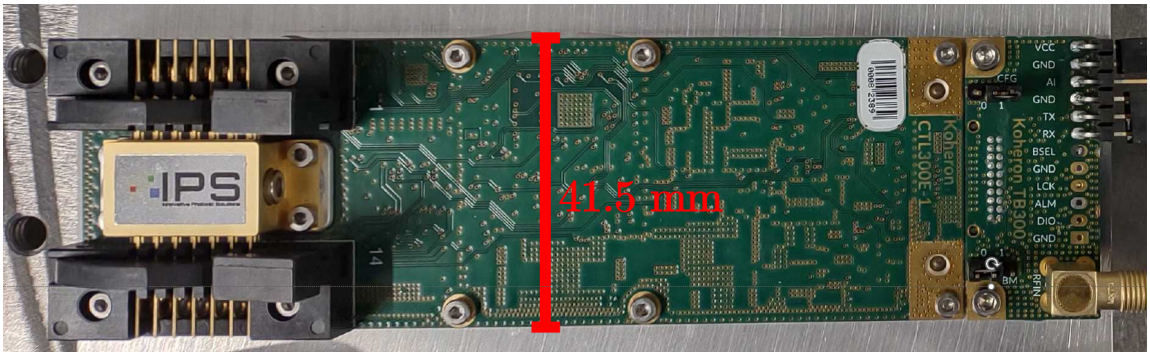

FIGURE 6.1. 976 nm laser.

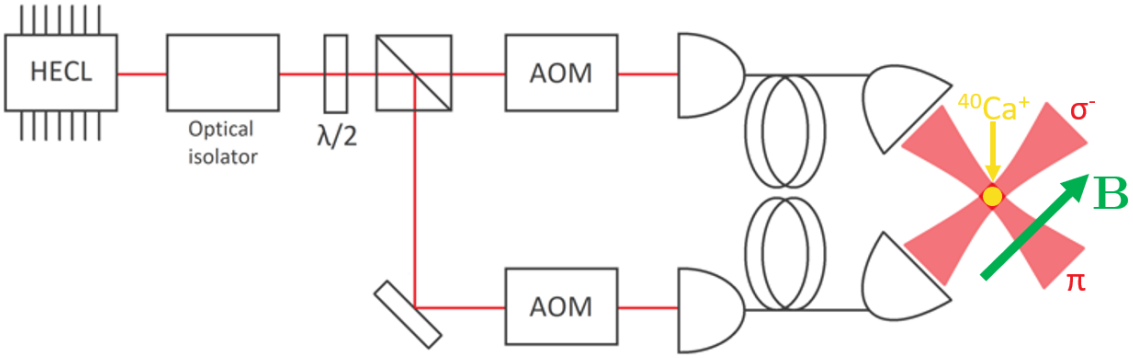

FIGURE 6.2. 976 nm optical setup.

The laser geometry we use for our scattering experiments is shown in Figure 6.2. The laser beam is split and then sent through two AOMs. These are the same AOMs as discussed in Section 3.6. There, it goes into the beam delivery system and is sent to the ions. Note that, in our scattering measurement experiments, we adjust the waveplate to divert all power into one beam at a time and use the undeflected beam out of the AOM in order to maximize available power at the ion. We keep the AOM on so that we can still use the SU servo (see Section 3.7) to control the beam power. Because we are using the zeroth order beam, we have to use a shutter to block the laser beam when we want no 976 nm light on the ion, and this is much slower than turning off the beam with the AOM, since the shutter takes a few milliseconds to block the beam.

6.2. Scattering rate experiments

The analyses of Chapters IV and V allow us to quantify the scattering rates in metastable qubits. In this section, I detail our measurements of scattering rates to the $S_{1/2}$ and $D_{3/2}$ manifolds for m qubits encoded in the $m_J = +5/2$ and $+3/2$ Zeeman sublevels of the $D_{5/2}$ manifold in $^{40}Ca^+$. The big picture of the experiment is that we prepare the qubit in one of its two states, then apply one of the 976 nm Raman beams, either the π- or σ^--polarized beam. We consider σ^- and π-polarized laser beams because they are used to drive Raman gates in our qubit, and so enables us to infer the Raman scattering error we can expect during such a gate. Then, in each relevant combination of initial state and laser beam polarization, we measure the scattering rate (note that we do not consider the $m_J = +5/2$ plus π-polarized beam scenario, since, absent polarization impurities, there will be no scattering in this case).

A more detailed explanation of the experiment is as follows: first, we calibrate the separation frequency between the $m_J = +5/2$ and $m_J = +3/2$ Zeeman sublevels of $D_{5/2}$, with and without the 976 nm beam applied. This enables us to measure the light shift of the qubit separation frequency, from which we infer the laser intensity at the ion. Next, after preparing the ion in either the $m_J = +5/2$ or $m_J = +3/2$ Zeeman sublevel of $D_{5/2}$, we perform a natural lifetime measurement (*i.e.*, we measure the lifetime with the 976 nm laser beam turned off). We do this by preparing the ion in one of the qubit states and wait for some duration. We then read out the state by first checking for fluorescence with the 397 nm and 866 nm cooling lasers. If the ion is bright, we infer that we have scattered or decayed from $D_{5/2}$. Conditional on the ion being dark in the previous step, we apply an rf π pulse on the $m_J = +3/2 \leftrightarrow m_J = +1/2$ transition,

and subsequently apply an 854 nm π-polarized depump beam, and finally check for fluorescence using our 397 nm and 866 nm cooling lasers applied. The rf pulse helps avoid back-scattering to the initial state and the fluorescence tells us if there was any population in the sublevels of $D_{5/2}$ (aside from $m_J = +5/2$). Afterwards, we also apply an 854 nm beam with both σ^+ and σ^- polarization to depump the $m_J = +5/2$ population and again look for fluorescence with our 397 nm and 866 nm cooling lasers; this checks whether or not the ion has heated excessively. If the ion has indeed heated excessively, it will appear dark and we reject the data from this experiment. If instead we detect a bright ion during the 393 nm + 866 nm step, we conclude that the ion was in the $m_J = +5/2$ state. We count up how often this happens and then repeat the experiment for various delays between state preparation and readout. We then fit an exponential curve to this data, giving us a measure of the natural lifetime τ_{Nat} of the $D_{5/2}$ manifold. We then repeat this experiment, but this time with the 976 nm Raman beam on throughout the experiment. The data generated by this experiment is another exponentially decaying lifetime curve, yielding lifetime τ_{Ram}. We can infer the Raman scattering rate Γ_{Ram} from these two measurements via

$$\Gamma_{\mathrm{Ram}} = \frac{1}{\tau_{\mathrm{Ram}}} - \frac{1}{\tau_{Nat}}. \tag{6.1}$$

6.2.1. Systematic Errors in Natural Lifetime Measurements

The method describe above of measuring the scattering rate has a knock-on benefit of checking for certain systematic errors from the measurement, which allows us to make unbiased measurements of the scattering rate. By systematic errors, I refer to any effects which lengthen or shorten the lifetime regardless of

whether the 976 nm laser is on or off. Because of how we calculate the scattering rate, such errors will cancel out of the calculation.

An example of such an effect is cooling laser leakage. Early on in our experiment, we noticed that our natural lifetimes were higher than expected from the literature. After investigation, we discovered that the 393 nm beam was present in the trap when it should have been off. This caused scattering from $S_{1/2}$ to $D_{5/2}$ and lengthened the measured lifetime. However, because the leakage was present when the 976 nm laser beam was on *and* when it was off, this systematic error canceled out when we calculated the Raman scattering error. After removing the 393 nm leakage, we did not notice any further discrepancies between our measured natural lifetime and the literature values, as we show below. However, there are still errors specific to each experimental condition (initial state choice and laser beam polarization) to consider. In the next section, I will give a detailed discussion of these three experimental conditions.

6.2.2. Prepare $m_J = +5/2$ State, Apply 976 nm σ^- Beam

In the first experimental condition, we prepare the $m_J = +5/2$ state and apply a σ^--polarized 976 nm laserer beam. The raw data, showing population over time at various powers, can be seen in Figure 6.4.

To interpret our experimental results correctly, understanding back-scattering to the $D_{5/2}$ manifold is paramount. If we scatter back to the $m_J = +5/2$ state, this does not hinder our goal of measuring the scattering rate to the $S_{1/2}$ and $D_{3/2}$ manifolds (although these Rayleigh scattering events would hurt the qubit during a gate). The scattering rate remains the same as we expect. However, if the ion scatters back to the $m_J = +3/2$ or $m_J = +1/2$ state, the scattering rate will

differ due to the different Clebsch-Gordan couplings of the Zeeman sublevels. The effect will be small though, since the scattering rate is low enough that we expect, most probably, zero or one scattering events in each experiment (where the ion is exposed to the laser for at most one second). The back-scattering contributes to scattering rate measurement error directly if there are two scattering events, one to the $D_{5/2}$ manifold and then one outside of $D_{5/2}$. The back-scattering can also contribute if it scatters back to $m_J = +3/2$ or $+1/2$ and then fails to scatter anywhere else. This is because scattering events where the ion first scatters back to $m_J = +5/2$ and then to $S_{1/2}$ or $D_{3/2}$ do contribute to the scattering rate, but the rate of these events is different for $m_J = +3/2$ or $+1/2$. This effect is, *a priori*, likely to be small though, since the total scattering rate is already low and the ion only scatters to the $D_{5/2}$ manifold 5% of the time, and the scattering rates from each of the other states are not significantly different from the scattering rate from the initial state.

During this experiment, scattering back to the $D_{5/2}$ manifold can change our measured scattering. To estimate the size of this effect, suppose the scattering rate from the initial state to $S_{1/2}$ and $D_{3/2}$, Γ_{SD}, is 1 Hz. By using the probabilities to scatter to each state in Figure 6.3 and assuming that at most one back-scattering event occurs in the experiment (a reasonable assumption given the low branching ratios), we can calculate the expected scattering rate after accounting for back-scattering, and find it to be 0.994 Hz, a 0.6% difference. Because the scattering rate is linear in the beam power, this effect will simply decrease the slope of the linear relationship by 1%. Below, we will verify experimentally that this effect is negligible by showing that a model which considers only scattering from

$m_J = +5/2$ fits the data very well, and the slope of the fit is 0.7% smaller than the theory line, in line with our estimate.

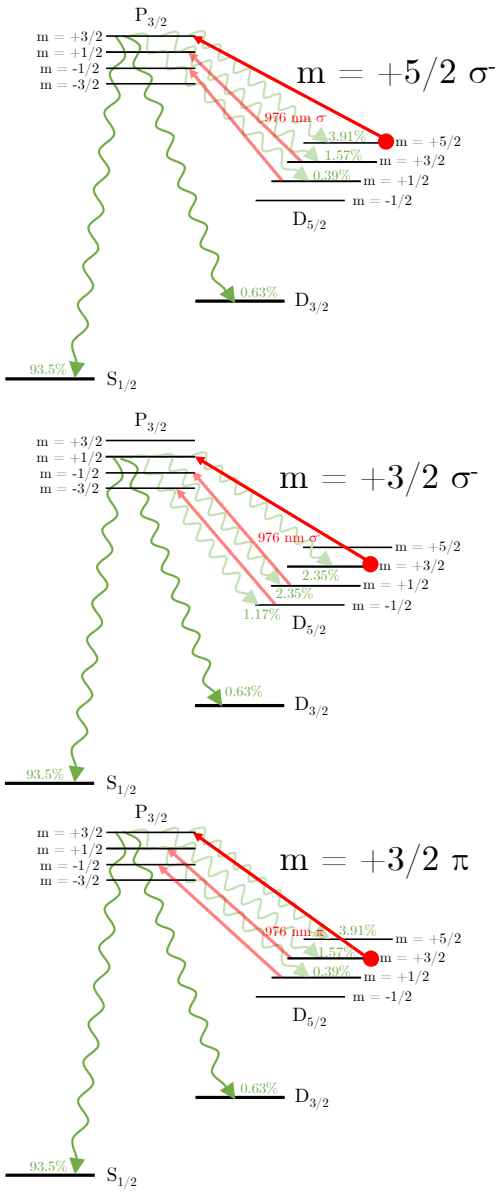

FIGURE 6.3. Scattering diagram for the various initial states and beam polarizations. Possible first-order scattering events indicated by wavy green arrows, with the dark green arrows indicating the scattering events we actually measure (i.e., scattering to $S_{1/2}$ and $D_{3/2}$). Light red arrows indicate coupling of the other sublevels (besides the initial state) of $D_{5/2}$ to $P_{3/2}$.

6.2.3. Prepare $m_J = +3/2$ State, Apply 976 nm σ^- Beam

In the second experimental condition, we prepare the $m_J = +3/2$ state and apply a σ^--polarized 976 nm laserer beam. The raw data, showing population over time at various powers, can be seen in Figure 6.6.

Back-scattering is also possible for this condition, of course. However, for the same reasons outlined above, its effect is negligible. We can undertake the same calculation as in the previous section to confirm this. In this case, we obtain a scattering rate of 0.986 Hz, a 1.4% difference. This is larger that in the $m_J = +5/2$ case, and we will see in the results below that the theory line is indeed 1.4% higher than the data fit line (though still within the error bars).

6.2.4. Prepare $m_J = +3/2$ State, Apply 976 nm π Beam

In the third and final experimental condition, we prepare the $m_J = +3/2$ state and apply a π-polarized 976 nm laserer beam. The raw data, showing population over time at various powers, can be seen in Figure 6.8.

Back-scattering plays a role in this condition as well, but in this case it exerts a strong effect. The reason for this is that the ion can scatter into the $m_J = +5/2$ state, but once the ion is in this state, it is not susceptible to Raman scattering from the π-polarized laser beam (there is no $m_J = +5/2$ level to which it can couple in the $P_{3/2}$ manifold). As you can see in Figure 6.3, the ion will scatter into the $m_J = +5/2$ state in 3.91% of all scattering events. Making the same assumptions as above, the scattering rate will be 3.4% lower after accounting for back-scattering.

Fortunately, this effect is easy to correct for on the experiment side in this case. To do so, we can just count how often the ion is dark after depumping

with the 854 nm π-polarized beam. This serves as a measure of the $m_J = +5/2$ population. Once we have this measure across all the experiments, we can remove the back-scattering effect by dividing the population data by $1 - \rho_{+5/2}$, where $\rho_{+5/2}$ is the measured population of $m_J = +5/2$. Note that this option works well only in this case, since for the other combinations of initial state and laser polarization, there is no state in which the back-scattering population remains in one sublevel throughout the experiment.

6.2.5. Experimental Results and Analysis

For each dataset generated, we took a separate natural lifetime measurement. One advantage of this is it lets us check for any errors that are systematic across the laser-on and laser-off conditions. We measured a natural lifetime in good agreement with the literature value of 1168(9) ms (see Kreuter et al., 2005). Our measured lifetimes were 1165(10) ms, 1154(9) ms, and 1161(13) ms for the $m_J = +5/2$ σ^- beam, $m_J = +3/2$ σ^- beam, and $m_J = +3/2$ π beam datasets, respectively.

The scattering rate is linear in the laser intensity applied, and the slope can be calculated from the Kramers-Heisenberg formula (see Appendix A). Noting this, we can compare the model we developed in Chapters IV and V the experiment by varying the laser intensity and comparing the slopes of these theory lines to the slope of the line fitted to the data. Plots of these lines are given in figures 6.5, 6.7, and 6.9.

The scattering rate measurements are in good agreement with the theory. The fitted slope is within the uncertainty range of the theory line's slope, and vice versa. The uncertainty ranges of the theory line and the fit line are calculated

differently. For the fit line, the uncertainty range spans all lines with slopes within one standard error of the fitted slope. For the theory line, the uncertainty range spans all lines with slopes that fall within the uncertainty range of the model parameters. These parameter uncertainties are dominated by uncertainty in the $P_{3/2}$ lifetime (precision of 0.6%, see Meir et al., 2020), so this uncertainty essentially determines the uncertainty range of the theory line. This corroborates the scattering rate calculations which went into Chapters IV and V, and therefore demonstrates low scattering errors are achievable in trapped-ion qubits. Similar experiments were also performed at UCLA on g qubits in $^{133}Ba^{+}$ ions, again achieving good agreement with the predicted scattering rates (see Boguslawski et al., 2022).

The next step of this research is to actually implement a two-qubit, Raman-beam-induced gate using these 976 nm lasers. Our lab's progress towards implementing such a gate and increasing its fidelity is the subject of the next chapter.

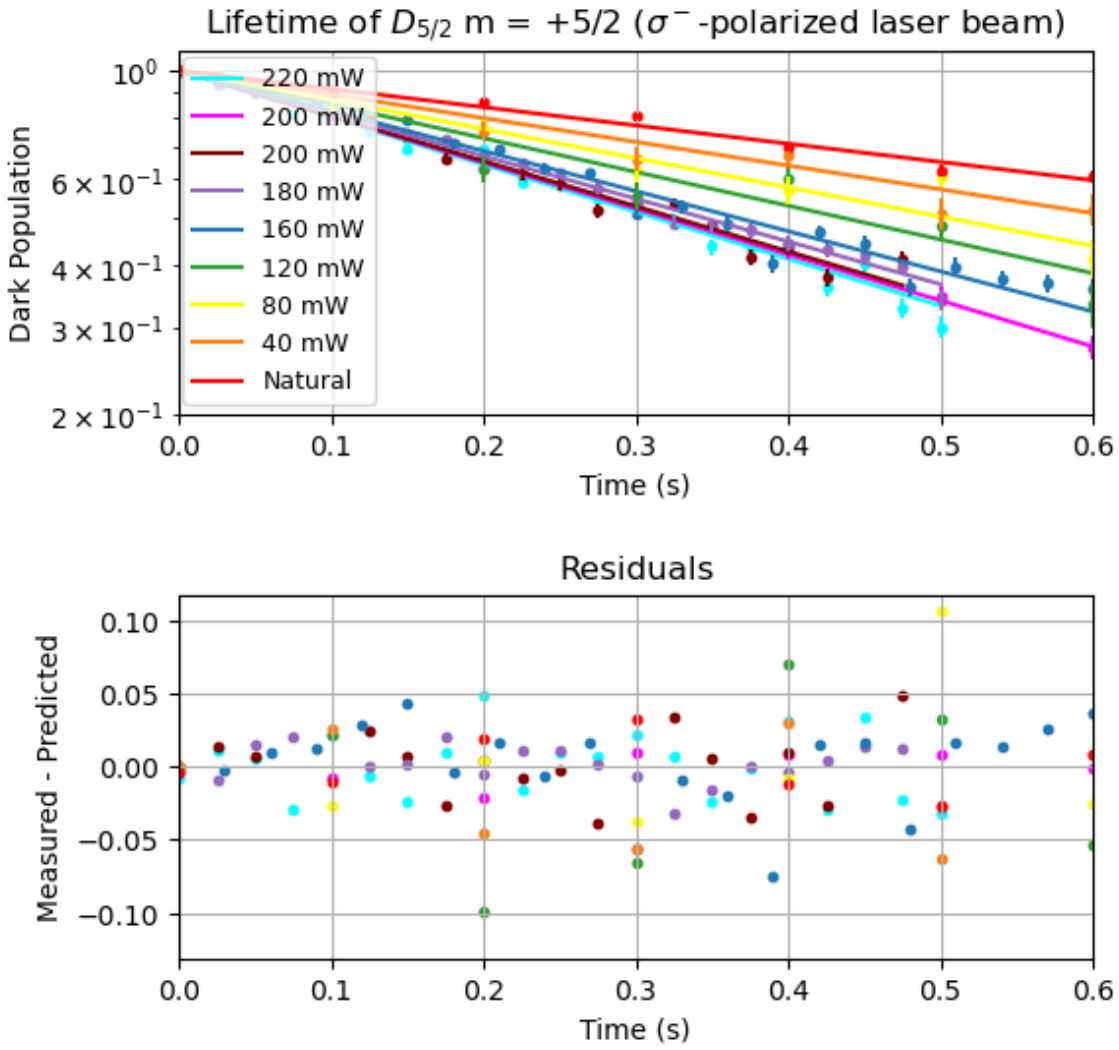

FIGURE 6.4. Lifetime measurement results for $m_J = +5/2$ initial state with σ^--polarized 976 nm laser beam applied. I fit an exponential decay function $1 - e^{\gamma t}$ to the data and infer the scattering rate by taking the difference between the γ fit parameters of the natural lifetime and laser-incident lifetime datasets.

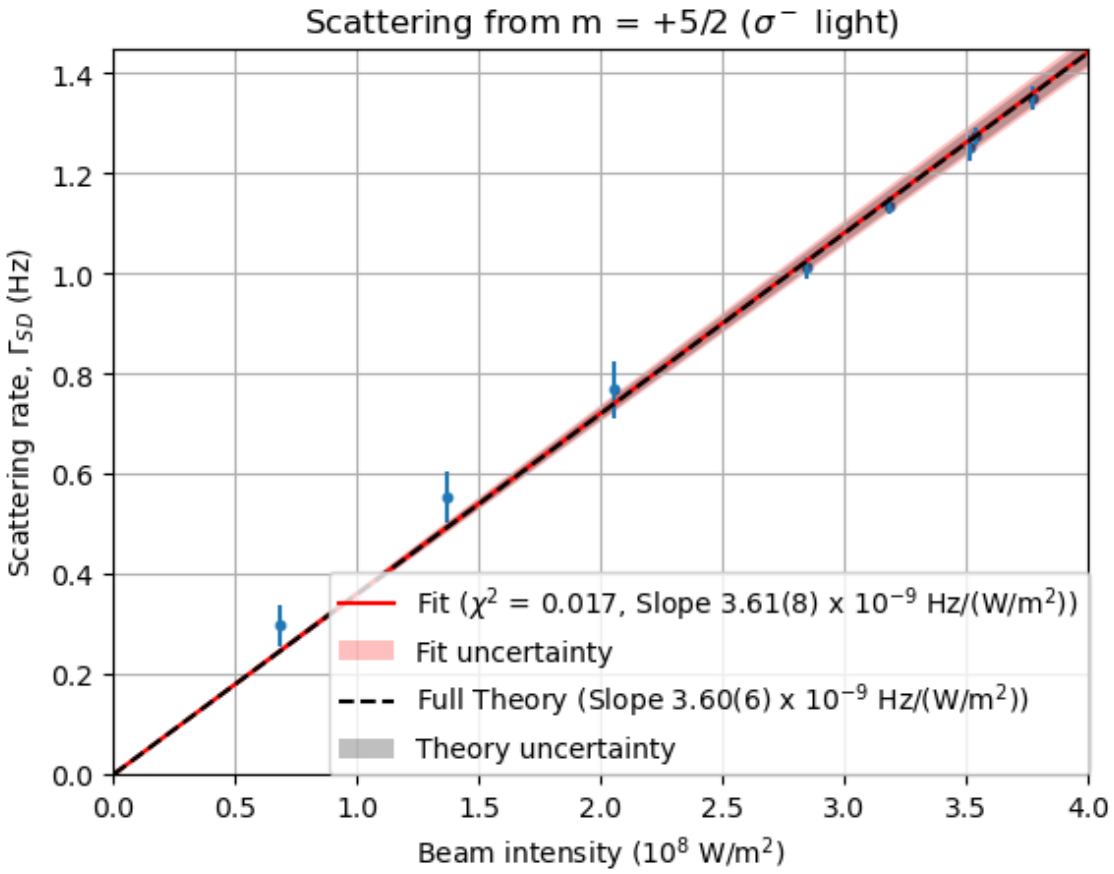

FIGURE 6.5. Scattering rate measurement results for $m_J = +5/2$ initial state with σ^--polarized 976 nm laser beam applied.

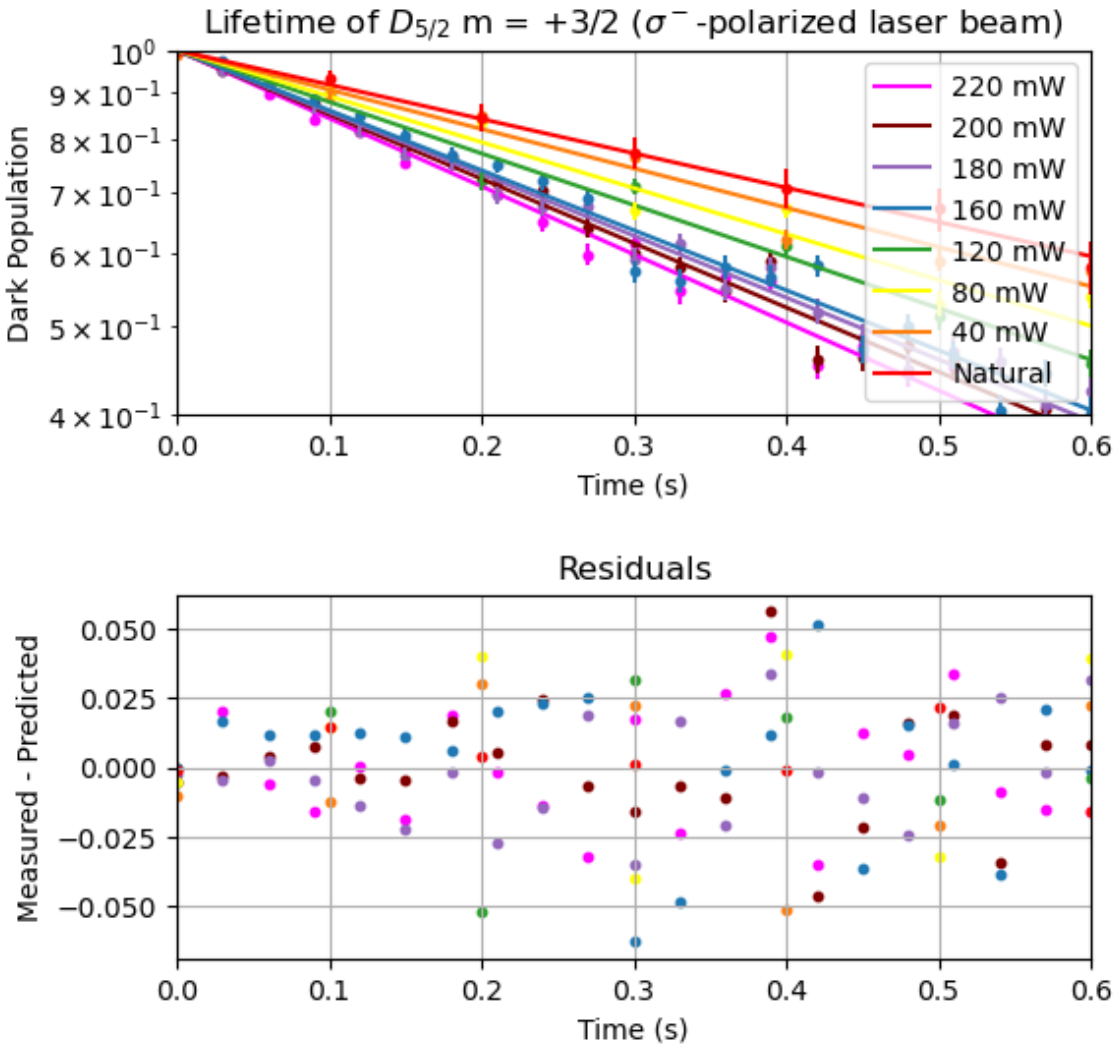

FIGURE 6.6. Lifetime measurement results for $m_J = +3/2$ initial state with σ^--polarized 976 nm laser beam applied. I fit an exponential decay function $1 - e^{\gamma t}$ to the data and infer the scattering rate by taking the difference between the γ fit parameters of the natural lifetime and laser-incident lifetime datasets.

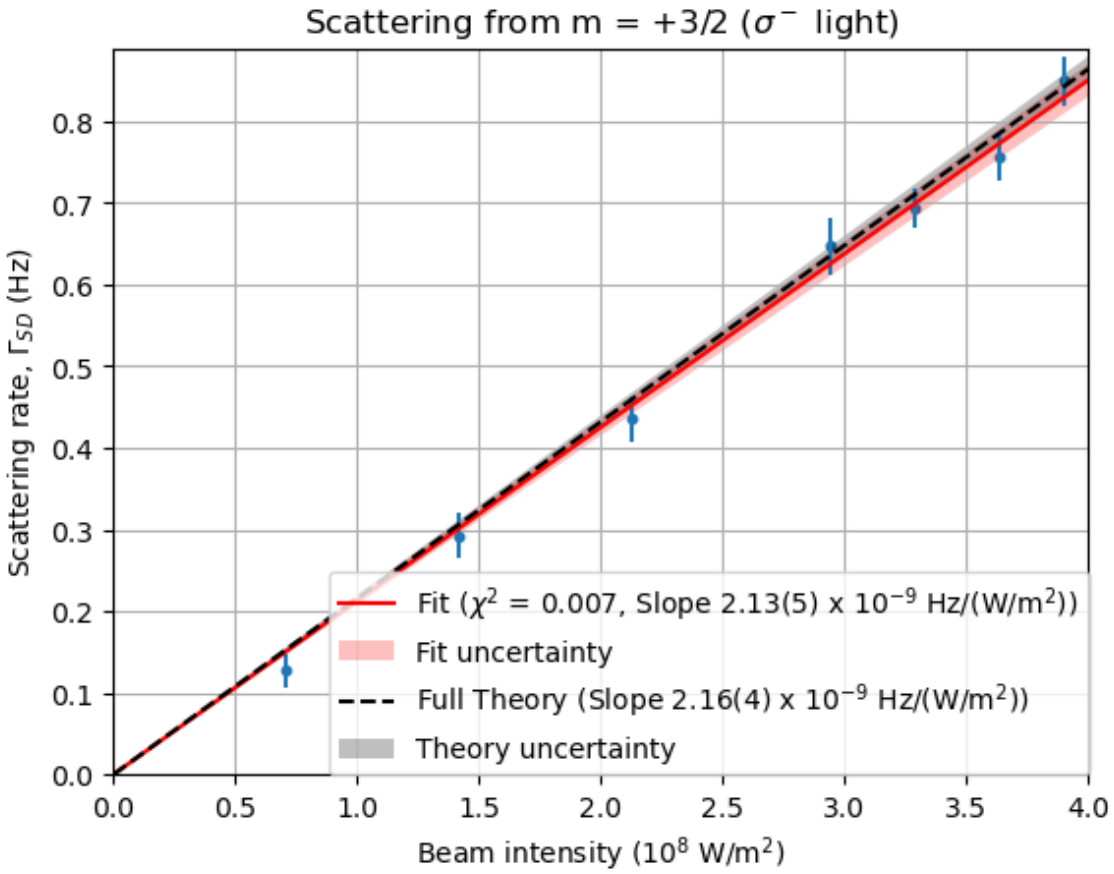

FIGURE 6.7. Scattering rate measurement results for $m_J = +3/2$ initial state with σ^--polarized 976 nm laser beam applied.

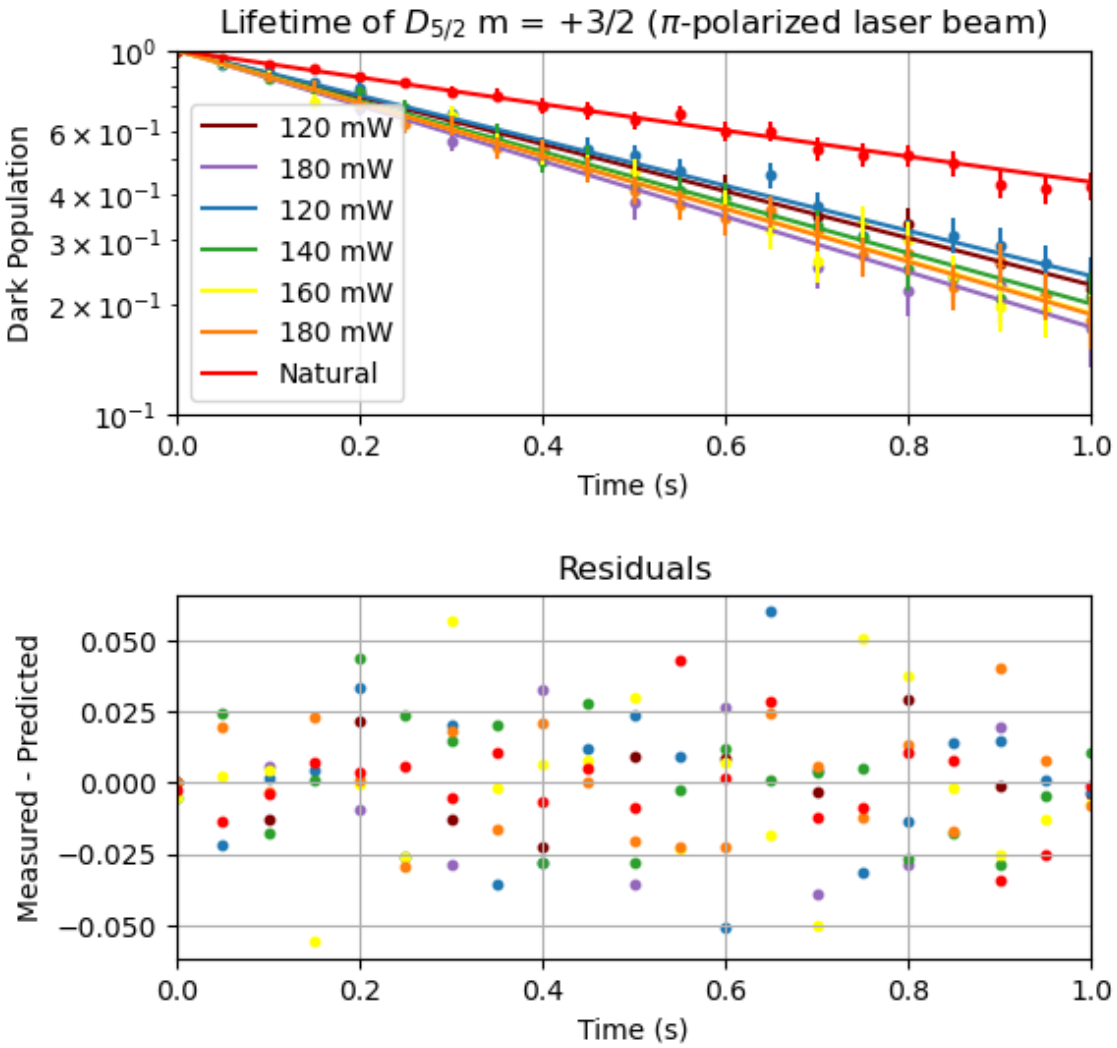

FIGURE 6.8. Lifetime measurement results for $m_J = +3/2$ initial state with π-polarized 976 nm laser beam applied. Note that all population measurements shown here were renormalized by subtracting out the measured $m_J = +5/2$ populations. I fit an exponential decay function $1 - e^{\gamma t}$ to the data and infer the scattering rate by taking the difference between the γ fit parameters of the natural lifetime and laser-incident lifetime datasets.

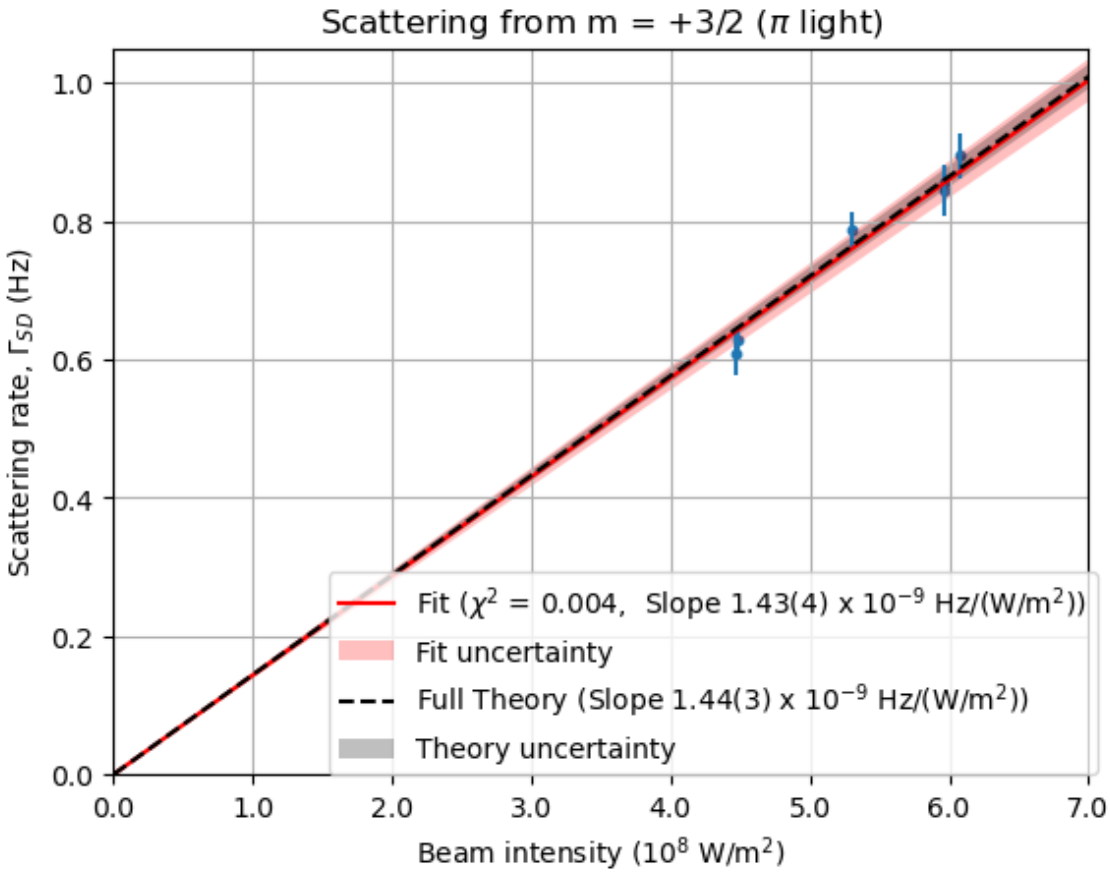

FIGURE 6.9. Scattering rate measurement results for $m_J = +3/2$ initial state with π-polarized 976 nm laser beam applied. The data points here were inferred from raw scattering data with $m_J = +5/2$ population subtracted out.

CHAPTER VII

TWO-QUBIT GATE

As discussed in the introduction, our lab has begun work towards implementing a two-qubit Mølmer-Sørensen entangling gate in our ion trap. As discussed in Chapter II, two-qubit gates have previously been used to generate entanglement in m qubits (see Bazavan et al., 2023 and Roos et al., 2004). However, we are attempting to implement the first Raman-beam-induced entangling gate in m qubits. This will serve as a proof-of-principle for m qubit Raman-driven operations.

7.1. Mølmer-Sørensen Gate Setup

Since we are using the qubit $|\downarrow\rangle \;=\; |D_{5/2}, m_J = +3/2\rangle$, $|\uparrow\rangle \;=\; |D_{5/2}, m_J = +5/2\rangle$, we must drive the MS gate using σ^-- and π-polarized laser beams. The beams and magnetic field geometry in our setup are shown in Figure 7.1.

The Mølmer-Sørensen gate effects entanglement by simultaneously driving the red- and blue-sideband transitions, and so the detunings of the two σ^- beams are appropriately chosen to drive these transitions. The different detunings of the σ^- beams are generated by applying two rf tones to the AOM for that beam.

The difference between the $\vec{k}$ vectors of the π- and σ^- beams, $\Delta\vec{k}$, is at 45° with respect to the mode vector of interest (see Figure 7.1) we are interested in driving. We choose a radial mode because the it is useful for other experiments we perform and it has a higher frequency than the axial modes, which reduces the heating rate but lowers the gate speed. However, this has the downside that

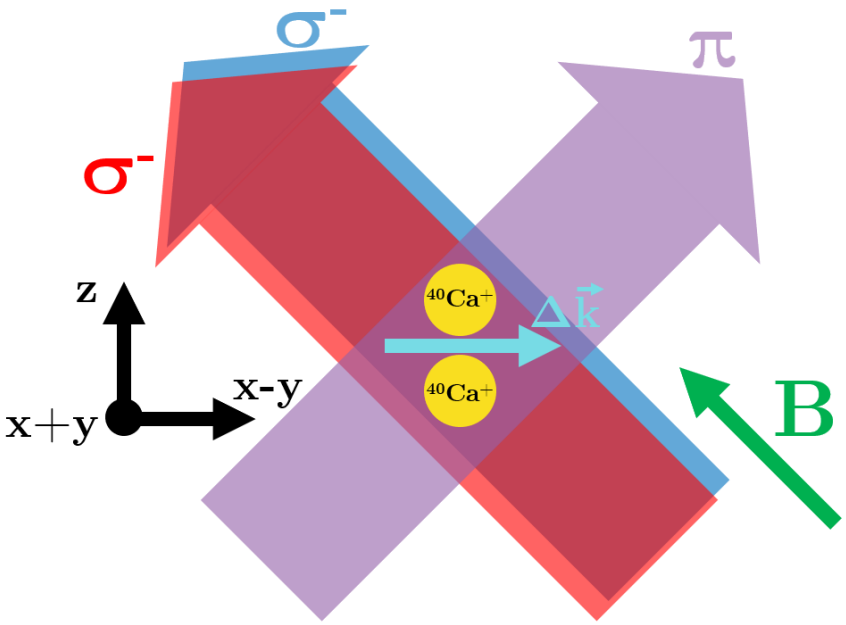

FIGURE 7.1. Schematic geometry of Mølmer-Sørensen gate physical setup. A pair of σ^--polarized laser beams travels perpendicular to a π-polarized laser beam, with all of these beams at 45° from the ion chain axis. The radial modes are along x and y (the difference and sums of these mode vector axes give the axes shown on the figure). The B field runs parallel to the σ^--polarized laser beams. The difference between the π-polarized beam's and each of the σ^--polarized beams' k vectors is shown as $\Delta\vec{k}$.

stabilizing the rf amplitude is more difficult than stabilizing the dc potential (see Section 3.4). Additionally, while, from the perspective of minimizing scattering errors, counter-propagating beams would be superior (they would lower the scattering rate by a factor of $\sqrt{2}$), it comes with several downsides. Because of the geometry of our trap electrodes and the direction of the B field, a counter-propagating beam geometry would require us to split the power in the σ^- beams equally between σ^+ and σ^- polarization, which could waste power. For our MS gate, the power at the ion is 45 mW in the π-polarized beam, with another 45 mW split evenly (22.5 mW each) between the two σ^--polarized beams. This uneven

distribution of power is optimal from the perspective of minimizing scattering errors from a three-beam MS setup Moore, Campbell et al., 2023.

Using the pulse sequence discussed in Chapter V, we are able to achieve a state preparation and readout fidelities of 99.2% and 99.1%, respectively. As for single-qubit operations, we are able to achieve highly-coherent, stimulated-Raman-induced Rabi flops, as seen in Figure 7.2. With a Ramsey experiment, we measure a coherence time of about 1 ms. The decay time in the contrast gives us our coherence time. With spin echoes, we are able to increase the coherence time to 2 ms.

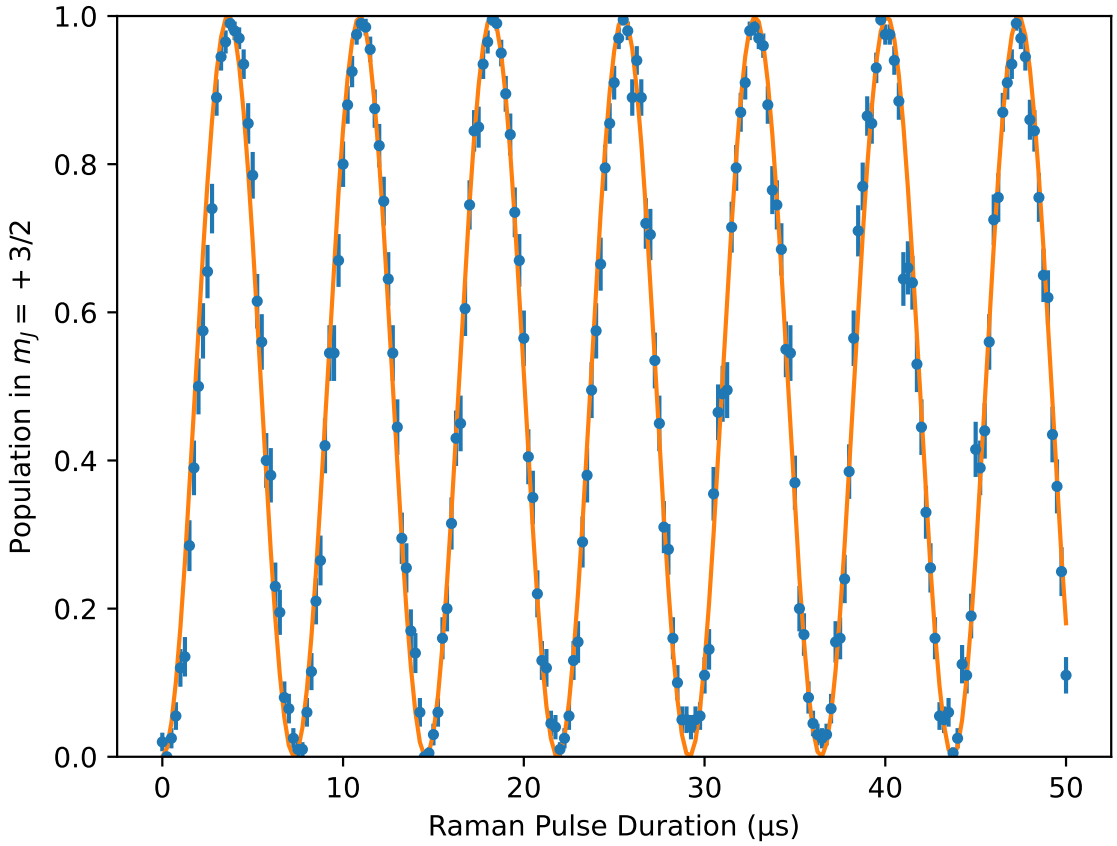

FIGURE 7.2. Carrier transition Rabi flopping at 137(4) kHz Rabi frequency from 976 nm Raman laser beams in the $D_{5/2}$ Zeeman qubit.

We are also able to drive the sideband transitions quite coherently, albeit less so than the carrier (because the system is not completely in the motional ground state). See Figure 7.3. This data is taken after cooling below the Doppler limit, an important step in implementing the MS gate. Although we could just use resolved sideband cooling, we instead follow the Doppler cooling with another sub-Doppler cooling technique, EIT cooling (see Morigi, Eschner and Keitel, 2000 and Lechner et al., 2016). We use this technique simply because it is faster than resolved sideband cooling. After this, we cool further with resolved sideband cooling. With this method, the measured phonon number $\langle n \rangle$ reaches 0.04(1).

There are two beam geometries to choose from when performing an MS gate, the phase sensitive and phase insensitive geometries (see A. Hughes, 2021 and Lee et al., 2005). These are shown schematically in Figure 7.4. We do not have the option to use the phase insensitive geometry, as it requires one of the beams be σ^+-polarized, but this does not couple $m_J = +5/2$ to any state in $P_{3/2}$. We therefore use the phase sensitive geometry instead (the two geometries can be seen in Figure 7.4). This makes our setup more sensitive to laser-phase-fluctuation-induced dephasing, although this can be mitigated to some extent (see Lee et al., 2005 and Section A3 of A. Hughes, 2021).

This setup allows us to generate entanglement because the sidebands couple the ions' internal, electronic states to the collective motional state of the ion crystal. The entanglement generation of this setup can only be appreciated when looking at the joint state of the two ions, as shown in Figure 7.5.

Figure 7.5 shows why each σ^- beam is detuned slightly from the sideband resonance: this ensures that the intermediate states, $|\uparrow\downarrow\rangle$ and $|\downarrow\uparrow\rangle$ are not populated. This setup allows population transfer between the states $|\uparrow\uparrow\rangle$ and $|\downarrow\downarrow\rangle$,

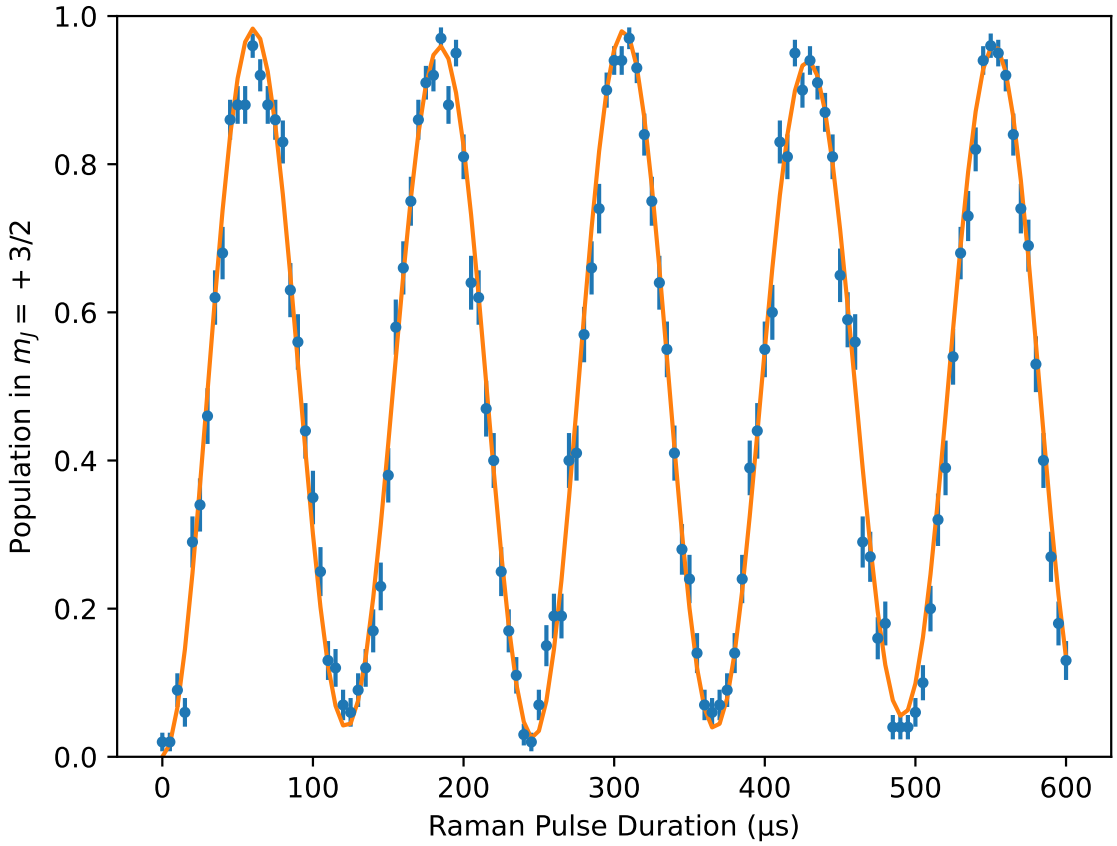

FIGURE 7.3. Sideband transition Rabi flopping at a sideband Rabi frequency of 8.20(2) kHz from 976 nm Raman laser beams in the $D_{5/2}$ Zeeman qubit. The fit to this data indicates that the measured phonon number $\langle n \rangle$ in this run was 0.04(1) and the Lamb-Dicke parameter is 0.060(2).

and so, for an appropriately chosen gate time, we can map the state $|\downarrow\downarrow\rangle$ to the Bell state $\frac{1}{\sqrt{2}}|\uparrow\uparrow\rangle + \frac{1}{\sqrt{2}}|\downarrow\downarrow\rangle$.

We can increase our gate's robustness to detuning errors with Walsh modulation. Walsh modulation involves applying a π phase shift or a π pulse in the middle of the gate. This flips the trajectory of the ion state in phase space Hayes et al., 2011. This behavior is shown in Figure 7.6.

The reason this enhances the robustness of the gate is that while the phase space trajectory may form one incomplete loop on its own, flipping the direction

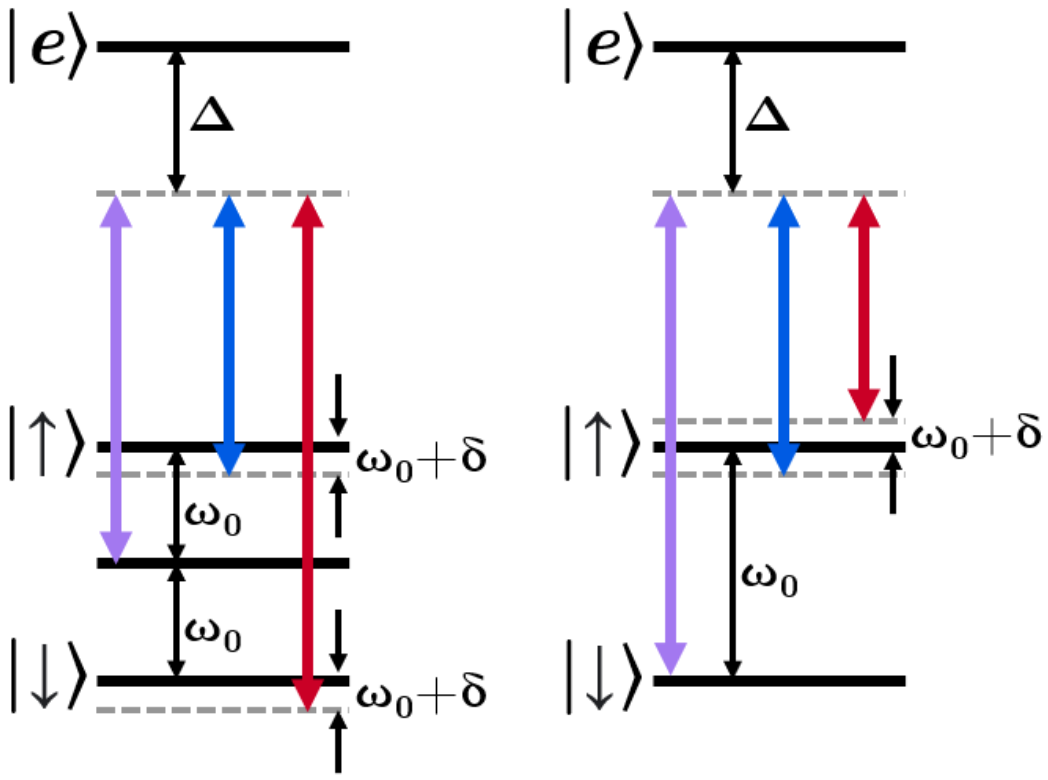

FIGURE 7.4. Phase insensitive (left) and phase sensitive (right) beam geometries in a single ion for MS gate.

of the trajectory with Walsh modulation will create two loops which, together, are more likely to close. We can most clearly see the utility of Walsh modulation by looking at its direct effects on a single ion. To do so, we measure the population in the $|\uparrow\rangle$ state in a single ion with and without this π phase shift (these schemes are called $W(0)$ and $W(1)$, respectively), with results shown in Figure 7.7. We found that the feature associated with loop closure (found at $1/\mathrm{T}_g$ for $W(0)$ and $2/\mathrm{T}_g$ at $W(1)$) is broader for $W(1)$, which shows that,with this setup, we can expect the MS gate's performance to be more robust to detuning errors.

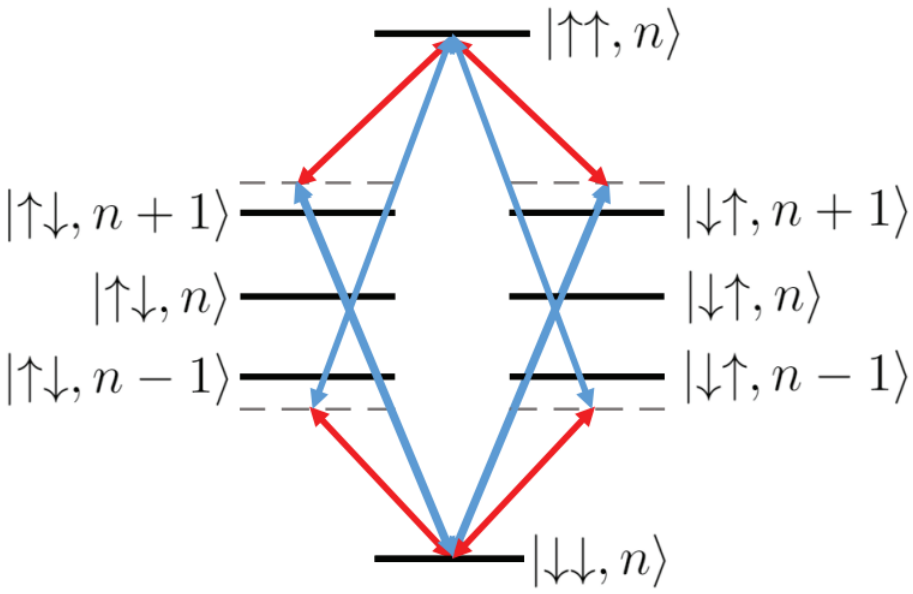

FIGURE 7.5. Schematic of Mølmer-Sørensen gate's effect on the joint state of an ion pair's energy. The detunings are chosen so that the only resonant coupling is between the $|\uparrow\uparrow\rangle$ and $|\downarrow\downarrow\rangle$ states.

7.2. Preliminary Results

Early tests of this gate have yielded promising results. In Figure 7.8, I plot the measured population in each of the possible joint two-ion states as a function of the detuning from the sideband resonance. Our data shows a population of 80% in the the $|\uparrow\uparrow\rangle$ and $|\downarrow\downarrow\rangle$ states. However, for an ideal gate, we would expect that the population would be evenly split between the $|\uparrow\uparrow\rangle$ and $|\downarrow\downarrow\rangle$ states, with no population in the other state. While our results are consistent with a fidelity of 80%, we will need to perform a parity measurement to confirm this Tan, 2016.

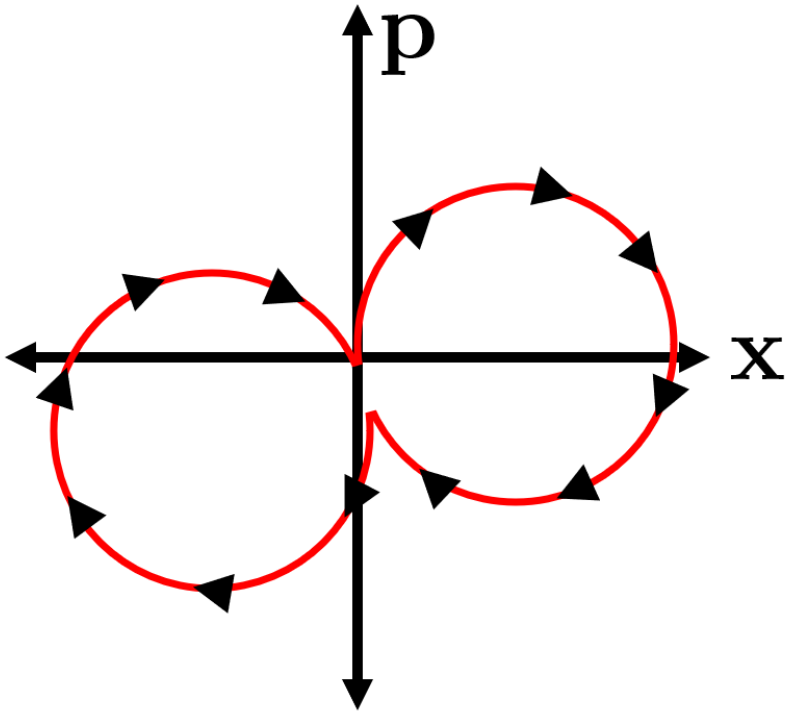

FIGURE 7.6. Effect of Walsh modulation on ion state trajectory in phase space. The first loop would close if not for detuning errors, but the Walsh modulation flips the trajectory, allowing the ion to make a second loop and close the path.

7.3. Future Directions

There are two primary tasks for the future of the investigation into this m qubit MS gate. First, we will need to verify entanglement with a parity measurement. Second, we will need to improve the gate time and fidelity.

To the first point: strictly speaking, population measurements are insufficient to confirm that we are generating entanglement. To ensure we are truly creating entangled states, we will need to implement a parity measurement. This will require that we can control the relative phase of our Raman laser beams, which is not possible in our current setup. However, we will easily remedy this by upgrading our ARTIQ crate (Section 3.7) to version 8, which allows us to control the relative phase of separate rf channels on the DDS boards.

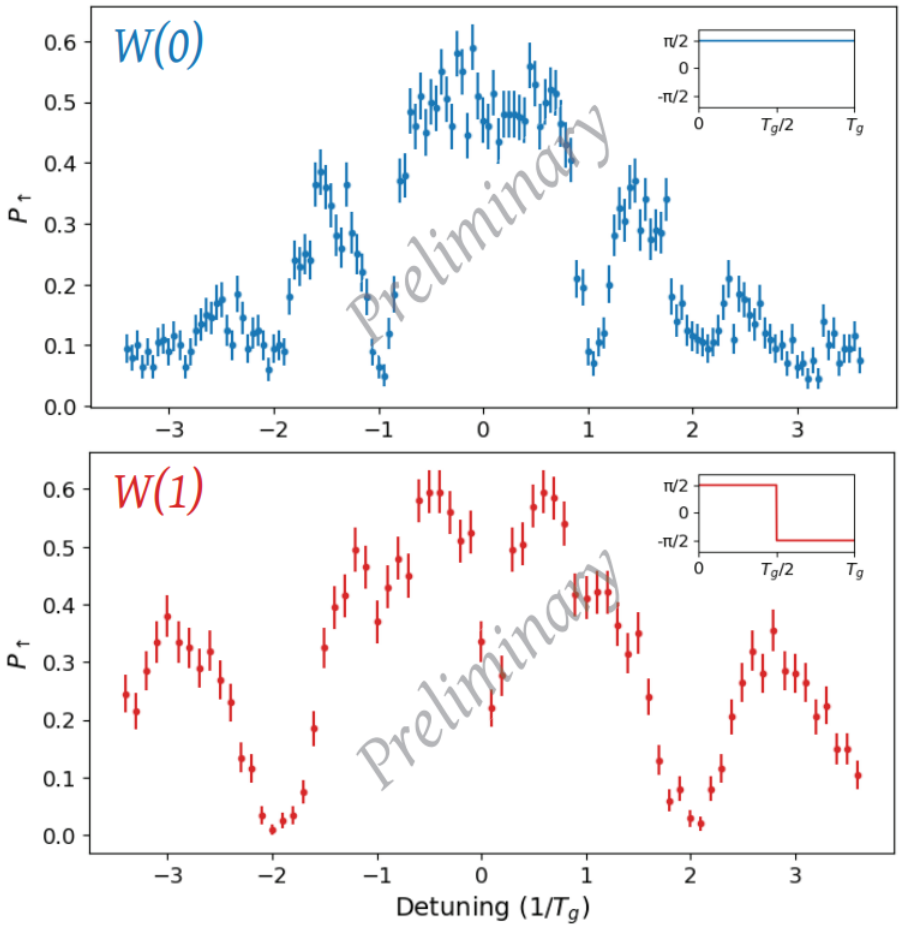

FIGURE 7.7. Preliminary results for the calibration experiment with Walsh modulation. In the $W(0)$ case, shown at the top, the system returns to the ground state at detuning $1/\mathrm{T}_g$, while in the $W(1)$ case, shown at the bottom, it returns at detuning $2/\mathrm{T}_g$ (T_g is 100 ms and 200 ms for the $W(0)$ and $W(1)$ cases, respectively). Note the broader feature associated with loop closure in the $W(1)$ case.

To the second point: in the future, we will explore multiple options for improving the gate time and fidelity. For the gate time, we completed the MS gate in 200 μs, but the preliminary data was taken with an older setup which had 45 mW of power in each polarization. We estimate that, after accounting for losses to the intermediate optics, we could achieve a total power of 300 mW: 150 mW in the π-polarized beam and 75 mW in each σ^--polarized beam, with the

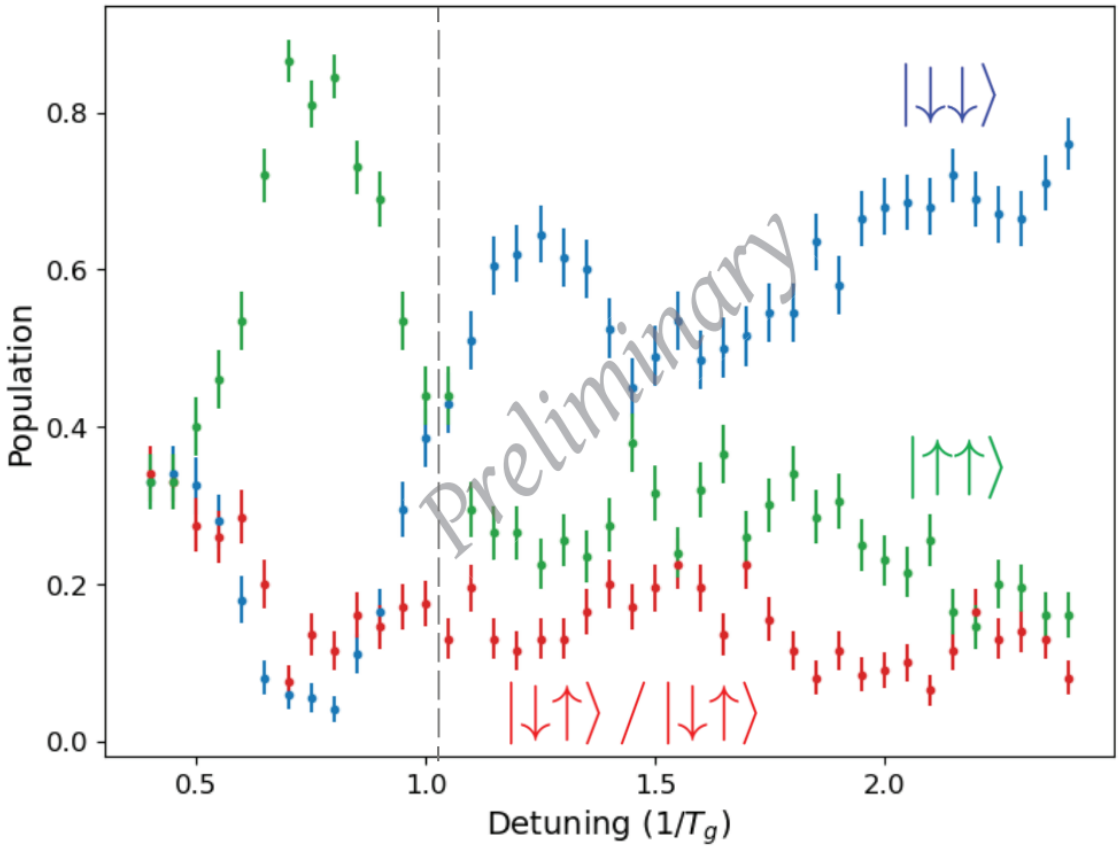

FIGURE 7.8. Preliminary results for the Mølmer-Sørensen gate with possible entanglement generation. Population corresponds to the fraction of experiments when both ions are bright ($|\uparrow\uparrow\rangle$), one ion is bright and the other is dark ($|\uparrow\downarrow\rangle/|\downarrow\uparrow\rangle$), and when both ions are dark ($|\downarrow\downarrow\rangle$). This data was taken without Walsh modulation. There was 45 mW of power in each polarization as discussed above. The 854 nm beam provided a light shift of 697(1) kHz on the $m_J = +1/2$ state during the gate, and a differential light shift on the qubit from the 976 nm Raman beams of 27(1) kHz. The gate time was 200 μs.

current setup. We can further reduce the gate time by increasing the intensity with improved beam focusing. The increased beam power alone will improve the gate time by a factor of three, so we can expect to achieve a gate time of roughly 60 μs with the current setup. Once we have added in Walsh modulation, however, the gate time will be a factor of $\sqrt{2}$ longer than this.

For increasing the gate fidelity, there are many options. First, it is worth noting that the current experimental setup is, in many ways, superior to the setup used to take the data seen in Figure 7.8. Since taking the preliminary MS data, we have improved the qubit and motional coherence. We improved the qubit coherence with feedforward, which suppresses qubit decoherence from 60 Hz electromagnetic signals from wires in the lab. We improved motional coherence and frequency stability with temperature stabilization and implementation of a device which removes amplitude modulation from the rf source 3.4. It is also worth noting that the heating rate is a common limitation of gate performance, but we can mitigate this issue by driving the gate faster or using an out-of-phase mode. Second, the qubit coherence time is only 10 times larger than the gate time, which is a strong limitation. We could improve this with magnetic shielding, but the solution we plan to implement is utilizing clock qubits in $^{43}Ca^{+}$. This would also eliminate the need for the 854 nm light shift laser. Additionally, for $^{43}Ca^{+}$, the fidelity limit from Raman scattering with 976 nm Raman beams is 9×10^{-5}, so the gate will likely be limited by the other factors mentioned above, not the Raman scattering error.

CHAPTER VIII

CONCLUSION

In this thesis, we studied scattering errors in trapped-ion qubits. Our motivation for doing so was the *omg* scheme, an ion trap quantum computing architecture that utilizes multiple different qubit types in the same ion species. Because the *omg* scheme requires the use of m qubits, and photon scattering commonly contributes substantially to the errors, we sought to characterize scattering errors during logic gates in m qubits. In the course of doing so, we found issues with past models of g qubit scattering errors, and reexamined them as well.

We therefore constructed a model of two-photon scattering errors during stimulated Raman transitions in trapped-ion qubits which incorporates all two-photon scattering processes, as well as the detuning dependencies of all system parameters involved. We also estimated the contribution to the scattering error from higher energy levels in m qubits and computed an upper bound on Rayleigh scattering error in both m and g qubits, finding this latter error to be negligible in all but the lightest ion species for most of the detuning range considered. We found that including all the above effects produced non-negligible corrections to simpler models of the systems, in particular that the more complete model implies there is no lower bound on Raman scattering-induced infidelity of g qubits as suggested by past models of such errors Ozeri, 2007. While we originally developed this theory for hyperfine qubits, it is easily extended to the Zeeman qubits we actually studied in our experiments.

Our experimental study of the scattering rates began from the observation that the inclusion or exclusion of the various features of the model predicted different slopes for the linear relationship between the scattering rate and laser beam intensity. This implied that we could test the accuracy of the calculations by measuring the scattering rate at various laser intensities, fitting a line to these points, and comparing the slope of the fit to the slope predicted by the theory. The experimental results provide strong evidence that the calculation is accurate, with fit slopes on each data set comfortably within one standard error of the theory slope. Our collaborators at UCLA conducted a similar experiment on g qubits in $^{133}Ba^{+}$ and obtained results that also verified the theory Boguslawski et al., 2022.

Finally, the results of the calculations (summarized in Table 8.1) show that, although m qubits have a lower bound on gate infidelity and the detunings and powers required for 10^{-4} error in m qubits are larger than in g qubits, low errors should still be experimentally achievable in m qubits because high power lasers are more readily available at the required wavelengths for the ion species considered. In sum, low Raman scattering errors are achievable in stimulated Raman-driven gates for both m and g trapped-ion qubits at sufficiently large red detunings.

		$^{9}Be^{+}$	$^{25}Mg^{+}$	$^{43}Ca^{+}$	$^{87}Sr^{+}$	$^{133}Ba^{+}$	$^{135}Ba^{+}$	$^{137}Ba^{+}$	$^{171}Yb^{+}$	$^{173}Yb^{+}$
$\omega_0/2\pi$ (GHz)	m	-	-	0.025	0.036	0.062	0.012	0.00047	-	-
	g	1.3	1.8	3.2	5.0	9.9	7.2	8.0	12.6	10.5
η	m	-	-	0.036	0.021	0.028	0.028	0.028	-	-
	g	0.213	0.143	0.077	0.053	0.038	0.038	0.038	0.046	0.047
$\Delta/2\pi$ (THz)	m	-	-	-40.0 (963 nm)	-66.0 (1335 nm)	-45.3 (676 nm)	-45.6 (677 nm)	-45.9 (677 nm)	-	-
	g	-1.00 (313 nm)	-4.55 (281 nm)	-9.05 (402 nm)	-13.0 (429 nm)	-26.4 (515 nm)	-26.6 (516 nm)	-26.9 (516 nm)	-15.3 (376 nm)	-15.4 (376 nm)
Power (W)	m	-	-	4.9	9.1	4.4	4.4	4.5	-	-
	g	0.067	0.13	0.30	0.37	0.94	0.96	0.98	0.67	0.67

TABLE 8.1. Comparison of g and m qubit gate characteristics. The qubit frequency for m and g qubits is given in the first two rows. The Lamb-Dicke parameter η is given for a 5 MHz trap frequency and counter-propagating beams at the $P_{3/2}$ resonances frequencies (resonance with $D_{5/2}$ and $S_{1/2}$ in m and g qubits, respectively). The detuning Δ corresponds to the detuning (from $P_{3/2}$ in m qubits and from $P_{1/2}$ in g qubits) required for 10^{-4} error, and the corresponding laser wavelength is given parenthetically below each detuning. Total power requirements are given for the 10^{-4} error threshold of the two-qubit Mølmer-Sørensen gate of Section 4.2.2, driven by 3 Raman beams.

APPENDIX A

DERIVATION OF SCATTERING RATE

To derive the general Raman ΛV scattering formula (Eqn. 4.6), begin with Eqn. 8.7.3 of Loudon, 2000,

$$\Gamma_{i\to f,\Lambda V} = \sum_{\boldsymbol{k}_{sc},\lambda} \frac{\pi e^4 \omega \omega_{sc} n}{2\epsilon_0^2 \hbar^2 V^2} \Big| \sum_k \Big(\frac{\langle f| \vec{r}\cdot\hat{\epsilon}_\lambda^* |k\rangle \langle k| \vec{r}\cdot\hat{\epsilon} |i\rangle}{\omega_k - \omega} + \frac{\langle f| \vec{r}\cdot\hat{\epsilon} |k\rangle \langle k| \vec{r}\cdot\hat{\epsilon}_\lambda^* |i\rangle}{\omega_k + \omega_{sc}} \Big) \Big|^2 \delta(\omega_{fi}+\omega_{sc}-\omega). \tag{A.1}$$

This equation describes the ΛV scattering rate to state f during virtual transitions from state i through the manifold containing the states indexed by k (where all these states are hyperfine sublevels). The transitions are driven by an n-photon laser beam of frequency ω and polarization $\hat{\epsilon}$, scattering a photon with frequency ω_{sc} and polarization $\hat{\epsilon}_\lambda^*$, where λ indexes the two independent polarizations in the chosen basis. The rate is calculated by summing contributions from all scattering modes $\boldsymbol{k}_{sc}, \lambda$ allowed in the quantization volume V. The frequencies can be understood by the energy level diagram of Fig. A.1.

Rearranging this equation, we find

$$\Gamma_{i\to f,\Lambda V} = \sum_{\boldsymbol{k}_{sc},\lambda} \frac{\hbar\omega n}{\epsilon_0 V} \frac{\pi e^4 \omega_{sc}}{2\epsilon_0 \hbar^3 V} \left| \sum_k \left(\frac{\langle f| \vec{r}\cdot\hat{\epsilon}_\lambda^* |k\rangle \langle k| \vec{r}\cdot\hat{\epsilon} |i\rangle}{\omega_k - \omega} + \frac{\langle f| \vec{r}\cdot\hat{\epsilon} |k\rangle \langle k| \vec{r}\cdot\hat{\epsilon}_\lambda^* |i\rangle}{\omega_k + \omega_{sc}} \right) \right|^2 \delta(\omega_{fi}+\omega_{sc}-\omega). \tag{A.2}$$

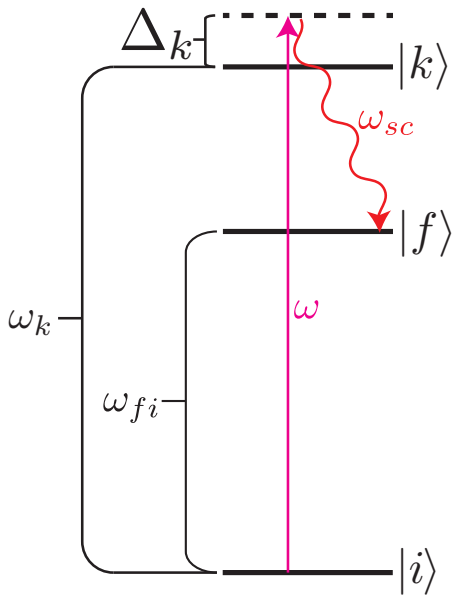

FIGURE A.1. Relevant frequency definitions for Eqn. A.1. The transitions are driven by a laser beam of frequency ω. Scattered photon frequency is given by $\omega_{sc} = \omega - \omega_{fi}$.

Now, if we model the laser field as a classical electric field plane wave with amplitude E,

$$\mathbf{E}_{\text{las}}(\mathbf{r}, t) = \frac{E}{2}\left(\hat{\epsilon}e^{i(\mathbf{k}\cdot\mathbf{r}-\omega t)} + \hat{\epsilon}^* e^{-i(\mathbf{k}\cdot\mathbf{r}-\omega t)}\right), \tag{A.3}$$

we can calculate the temporal and spatial average of

$$\langle \mathbf{E}^*_{\text{las}}(\mathbf{r}, t) \cdot \mathbf{E}_{\text{las}}(\mathbf{r}, t)\rangle = \frac{E^2}{2}. \tag{A.4}$$

Comparing this to the quantized result in an n photon Fock state, $\langle n|\, \hat{E}^\dagger \hat{E}\, |n\rangle = \frac{\hbar\omega}{\epsilon_0 V}(n + \frac{1}{2})$ allows us to make the replacement, assuming $n \gg 1$,

$$\frac{2\hbar\omega}{\epsilon_0 V} n \approx E^2 \tag{A.5}$$

to get

$$\Gamma_{i\to f,\Lambda V} = \sum_{\boldsymbol{k}_{sc},\lambda} \frac{E^2\pi e^4\omega_{sc}}{4\epsilon_0\hbar^3 V}\left|\sum_k \left(\frac{\langle f|\,\vec{r}\cdot\hat{\epsilon}^*_\lambda\,|k\rangle\,\langle k|\,\vec{r}\cdot\hat{\epsilon}\,|i\rangle}{\omega_k-\omega} + \frac{\langle f|\,\vec{r}\cdot\hat{\epsilon}\,|k\rangle\,\langle k|\,\vec{r}\cdot\hat{\epsilon}^*_\lambda\,|i\rangle}{\omega_k+\omega_{sc}}\right)\right|^2 \delta(\omega_{fi}+\omega_{sc}-\omega). \tag{A.6}$$

Next, we can take the limit of large quantization volume V,

$$\sum_{\boldsymbol{k}_{sc}} \to \frac{V}{(2\pi)^3}\iint d\omega_{sc}d\Omega\frac{\omega_{sc}^2}{c^3}, \tag{A.7}$$

enabling us to write the spontaneous scattering rate in the form

$$\Gamma_{i\to f,\Lambda V} = \sum_\lambda \iint d\omega_{sc}d\Omega\frac{E^2e^4\omega_{sc}^3}{32\pi^2c^3\epsilon_0\hbar^3}\left|\sum_k\left(\frac{\langle f|\,\vec{r}\cdot\hat{\epsilon}^*_\lambda\,|k\rangle\,\langle k|\,\vec{r}\cdot\hat{\epsilon}\,|i\rangle}{\omega_k-\omega} + \frac{\langle f|\,\vec{r}\cdot\hat{\epsilon}\,|k\rangle\,\langle k|\,\vec{r}\cdot\hat{\epsilon}^*_\lambda\,|i\rangle}{\omega_k+\omega_{sc}}\right)\right|^2 \delta(\omega_{fi}+\omega_{sc}-\omega). \tag{A.8}$$

Now we wish to perform the integral over $d\Omega \equiv d\phi\, d\theta\sin(\theta)$, the direction of the scattered photon's k-vector, $\hat{k}_{sc}$. For this, it is conceptually helpful to gather terms into an expression for the vector transition dipole matrix element for spontaneous scattering,

$$\vec{r}_{sc}(\omega_{sc}) \equiv \frac{Ee}{2\hbar}\sum_k\left(\frac{\langle f|\,\vec{r}\,|k\rangle\,\langle k|\,\vec{r}\cdot\hat{\epsilon}\,|i\rangle}{\omega_k-\omega} + \frac{\langle f|\,\vec{r}\cdot\hat{\epsilon}\,|k\rangle\,\langle k|\,\vec{r}\,|i\rangle}{\omega_k+\omega_{sc}}\right) \tag{A.9}$$

which allows us to write Eq. (A.8) in the form

$$\Gamma_{i\to f,\Lambda V} = \sum_\lambda \iint d\omega_{sc}d\Omega\frac{e^2\omega_{sc}^3}{8\pi^2c^3\epsilon_0\hbar}|\vec{r}_{sc}\cdot\hat{\epsilon}^*_\lambda|^2\delta(\omega_{fi}+\omega_{sc}-\omega). \tag{A.10}$$

Without loss of generality, we will choose a polarization basis such that one of the basis polarization vectors lies in the plane of $\vec{r}_{sc}$ and $\hat{k}_{sc}$; we will call this vector $\hat{\epsilon}_{sc}$ (note that the other basis vector will not contribute to the scattering, as it will necessarily be perpendicular to $\vec{r}_{sc}$). Choosing θ to be the angle between $\vec{r}_{sc}$ and $\vec{k}_{sc}$, the angle between $\vec{r}_{sc}$ and $\hat{\epsilon}_{sc}$ is $\frac{\pi}{2} - \theta$, which implies

$$\begin{aligned} |\vec{r}_{sc} \cdot \hat{\epsilon}_{sc}|^2 =& |\vec{r}_{sc}|^2 \cos^2\left(\tfrac{\pi}{2} - \theta\right) \\ =& |\vec{r}_{sc}|^2 \sin^2(\theta), \end{aligned} \tag{A.11}$$

allowing us to carry out the integral over the direction of the spontaneously emitted photon to get

$$\begin{aligned} \Gamma_{i\to f,\Lambda\mathrm{V}} =& \int d\omega_{sc} \frac{e^2\omega_{sc}^3}{3\pi c^3\epsilon_0\hbar} |\vec{r}_{sc}(\omega_{sc})|^2 \delta(\omega_{fi} + \omega_{sc} - \omega) \\ =& \frac{e^2(\omega-\omega_{fi})^3}{3\pi c^3\epsilon_0\hbar} |\vec{r}_{sc}(\omega-\omega_{fi})|^2 \\ =& \frac{e^2(\omega-\omega_{fi})^3}{3\pi c^3\epsilon_0\hbar} \left(|\vec{r}_{sc}(\omega-\omega_{fi})|\right)^2 \\ =& \frac{e^2(\omega-\omega_{fi})^3}{3\pi c^3\epsilon_0\hbar} \left(\sqrt{\sum_q |\vec{r}_{sc}(\omega-\omega_{fi}) \cdot \hat{\mathbf{e}}_q|^2}\right)^2 \\ =& \frac{e^2(\omega-\omega_{fi})^3}{3\pi c^3\epsilon_0\hbar} \sum_q |\vec{r}_{sc}(\omega-\omega_{fi}) \cdot \hat{\mathbf{e}}_q|^2 \\ =& \frac{E^2e^4(\omega-\omega_{fi})^3}{12\pi c^3\epsilon_0\hbar^3} \sum_q \left| \sum_k \left(\frac{\langle f|\, \vec{r}\cdot\hat{\mathbf{e}}_q\, |k\rangle \langle k|\, \vec{r}\cdot\hat{\epsilon}\, |i\rangle}{\omega_k - \omega} + \frac{\langle f|\, \vec{r}\cdot\hat{\epsilon}\, |k\rangle \langle k|\, \vec{r}\cdot\hat{\mathbf{e}}_q\, |i\rangle}{\omega_k + \omega - \omega_{fi}} \right) \right|^2 \end{aligned} \tag{A.12}$$

where $\hat{\mathbf{e}}_q$ is a polarization vector corresponding to π, σ^+, or σ^-, with q indexing these possibilities.

Now, if $\Delta_k \equiv \omega - \omega_k$ is the detuning relative to some level k, we see that we can write $\omega - \omega_{fi}$ as $\omega_k - \omega_{fi} + \Delta_k$. Since we choose to measure the detuning relative to the $P_{3/2}$ manifold, we define $\Delta = \omega - \omega_{Pi}$, where ω_{Pi} is the frequency of the transtion between the manifold containing $|i\rangle$ and $P_{3/2}$. This allows us to rewrite $\omega - \omega_{fi}$ as $\omega_{Pf} + \Delta$, where ω_{Pf} is the frequency of the transition between the manifold containing state f and $P_{3/2}$; additionally, we may rewrite $\omega_k - \omega$ as $\omega_k - \omega_{Pi} - \Delta$. Rewriting $\omega - \omega_{fi}$ as such and rearranging gives us

$$\begin{aligned}\Gamma_{i\to f,\Lambda\mathrm{V}} &= \frac{E^2 e^4 \omega_{Pf}^3}{12\pi c^3 \epsilon_0 \hbar^3} \sum_q \left| \sum_k \left(\frac{\langle f|\, \vec{r}\cdot\hat{\mathbf{e}}_q\, |k\rangle \langle k|\, \vec{r}\cdot\hat{\epsilon}\, |i\rangle}{\omega_k - \omega_{Pi} - \Delta} + \frac{\langle f|\, \vec{r}\cdot\hat{\epsilon}\, |k\rangle \langle k|\, \vec{r}\cdot\hat{\mathbf{e}}_q\, |i\rangle}{\omega_k + \omega_{Pf} + \Delta} \right) \right|^2 \left(1 + \frac{\Delta}{\omega_{Pf}}\right)^3 \\ &= \frac{e^4 \omega_{Pf}^3}{3\pi c^3 \epsilon_0 \hbar} \frac{E^2}{4\hbar^2} \sum_q \left| \sum_k \left(\frac{\langle f|\, \vec{r}\cdot\hat{\mathbf{e}}_q\, |k\rangle \langle k|\, \vec{r}\cdot\hat{\epsilon}\, |i\rangle}{\omega_k - \omega_{Pi} - \Delta} + \frac{\langle f|\, \vec{r}\cdot\hat{\epsilon}\, |k\rangle \langle k|\, \vec{r}\cdot\hat{\mathbf{e}}_q\, |i\rangle}{\omega_k + \omega_{Pf} + \Delta} \right) \right|^2 \left(1 + \frac{\Delta}{\omega_{Pf}}\right)^3 .\end{aligned} \tag{A.13}$$

We begin the next step by noting Eqn. 4.3,

$$\frac{e^2 \omega_{Pf}^3}{3\pi\epsilon_0 \hbar c^3} \mu_{Pf}^2 = \frac{1}{\tau_{fl}} \equiv \gamma_{Pf}$$

where γ_{Pf} is the decay rate from the $P_{3/2}$ manifold to the manifold containing state f; this is given by $\alpha_f \gamma$, where α_f is the branching ratio into the manifold containing state f and γ is the total spontaneous decay rate for the manifold containing state l. With this, we can write

$$\Gamma_{i\to f,\Lambda V} = \frac{\gamma_{Pf}}{\mu_{Pf}^2}\frac{e^2E^2}{4\hbar^2}\sum_q\left|\sum_k\left(\frac{\langle f|\,\vec{r}\cdot\hat{\mathbf{e}}_q\,|k\rangle\,\langle k|\,\vec{r}\cdot\hat{\epsilon}\,|i\rangle}{\omega_k-\omega_{Pi}-\Delta}+\frac{\langle f|\,\vec{r}\cdot\hat{\epsilon}\,|k\rangle\,\langle k|\,\vec{r}\cdot\hat{\mathbf{e}}_q\,|i\rangle}{\omega_k+\omega_{Pf}+\Delta}\right)\right|^2\left(1+\frac{\Delta}{\omega_{Pf}}\right)^3$$
$$=\gamma_{Pf}\frac{e^2E^2}{4\hbar^2}\sum_q\left|\sum_k\left(\frac{\langle f|\,\vec{r}\cdot\hat{\mathbf{e}}_q\,|k\rangle\,\langle k|\,\vec{r}\cdot\hat{\epsilon}\,|i\rangle}{\mu_{Pf}(\omega_k-\omega_{Pi}-\Delta)}+\frac{\langle f|\,\vec{r}\cdot\hat{\epsilon}\,|k\rangle\,\langle k|\,\vec{r}\cdot\hat{\mathbf{e}}_q\,|i\rangle}{\mu_{Pf}(\omega_k+\omega_{Pf}+\Delta)}\right)\right|^2\left(1+\frac{\Delta}{\omega_{Pf}}\right)^3. \tag{A.14}$$

Now we divide and multiply by μ_{Pi}, *i.e.*, the matrix element of Eqn. 5.2 between the $P_{3/2}$ and the manifold containing i.

$$\Gamma_{i\to f,\Lambda V}=\gamma_{Pf}\frac{e^2E^2}{4\hbar^2}\sum_q\left|\sum_k\mu_{Pi}\left(\frac{\langle f|\,\vec{r}\cdot\hat{\mathbf{e}}_q\,|k\rangle\,\langle k|\,\vec{r}\cdot\hat{\epsilon}\,|i\rangle}{\mu_{Pf}\mu_{Pi}(\omega_k-\omega_{Pi}-\Delta)}+\frac{\langle f|\,\vec{r}\cdot\hat{\epsilon}\,|k\rangle\,\langle k|\,\vec{r}\cdot\hat{\mathbf{e}}_q\,|i\rangle}{\mu_{Pf}\mu_{Pi}(\omega_k+\omega_{Pf}+\Delta)}\right)\right|^2\left(1+\frac{\Delta}{\omega_{Pf}}\right)^3$$

$$=\gamma_{Pf}\frac{e^2E^2\mu_{Pi}^2}{4\hbar^2}\sum_q\left|\sum_k\left(\frac{\langle f|\,\vec{r}\cdot\hat{\mathbf{e}}_q\,|k\rangle\,\langle k|\,\vec{r}\cdot\hat{\epsilon}\,|i\rangle}{\mu_{Pf}\mu_{Pi}(\omega_k-\omega_{Pi}-\Delta)}+\frac{\langle f|\,\vec{r}\cdot\hat{\epsilon}\,|k\rangle\,\langle k|\,\vec{r}\cdot\hat{\mathbf{e}}_q\,|i\rangle}{\mu_{Pf}\mu_{Pi}(\omega_k+\omega_{Pf}+\Delta)}\right)\right|^2\left(1+\frac{\Delta}{\omega_{Pf}}\right)^3. \tag{A.15}$$

Noting the definition of g_{Pi} (Eqn. 4.5), this becomes

$$\Gamma_{i\to f,\Lambda V}=\gamma_{Pf}g_{Pi}^2\sum_q\left|\sum_k\left(\frac{\langle f|\,\vec{r}\cdot\hat{\mathbf{e}}_q\,|k\rangle\,\langle k|\,\vec{r}\cdot\hat{\epsilon}\,|i\rangle}{\mu_{Pf}\mu_{Pi}(\omega_k-\omega_{Pi}-\Delta)}+\frac{\langle f|\,\vec{r}\cdot\hat{\epsilon}\,|k\rangle\,\langle k|\,\vec{r}\cdot\hat{\mathbf{e}}_q\,|i\rangle}{\mu_{Pf}\mu_{Pi}(\omega_k+\omega_{Pf}+\Delta)}\right)\right|^2\left(1+\frac{\Delta}{\omega_{Pf}}\right)^3. \tag{A.16}$$

Finally, we make our result applicable to gates; we do so by averaging over the undisturbed state $|i\rangle$ during the course of the gate. If we consider a $\hat{\sigma}_x$ gate,

then an ion initially in the state $|0\rangle$ will get mapped to $|1\rangle$. The ion's state $|i\rangle$ then has a time dependence given by $|i(t)\rangle = \cos(2\pi t/\tau)\,|0\rangle + \sin(2\pi t/\tau)\,|1\rangle$, where τ is the gate time. Considering this time dependence and averaging Eqn. A.16 over the gate time gives

$$\Gamma_{f,\Lambda\mathrm{V}} = \gamma_{Pf}\frac{g_{Pi}^2}{2}\sum_{i,q}\left|\sum_k\left(\frac{\langle f|\,\vec{r}\cdot\hat{\mathbf{e}}_q\,|k\rangle\,\langle k|\,\vec{r}\cdot\hat{\epsilon}\,|i\rangle}{\mu_{Pf}\mu_{Pi}(\omega_k-\omega_{Pi}-\Delta)}+\frac{\langle f|\,\vec{r}\cdot\hat{\epsilon}\,|k\rangle\,\langle k|\,\vec{r}\cdot\hat{\mathbf{e}}_q\,|i\rangle}{\mu_{Pf}\mu_{Pi}(\omega_k+\omega_{Pf}+\Delta)}\right)\right|^2\left(1+\frac{\Delta}{\omega_{Pf}}\right)^3, \tag{A.17}$$

where $|i\rangle$ now indexes the two qubit states, $|0\rangle$ and $|1\rangle$.

By the same reasoning, we can get the ladder scattering rate (which contributes in m qubits but not g qubits),

$$\Gamma_{f,\mathrm{lad}} = \gamma_{Pf}\frac{g_{Pi}^2}{2}\sum_{i,q}\left|\sum_k\left(\frac{\langle f|\,\vec{r}\cdot\hat{\mathbf{e}}_q\,|k\rangle\,\langle k|\,\vec{r}\cdot\hat{\epsilon}^*\,|i\rangle}{\mu_{Pf}\mu_{Pi}\,(\omega_{kP}+\Delta+2\omega_{PD})}\right.\right.$$
$$\left.\left.+\frac{\langle f|\,\vec{r}\cdot\hat{\epsilon}^*\,|k\rangle\,\langle k|\,\vec{r}\cdot\hat{\mathbf{e}}_q\,|i\rangle}{\mu_{Pf}\mu_{Pi}\,(\omega_{kP}-\Delta+\omega_{Df})}\right)\right|^2\left(1-\frac{2\omega_{PD}+\Delta}{\omega_{Pf}}\right)^3. \tag{A.18}$$

To generate the full model scattering rate, we sum over all scattering events $i \to f$ except for $i \to i$ scattering events, since we are ignoring Rayleigh scattering.

We can get the simplified model's scattering rate equation by neglecting the V scattering term in Eqn. A.17 and assuming $(1+\Delta/\omega_{Pf})^3 \approx 1$

$$\Gamma_f \approx \gamma_{Pf}\frac{g_{Pi}^2}{2}\sum_i\left|\sum_{k,q}\frac{\langle f|\,\vec{r}\cdot\hat{\mathbf{e}}_q\,|k\rangle\,\langle k|\,\vec{r}\cdot\hat{\epsilon}\,|i\rangle}{\mu_{Pf}\mu_{Pi}\,(\omega_{kP}-\Delta)}\right|^2. \tag{A.19}$$

We can again obtain the Raman scattering rate by summing over all scattering events except for $i \to i$.

APPENDIX B

DECAY RATE FROM FERMI'S GOLDEN RULE

Here we derive Eqn. 4.3. To do so, begin with Fermi's Golden Rule (Eqn. 1 in J. M. Zhang and Liu, 2016) for the rate of spontaneous decay from excited atomic state i to a state f,

$$\gamma_{i\to f} = \frac{2\pi}{\hbar}\left|\langle f|\,\hat{H}_I\,|i\rangle\right|^2 \rho(E_{\omega_0}) \tag{B.1}$$

where $\rho(E_{\omega_0})$ is the density of states in energy at the energy of a photon with frequency ω_0 (the resonant frequency of the transition between i and f), and $\hat{H}_I$ is the interaction Hamiltonian. The corresponding matrix element is given by (see §2.2 of Metcalf and Straten, 1999)

$$\langle f|\,\hat{H}_I\,|i\rangle = e\sqrt{\frac{\hbar\omega_0}{2\epsilon_0 V}}\,\langle f|\,\vec{d}\cdot\hat{\epsilon}_{sc}\,|i\rangle$$

where V is the quantization volume, $\vec{d}$ is the dipole operator, and $\hat{\epsilon}_{sc}$ is the polarization unit vector of the scattered photon. Putting these together, we get

$$\gamma_{i\to f} = \frac{\pi e^2\omega_0}{\epsilon_0 V}\left|\langle f|\,\vec{d}\cdot\hat{\epsilon}_{sc}\,|i\rangle\right|^2 \rho(E_{\omega_0}) \tag{B.2}$$

Now, to find $\rho(E_{\omega_0})$, we consider the number of modes N, i.e, the sum of 1 over all polarizations and wave vectors, which for large quantization volume V (see eqn 1.1.11 in Loudon, 2000) goes as

$$N = \sum_{\lambda} \sum_{\boldsymbol{k}_{sc}} 1 \to 2\frac{V}{(2\pi)^3} \int \int d\omega_{sc} d\Omega \frac{\omega_{sc}^2}{c^3} = 2\frac{V}{\hbar(2\pi)^3} \int \int dE_{\omega_{sc}} d\Omega \frac{\omega_{sc}^2}{c^3} = \frac{V}{\pi^2 \hbar} \int dE_{\omega_{sc}} \frac{\omega_{sc}^2}{c^3} \tag{B.3}$$

where the first factor of 2 came from the sum over the two independent polarizations λ. So

$$\rho(E_{\omega_0}) = \frac{V\omega_0^2}{\pi^2 \hbar c^3} \tag{B.4}$$

which gives

$$\gamma_{i\to f} = \frac{\pi e^2 \omega_0}{\epsilon_0 V} \frac{V\omega_0^2}{\pi^2 \hbar c^3} \left| \langle f | \, \vec{d} \cdot \hat{\epsilon}_{sc} \, | i \rangle \right|^2 = \frac{e^2 \omega_0^3}{\pi \epsilon_0 \hbar c^3} \left| \langle f | \, \vec{d} \cdot \hat{\epsilon}_{sc} \, | i \rangle \right|^2 \tag{B.5}$$

and, finally, after averaging over the random polarization direction,

$$\gamma_{i\to f} = \frac{e^2 \omega_0^3}{3\pi \epsilon_0 \hbar c^3} \left| \langle f | \, |\vec{d}| \, | i \rangle \right|^2 \tag{B.6}$$

APPENDIX C

POWER REQUIREMENTS DERIVATION

Here we derive the expressions given in Section 4.3. For a Gaussian laser beam of power $\mathscr{P}$ we consider Steck, n.d.:

$$E^2 = \frac{4\mathscr{P}}{\pi \mathrm{w}_0^2 c \epsilon_0}, \tag{C.1}$$

$$\frac{\gamma}{g_{Pi}^2} = \frac{\hbar \omega_{Pi}^3 \mathrm{w}_0^2}{3c^2 \mathscr{P} \alpha_q}, \tag{C.2}$$

where w_0 is the laser beam waist and α_q is the branching ratio for transitions between $P_{3/2}$ and the qubit manifold. Note that in general $|\Omega_R| = g_{Pi}^2 r(\Delta)$ for some $r(\Delta)$, so we can replace g_{Pi}^2 with $|\Omega_R|/r(\Delta)$. This means that the power can be written as

$$\mathscr{P} = \frac{\hbar \omega_{Pi}^3 \mathrm{w}_0^2}{3c^2 \alpha_q \gamma} \frac{|\Omega_R|}{r(\Delta)}. \tag{C.3}$$

For a single-qubit gate, $|\Omega_R| = \pi/2\tau_{1q}$ where τ_{1q} is the gate time; for a two-qubit gate, $|\Omega_R| = \pi\sqrt{K}/2\sqrt{2}\tau_{2q}\eta(\Delta)$. This allows us to write the total power required for each as a function of Δ:

$$\mathscr{P}_{1q}(\Delta) = 2\frac{\hbar \omega_{Pi}^3 \mathrm{w}_0^2}{6c^2 \alpha_q \gamma} \frac{\pi}{\tau_{1q} r(\Delta)} \tag{C.4}$$

and

$$\mathscr{P}_{2q}(\Delta) = 4\frac{\hbar \omega_{Pi}^3 \mathrm{w}_0^2}{6\sqrt{2}c^2 \alpha_q \gamma} \frac{\pi\sqrt{K}}{\tau_{2q}\eta(\Delta) r(\Delta)}, \tag{C.5}$$

where the factor of 2 in front of Eqn. C.4 is due to the use of two beams of equal power, and the factor of 4 in front of Eqn. C.5 is due to the use of two beams of equal power along with one beam with double the power.

If, as we did in Section 4.2, we neglect the effects of large detuning, we can write power as a function of the gate error directly. We will start by rewriting $r(\Delta) = 2/15|\Delta|$ in terms of the single-qubit gate error ϵ_{1q},

$$\epsilon_{1q} = \rho\frac{\pi\gamma}{|\Delta|} = \rho\frac{15\pi\gamma r(\Delta)}{2}$$

$$\implies r(\Delta) = \tfrac{2\epsilon_{1q}}{15\rho\pi\gamma}, \text{(C.6)or for a two-qubit gate,}$$

$$\begin{aligned}\epsilon_{2q} = \rho\frac{\pi\gamma}{|\Delta|}\frac{4\sqrt{K}}{\sqrt{2}\eta} = \rho\frac{15\pi\gamma r(\Delta)}{2}\frac{4\sqrt{K}}{\sqrt{2}\eta} \\ \implies r(\Delta) = \frac{2\epsilon_{2q}}{15\rho\pi\gamma}\frac{\sqrt{2}\eta}{4\sqrt{K}}.\end{aligned} \tag{C.7}$$

Substituting into Eqns. C.4 and C.5, we get

$$\mathscr{P}_{1q}(\epsilon_{1q}) = \rho\frac{5\pi\hbar\omega_{Pi}^3 \mathrm{w}_0^2}{2c^2\epsilon_{1q}\alpha_q}\frac{\pi}{\tau_{1q}} \tag{C.8}$$

and

$$\mathscr{P}_{2q}(\epsilon_{2q}) = \rho\frac{10\pi\hbar\omega_{Pi}^3 \mathrm{w}_0^2}{c^2\epsilon_{2q}\alpha_q}\frac{\pi}{\tau_{2q}}\frac{K}{\eta^2}. \tag{C.9}$$

APPENDIX D

RECOVERING CLASSICAL LIMITS

We can test the completeness of our model by seeing if it is able to recover classical elastic scattering behavior in the limit of large detuning. Considering only elastic scattering excludes ladder scattering processes (since they are inelastic). This means we can write the elastic scattering rate as

$$\Gamma = E^2 \frac{e^4 \omega_L^3}{12\pi c^3 \epsilon_0 \hbar^3} \left| \sum_k |\langle i| \vec{r} |k\rangle|^2 \left(\frac{1}{\omega_{ki} - \omega_L} + \frac{1}{\omega_{ki} + \omega_L} \right) \right|^2 . \tag{D.1}$$

For Raman beams with intensity I, we have $E^2 = 2I/\epsilon_0 c$; additionally, we can replace the scattering rate with the scattering cross-section σ via $\sigma = \Gamma \hbar \omega_L / I$. Putting these equations together, we get

$$\sigma = \alpha^2 \frac{8\pi}{3} \frac{\omega_L^4}{c^2} \left| \sum_k |\langle i| \vec{r} |k\rangle|^2 \left(\frac{1}{\omega_{ki} - \omega_L} + \frac{1}{\omega_{ki} + \omega_L} \right) \right|^2 , \tag{D.2}$$

where $\alpha = e^2/4\pi\epsilon_0 \hbar c$ is the fine structure constant.

Now we can calculate the limits. For large blue detuning ($\omega_L \gg \omega_{ki}$ for every k), we have

$$\left(\frac{1}{\omega_{ki} - \omega_L} + \frac{1}{\omega_{ki} + \omega_L} \right) \approx -2 \frac{\omega_{ki}}{\omega_L^2}, \tag{D.3}$$

allowing us to rewrite Eqn. D.2 as

$$\sigma_{\text{blue}} = \alpha^2 \frac{32\pi}{3} \frac{1}{c^2} \left| \sum_k \omega_{ki} |\langle i| \vec{r} |k\rangle|^2 \right|^2 . \tag{D.4}$$

Using the Thomas-Reiche-Kuhn sum rule (for the single valence electron only, and neglecting recoil and the ion's monopole charge), the sum can be evaluated to

$$\sum_k \omega_{ki} |\langle i|\,\vec{r}\,|k\rangle|^2 = \frac{\hbar}{2m_e}. \tag{D.5}$$

This gives

$$\sigma_{\text{blue}} = \alpha^2 \frac{32\pi}{3} \frac{1}{c^2} \frac{\hbar^2}{4m_e^2} = \frac{8\pi}{3}\alpha^4 a_0^2, \tag{D.6}$$

where a_0 is the Bohr radius and $\alpha^2 a_0$ is the classical electron radius. So for large blue detuning, the model recovers the Thomson cross-section of the valence electron.

For red-detuning, ($\omega_L \ll \omega_{ki}$ for every k), we have

$$\left(\frac{1}{\omega_{ki} - \omega_L} + \frac{1}{\omega_{ki} + \omega_L}\right) \approx \frac{2}{\omega_{ki}}, \tag{D.7}$$

giving

$$\sigma_{\text{red}} = \alpha^2 \frac{8\pi}{3} \frac{\omega_L^4}{c^2} \left| \sum_k \frac{2|\langle i|\,\vec{r}\,|k\rangle|^2}{\omega_{ki}} \right|^2. \tag{D.8}$$

The DC polarizability of the ion can be written as

$$\alpha^{(0)} \equiv e^2 \sum_{k \neq i} \frac{\langle i|\,\vec{r}\,|k\rangle \langle k|\,\vec{r}\,|i\rangle + \langle k|\,\vec{r}\,|i\rangle \langle i|\,\vec{r}\,|k\rangle}{E_k - E_i}, \tag{D.9}$$

allowing us to rewrite Eqn. (D.8) as

$$\begin{aligned}\sigma_{\rm red} &= \frac{8\pi}{3}\alpha^2\frac{\omega_L^4}{c^2e^4}\hbar^2|\alpha^{(0)}|^2 \\ &= \frac{8\pi}{3}\left(\frac{\omega_L}{c}\right)^4\hbar^2|\frac{\alpha^{(0)}}{4\pi\epsilon_0}|^2 \\ &= \frac{8\pi}{3}k_L^4\hbar^2|\alpha^{(0)}|^2.\end{aligned} \tag{D.10}$$

We can compare to the classical result by using the Clausius-Mossotti relation,

$$|\alpha^{(0)}|^2 = \left(\frac{3\epsilon_0}{N}\right)^2\left(\frac{\epsilon_r-1}{\epsilon_r+2}\right) = \left(\frac{3\epsilon_0}{N}\right)^2\left(\frac{n^2-1}{n^2+2}\right) \approx \left(\frac{3\epsilon_0}{N}\right)^2\frac{4}{9}(n-1)^2, \tag{D.11}$$

where N is the number density of particles in the material, ϵ_r is the dielectric constant, and n is the refractive index. The second equality is true for non-magnetic media, and the third, approximate equality holds when $n \approx 1$. Applying this to Eqn. (D.10), we find

$$\sigma_{\rm red} \approx \frac{2k_L^4}{3\pi N^2}|n-1|^2, \tag{D.12}$$

which is the expression for classical Rayleigh scattering (*e.g.* Jackson, 1999). Note that if we had ignored the V scattering process, *i.e.*, the $1/(\omega_{ki}+\omega_L)$ term, we would not have recovered the correct limits.

APPENDIX E

QUANTUM CRYPTOGRAPHY PROTOCOL

Below, I detail a quantum cryptography protocol I helped develop with Steven van Enk Moore and Enk, 2021.

Suppose that Alice and Bob are preaparing and sending separable qubit states α_A and β_B, respectively, to a joint measurement device represented by a measurement operator ξ_{AB}. Then the probability of getting a given measurement is

$$P = \mathrm{Tr}(\alpha_A \otimes \beta_B \xi_{AB}) \tag{E.1}$$

If Alice and Bob together would like to be able to tomographically reconstruct the two-qubit measurement operator ξ, they each need to prepare 4 different (linearly independent) states of their qubits. Given probabilities of the form (E.1), Alice and Bob can gather the measured frequencies of detector "clicks" in a 4-by-4 data matrix whose expectation value should (*if* there is a unique single-valued operator ξ) have the form

$$F^{kl} = \mathrm{Tr}\{\alpha_A^k \otimes \beta_B^l \, \xi_{AB}\} \tag{E.2}$$

for $k, l = 1 \ldots 4$. The trace on the right-hand-side of Eq. (E.2) can be calculated by expanding all operators in the Pauli basis as follows

$$\alpha^k = \sum_i \alpha_i^k \, \sigma_i, \quad \beta^l = \sum_i \beta_i^l \, \sigma_i, \quad \xi = \sum_{i,j} x_{ij} \, \sigma_i \otimes \sigma_j. \tag{E.3}$$

Substituting these expansions into the definition of the data matrix and noting that

$$\mathrm{Tr}\{\sigma_i\sigma_j \otimes \sigma_k\sigma_l\} = 4\delta_{ij}\delta_{kl}, \tag{E.4}$$

yields the equation

$$F^{kl} = 4\sum_{i,j} x_{ij}\alpha_i^k\beta_j^l. \tag{E.5}$$

Eliminating the factor of four by defining $S = F/4$, we can rewrite the equation for S as a matrix equation

$$S = A^T X B \tag{E.6}$$

where X has matrix element x_{ij} and A has columns made from vectors of the Pauli expansion coefficients of Alice's operators, and B is similarly defined for Bob. Multiplying both sides of this equation on the left by $(A^T)^{-1}$ [we assume the inverse exists, i.e., we assume Alice's 4 operators to be linearly independent] yields

$$(A^T)^{-1}S = XB. \tag{E.7}$$

Now we assume that both Alice and Bob have control over their own operators such that these operators do not vary over the course of the experiment. Next, suppose that there are two trials, each using a different (not identical) set of operators α^k for Alice but the same set of operators β^l for Bob. Then we can eliminate the unknown matrix X and write the condition on there being a unique X that does not depend on which operators α^k Alice is using, as

$$(A_1^T)^{-1}S_1 = (A_2^T)^{-1}S_2, \tag{E.8}$$

where the left-hand and right-hand sides of the equation represent trials with different operators $\alpha^{k'}$. One alternative useful way of rewriting this same equation is

$$S_1 S_2^{-1} A_2^T (A_1^T)^{-1} = \mathbb{1}, \tag{E.9}$$

even though this may fail, namely, if S_2 is not invertible. It is helpful to write this matrix product out in terms of the coefficients:

$$\sum_{k,l,m} (S_1)_{ik} (S_2^{-1})_{kl} (A_2^T)_{lm} ((A_1^T)^{-1})_{mj} = \delta_{ij} \tag{E.10}$$

Written this way, it is easy to see how this equation can be used to test for dependence of ξ on Alice's operators: suppose, without loss of generality, that ξ is somehow different for the operator α_A^i of the first trial. Then every row but the ith row of S_1 is inverted by the remaining three matrices. Therefore, only the ith row of the left-hand side matrix will differ from the identity. Conversely, since Alice is able to calculate the left-hand side of (E.10) just from her knowledge of her operators α^k and from the data matrices S_1 and S_2 she can diagnose, without needing any knowledge about Bob's operators β^l, with which of her state preparations the measurement is correlated. She also does not need to reconstruct the measurement operator ξ.

Note that all we need for this to work is that the trials are not identical. That is, Alice needs just 5 different states at a minimum [to make two non-identical sets of 4 states] to be able to run this check.

(By symmetry, Bob could diagnose the presence of correlations between ξ and *his* states β^l without needing knowledge of Alice's operators. In this case Bob would need to prepare at least 5 different states.)

Bibliography

Allcock, D. T. C. et al. (2021). "*omg* blueprint for trapped ion quantum computing with metastable states". In: *Applied Physics Letters* 119.21, p. 214002. DOI: 10.1063/5.0069544. URL: http://dx.doi.org/10.1063/5.0069544.

Ansbacher, W., Y. Li and E. H. Pinnington (1989). "Precision lifetime measurement for the $3P$ levels of Mg II using frequency-doubled laser radiation to excite a fast ion beam". In: *Physics Letters A* 139.3, pp. 165–169. DOI: https://doi.org/10.1016/0375-9601(89)90353-8. URL: https://www.sciencedirect.com/science/article/pii/0375960189903538.

Ballance, C. J. (2014). "High Fidelity Quantum Logic in Ca^+". University of Oxford.

Barakhshan, P. et al. (n.d.). *Portal for High-Precision Atomic Data and Computation* (version 1.0). University of Delaware, Newark, DE, USA. URL: https://www.udel.edu/atom [January 2021].

Bazavan, O. et al. (2023). "Synthesizing a $\hat{\sigma}_z$ spin-dependent force for optical, metastable, and ground-state trapped-ion qubits". In: *Phys. Rev. A* 107 (2), p. 022617. DOI: 10.1103/PhysRevA.107.022617. URL: https://link.aps.org/doi/10.1103/PhysRevA.107.022617.

Boguslawski, Matthew J. et al. (2022). *Errors in stimulated-Raman-induced logic gates in* $^{133}Ba^+$. arXiv: 2212.02608 [quant-ph].

Bourdeauducq, Sébastien et al. (2016). *ARTIQ 1.0*. Version 1.0. DOI: 10.5281/zenodo.51303. URL: https://doi.org/10.5281/zenodo.51303.

Brink, D. M. and G. R. Satchler (1968). *Angular Momentum*.

Bruzewicz, C. D. et al. (2019). "Dual-species, multi-qubit logic primitives for Ca+/Sr+ trapped-ion crystals". In: *npj Quantum Information* 5.1, p. 102. DOI: 10.1038/s41534-019-0218-z. URL: https://doi.org/10.1038/s41534-019-0218-z.

Burton, William Cody et al. (2023). "Transport of Multispecies Ion Crystals through a Junction in a Radio-Frequency Paul Trap". In: *Phys. Rev. Lett.* 130 (17), p. 173202. DOI: 10.1103/PhysRevLett.130.173202. URL: https://link.aps.org/doi/10.1103/PhysRevLett.130.173202.

Cirac, J. I. and P. Zoller (1995). "Quantum Computations with Cold Trapped Ions". In: *Phys. Rev. Lett.* 74 (20), pp. 4091–4094. DOI: 10.1103/PhysRevLett.74.4091. URL: https://link.aps.org/doi/10.1103/PhysRevLett.74.4091.

Cline, R. A. et al. (1994). "Spin relaxation of optically trapped atoms by light scattering". In: *Opt. Lett.* 19.3, pp. 207–209. DOI: 10.1364/OL.19.000207. URL: http://opg.optica.org/ol/abstract.cfm?URI=ol-19-3-207.

Curtis, M. (2010). "Measurement-Selected Ensembles in Trapped-Ion Qubits". unpublished thesis. University of Oxford.

Eschner, Jürgen et al. (2003). "Laser cooling of trapped ions". In: *J. Opt. Soc. Am. B* 20.5, pp. 1003–1015. DOI: 10.1364/JOSAB.20.001003. URL: https://opg.optica.org/josab/abstract.cfm?URI=josab-20-5-1003.

Feldker, T. et al. (2018). "Spectroscopy of the $^2S_{1/2} \rightarrow ^2 P_{3/2}$ transition in Yb II: Isotope shifts, hyperfine splitting, and branching ratios". In: *Phys. Rev. A* 97 (3), p. 032511. DOI: 10.1103/PhysRevA.97.032511. URL: https://link.aps.org/doi/10.1103/PhysRevA.97.032511.

Gosselin, R. N., E. H. Pinnington and W. Ansbacher (1988). "Measurement of the lifetimes of the $4P$ levels in Ca II using laser excitation of a fast beam". In: *Phys. Rev. A* 38 (9), pp. 4887–4890. DOI: 10.1103/PhysRevA.38.4887. URL: https://link.aps.org/doi/10.1103/PhysRevA.38.4887.

Hayes, David et al. (2011). "Reducing sequencing complexity in dynamical quantum error suppression by Walsh modulation". In: *Phys. Rev. A* 84 (6), p. 062323. DOI: 10.1103/PhysRevA.84.062323. URL: https://link.aps.org/doi/10.1103/PhysRevA.84.062323.

Home, J. P. et al. (2009). "Memory coherence of a sympathetically cooled trapped-ion qubit". In: *Phys. Rev. A* 79 (5), p. 050305. DOI: 10.1103/PhysRevA.79.050305. URL: https://link.aps.org/doi/10.1103/PhysRevA.79.050305.

Hughes, A (2021). "Benchmarking memory and logic gates for trapped-ion quantum computing". unpublished thesis. PhD thesis. University of Oxford.

Hughes, A. C. et al. (2020). "Benchmarking a High-Fidelity Mixed-Species Entangling Gate". In: *Phys. Rev. Lett.* 125 (8), p. 080504. DOI: 10.1103/PhysRevLett.125.080504.

Jackson, J. D. (1999). *Classical electrodynamics*. 3rd ed. Wiley. ISBN: 9780471309321.

James, D. F. and J. Jerke (2007). "Effective Hamiltonian theory and its applications in quantum information". In: *Canadian Journal of Physics* 85.6, pp. 625–632. DOI: 10.1139/p07-060. URL: https://doi.org/10.1139%2Fp07-060.

Kang, M., W. C. Campbell and K. R. Brown (2022). *Quantum error correction with metastable states of trapped ions using erasure conversion*. arXiv: 2210.15024.

Kasprowicz, Grzegorz, Thomas Harty et al. (2022). "Urukul – Open-source Frequency Synthesizer Module for Quantum Physics". In: *International Journal of Electronics and Telecommunications* vol. 68.No 1, pp. 123–128. DOI: 10.24425/ijet.2022.139859. URL: http://journals.pan.pl/Content/122812/PDF-MASTER/18-3380-Kasprowicz_sk.pdf.

Kasprowicz, Grzegorz, Paweł Kulik et al. (2020). "ARTIQ and Sinara: Open Software and Hardware Stacks for Quantum Physics". In: *OSA Quantum 2.0 Conference*. Optica Publishing Group, QTu8B.14. DOI: 10.1364/QUANTUM.2020.QTu8B.14. URL: https://opg.optica.org/abstract.cfm?URI=QUANTUM-2020-QTu8B.14.

King, B. E. (2008). *Angular Momentum Coupling and Rabi Frequencies for Simple Atomic Transitions*. arXiv: 0804.4528. DOI: 10.48550/ARXIV.0804.4528. URL: https://arxiv.org/abs/0804.4528.

Kreuter, A. et al. (2005). "Experimental and theoretical study of the $3d\,^2D$–level lifetimes of $^{40}Ca^+$". In: *Phys. Rev. A* 71 (3), p. 032504. DOI: 10.1103/PhysRevA.71.032504. URL: https://link.aps.org/doi/10.1103/PhysRevA.71.032504.

Lechner, Regina et al. (2016). "Electromagnetically-induced-transparency ground-state cooling of long ion strings". In: *Phys. Rev. A* 93 (5), p. 053401. DOI: 10.1103/PhysRevA.93.053401. URL: https://link.aps.org/doi/10.1103/PhysRevA.93.053401.

Lee, P J et al. (2005). "Phase control of trapped ion quantum gates". In: *Journal of Optics B: Quantum and Semiclassical Optics* 7.10, S371. DOI: 10.1088/1464-4266/7/10/025. URL: https://dx.doi.org/10.1088/1464-4266/7/10/025.

Leibfried, D. et al. (2003). "Experimental demonstration of a robust, high-fidelity geometric two ion-qubit phase gate". In: *Nature News*. URL: https://www.nature.com/articles/nature01492.

Letokhov, Vladilen Stepanovich, Vladimir G. Minogin and Boris Pavlik (1977). "Cooling and capture of atoms and molecules by a resonant light field". In: *Journal of Experimental and Theoretical Physics* 45, p. 698.

Loudon, R. (2000). *The Quantum Theory of Light*. 3rd. Oxford Science Publications.

Meir, Ziv et al. (2020). "Combining experiments and relativistic theory for establishing accurate radiative quantities in atoms: The lifetime of the $^2P_{3/2}$ state in $^{40}Ca^+$". In: *Phys. Rev. A* 101 (1), p. 012509. DOI: 10.1103/PhysRevA.101.012509. URL: https://link.aps.org/doi/10.1103/PhysRevA.101.012509.

Metcalf, H. J. and P. van der Straten (1999). *Laser Cooling and Trapping*. Springer.

Metzner, J. M., D. T. C. Allcock and C. J. Ballance (2020). *Squareatron-5000*. https://github.com/OregonIons/Squareatron-5000.

Mølmer, K. and A. Sørensen (1999). "Multiparticle Entanglement of Hot Trapped Ions". In: *Phys. Rev. Lett.* 82 (9), pp. 1835–1838. DOI: 10.1103/PhysRevLett.82.1835. URL: https://link.aps.org/doi/10.1103/PhysRevLett.82.1835.

Monroe, C. et al. (1995). "Resolved-Sideband Raman Cooling of a Bound Atom to the 3D Zero-Point Energy". In: *Phys. Rev. Lett.* 75 (22), pp. 4011–4014. DOI: 10.1103/PhysRevLett.75.4011. URL: https://link.aps.org/doi/10.1103/PhysRevLett.75.4011.

Moore, I. D., W. C. Campbell et al. (2023). "Photon scattering errors during stimulated Raman transitions in trapped-ion qubits". In: *Phys. Rev. A* 107 (3), p. 032413. DOI: 10.1103/PhysRevA.107.032413. URL: https://link.aps.org/doi/10.1103/PhysRevA.107.032413.

Moore, I. D. and S. J. van Enk (2021). "Self-consistent tomography and measurement-device independent cryptography". In: *International Journal of Quantum Information* 19.07, p. 2040003. DOI: 10.1142/S0219749920400031. eprint: https://doi.org/10.1142/S0219749920400031.

Morigi, Giovanna, Jürgen Eschner and Christoph H. Keitel (2000). "Ground State Laser Cooling Using Electromagnetically Induced Transparency". In: *Phys. Rev. Lett.* 85 (21), pp. 4458–4461. DOI: 10.1103/PhysRevLett.85.4458. URL: https://link.aps.org/doi/10.1103/PhysRevLett.85.4458.

Neuhauser, W. et al. (1978). "Optical-Sideband Cooling of Visible Atom Cloud Confined in Parabolic Well". In: *Phys. Rev. Lett.* 41 (4), pp. 233–236. DOI: 10.1103/PhysRevLett.41.233. URL: https://link.aps.org/doi/10.1103/PhysRevLett.41.233.

Nielsen, Michael A. and Isaac L. Chuang (2000). *Quantum Computation and Quantum Information*. Cambridge University Press.

Ozeri, R. (2007). "Errors in trapped-ion quantum gates due to spontaneous photon scattering". In: *Phys. Rev. A* 75 (4), p. 042329. URL: https://www.nist.gov/publications/errors-trapped-ion-quantum-gates-due-spontaneous-photon-scattering.

Paul, Wolfgang and Helmut Steinwedel (1953). In: *Zeitschrift für Naturforschung A* 8.7, pp. 448–450. DOI: doi:10.1515/zna-1953-0710. URL: https://doi.org/10.1515/zna-1953-0710.

Pinnington, E. H., R. W. Berends and M. Lumsden (1995). "Studies of laser-induced fluorescence in fast beams of Srand Baions". In: *Journal of Physics B: Atomic, Molecular and Optical Physics* 28.11, pp. 2095–2103. DOI: 10.1088/0953-4075/28/11/009. URL: https://doi.org/10.1088/0953-4075/28/11/009.

Pinnington, E. H., G. Rieger and J. A. Kernahan (1997). "Beam-laser measurements of the lifetimes of the 6*p* levels in Yb II". In: *Phys. Rev. A* 56 (3), pp. 2421–2423. DOI: 10.1103/PhysRevA.56.2421. URL: https://link.aps.org/doi/10.1103/PhysRevA.56.2421.

Poulsen, O., T. Andersen and N. J. Skouboe (1975). "Fast-beam, zero-field level-crossing measurements of radiative lifetimes, fine and hyperfine structures in excited states of ionic and neutral beryllium". In: *Journal of Physics B: Atomic and Molecular Physics* 8.9, pp. 1393–1405. DOI: 10.1088/0022-3700/8/9/006. URL: https://doi.org/10.1088/0022-3700/8/9/006.

Ransford, Anthony et al. (Dec. 2021). "Weak dissipation for high-fidelity qubit-state preparation and measurement". In: *Phys. Rev. A* 104 (6), p. L060402. DOI: 10.1103/PhysRevA.104.L060402. URL: https://link.aps.org/doi/10.1103/PhysRevA.104.L060402.

Roos, Christian F. et al. (2004). "Control and Measurement of Three-Qubit Entangled States". In: *Science* 304.5676, pp. 1478–1480. DOI: 10.1126/science.1097522. eprint: https://www.science.org/doi/pdf/10.1126/science.1097522. URL: https://www.science.org/doi/abs/10.1126/science.1097522.

Saad, H. M. H. et al. (2021). "Quantum-Inspired Genetic Algorithm for Resource-Constrained Project-Scheduling". In: *IEEE Access* 9, pp. 38488–38502. DOI: 10.1109/ACCESS.2021.3062790.

Sackett, C. A. et al. (Mar. 2000). "Experimental entanglement of four particles". In: *Nature* 404.6775, pp. 256–259. DOI: 10.1038/35005011. URL: https://doi.org/10.1038/35005011.

Safronova, U. I. (2010). "All-order perturbation calculation of energies, hyperfine constants, multipole polarizabilities, and blackbody radiation shift in $^{87}Sr^{+}$". In: *Phys. Rev. A* 82 (2), p. 022504. DOI: 10.1103/PhysRevA.82.022504. URL: https://link.aps.org/doi/10.1103/PhysRevA.82.022504.

Sahoo, B. K. et al. (2006). "Lifetimes of the metastable $^2D_{3/2,5/2}$ states in Ca^+, Sr^+, and Ba^+". In: *Phys. Rev. A* 74 (6), p. 062504. DOI: 10.1103/PhysRevA.74.062504. URL: https://link.aps.org/doi/10.1103/PhysRevA.74.062504.

Sawyer, B. C. and K. R. Brown (2021). "Wavelength-insensitive, multispecies entangling gate for group-2 atomic ions". In: *Physical Review A* 103.2. DOI: 10.1103/physreva.103.022427. URL: http://dx.doi.org/10.1103/PhysRevA.103.022427.

Sherman, J. A. et al. (2013). "Experimental Recovery of a Qubit from Partial Collapse". In: *Phys. Rev. Lett.* 111 (18), p. 180501. DOI: 10.1103/PhysRevLett.111.180501. URL: https://link.aps.org/doi/10.1103/PhysRevLett.111.180501.

Song, H. F. et al. (2019). "Combined experimental and theoretical probe of the branching fractions of the $4P_{3/2}$ state in $^{40}Ca^{+}$". In: *Phys. Rev. A* 100 (5),

p. 052505. DOI: 10.1103/PhysRevA.100.052505. URL: https://link.aps.org/doi/10.1103/PhysRevA.100.052505.

Steck, D. A. (2001). "Rubidium 87 D Line Data." unpublished, available online at http://steck.us/alkalidata (Version 2.2.1, last revised 21 November 2019).

— (n.d.). *Classical and Modern Optics*. available online at http://steck.us/teaching (revision 1.7.7, 19 June 2020).

Tan, T. R. (2016). "High-Fidelity Entangling Gates with Trapped-Ions". unpublished thesis. PhD thesis. University of Colorado.

Tan, T. R. et al. (2015). "Multi-element logic gates for trapped-ion qubits". In: *Nature* 528.7582, pp. 380–383. DOI: 10.1038/nature16186. URL: https://doi.org/10.1038/nature16186.

Taylor, P. et al. (1997). "Investigation of the ${}^2S_{1/2}-{}^2D_{5/2}$ clock transition in a single ytterbium ion". In: *Phys. Rev. A* 56 (4), pp. 2699–2704.

Thermostat (2022). https://github.com/sinara-hw/Thermostat/wiki.

Uys, H. et al. (2010). "Decoherence due to Elastic Rayleigh Scattering". In: *Phys. Rev. Lett.* 105.20. DOI: 10.1103/physrevlett.105.200401. URL: http://dx.doi.org/10.1103/PhysRevLett.105.200401.

Wineland, D. J. (2003). "Quantum information processing with trapped ions". In: *Philos. Trans. R. Soc. A* 361.1808, pp. 1349–1361. DOI: 10.1098/rsta.2003.1205. URL: http://dx.doi.org/10.1098/rsta.2003.1205.

Wineland, D. J., R. E. Drullinger and F. L. Walls (1978). "Radiation-Pressure Cooling of Bound Resonant Absorbers". In: *Phys. Rev. Lett.* 40 (25), pp. 1639–1642. DOI: 10.1103/PhysRevLett.40.1639. URL: https://link.aps.org/doi/10.1103/PhysRevLett.40.1639.

Wineland, D.J. et al. (1998). "Experimental Issues in Coherent Quantum-State Manipulation of Trapped Atomic Ions". In: *J. Res. Natl. Inst. Stand. Technol.* DOI: 10.6028/jres.103.019.

Yang, H.-X. et al. (Sept. 2022). "Realizing coherently convertible dual-type qubits with the same ion species". In: *Nature Physics* 18.9, pp. 1058–1061. DOI: 10.1038/s41567-022-01661-5.

Zhang, H. et al. (2016). "Iterative precision measurement of branching ratios applied to 5Pstates in88Sr". In: *New Journal of Physics* 18.12, p. 123021. DOI: 10.1088/1367-2630/aa511d. URL: https://doi.org/10.1088/1367-2630/aa511d.

Zhang, J M and Y Liu (2016). "Fermi's golden rule: its derivation and breakdown by an ideal model". In: *European Journal of Physics* 37.6, p. 065406. DOI: 10.1088/0143-0807/37/6/65406. URL: http://dx.doi.org/10.10%208/0143-0807/37/6/065406.

Zhang, Z. et al. (2020). "Branching fractions for $P_{3/2}$ decays in Ba^+". In: *Physical Review A* 101.6. DOI: 10.1103/physreva.101.062515. URL: http://dx.doi.org/10.1103/PhysRevA.101.062515.